

Inaugural dissertation
for
obtaining the doctoral degree
of the
Combined Faculty of Mathematics, Engineering and Natural Sciences
of the
Ruprecht - Karls - University
Heidelberg

Presented by
M.Phil. Silvija Švambarytė
born in Šiauliai, Lithuania
Oral examination: 10.04.2024

Integration of axis elongation and somite patterning via signaling dynamics
in the medaka embryo

Referees:

Prof. Dr. Lázaro Centanin

Dr. Justin Crocker

Acknowledgements

I am grateful to Alexander Aulehla for his guidance and encouragement throughout this long journey.

I thank my thesis advisory committee members Justin Crocker, Michael Knop, James Sharpe, and Ben Steventon for their valuable feedback and support. Thanks to Sergio P. Acebrón, Lázaro Centanin, Justin Crocker, and Vikas Trivedi for serving on my thesis defense committee.

I thank Lázaro Centanin and Paul François and their groups for generously sharing their resources and expertise with us.

I am deeply thankful to all members of the Aulehla lab for their friendship and making our lab such a warm, supportive, and fun place to work at. Above all, I thank Carina for passing down her knowledge of medaka to me and supporting me in every way possible – from experimental work and data analysis to being a true friend – throughout my PhD. I am thankful to Takehito for his kind help with spatial gradient analysis and the camaraderie we shared as lab mates, batch mates, and flat mates. Thanks to Jona and Michael for their friendship and making me laugh so much. Thank you to my taekwondo companions Emilia and Ana for all the Friday nights we spent laughing and kicking each other. Thank you to Paul for consistently checking-in with me and being so supportive. Thank you to Ana, Hidenobu, Michael, Takehito, Sapna, Sarkis, and Simona for reading parts of my thesis and providing feedback. A special thanks to Simon for translating the summary.

An honorable mention goes to Dimitri – while the data we generated together did not make it into this thesis, I am grateful for our collaboration and the beautiful movies we managed to obtain.

Thanks to all the friends I made in Heidelberg and to my time- and distance-tested friends – Paulius, Simona, and Vilija – for their continuing friendship and support.

I thank my parents Jovita and Arvydas and my sister Elvina for supporting my decisions and for all the sacrifices they have made to help me reach this milestone.

Lastly, I thank Pablo for bringing so much joy to my life and being the best companion one could ask for.

Summary

Vertebrate embryos robustly pattern their anteroposterior axis with a relatively invariant species-specific number of somites despite conspecific variation in body size. The periodicity with which somites segment from the anterior end of the unsegmented presomitic mesoderm (PSM) has been linked to the activity of a molecular oscillator known as the segmentation clock, which involves tissue-level oscillatory signaling in the PSM. A striking feature of anteroposterior axis patterning is that somite segmentation occurs concomitantly with axis elongation. The central hypothesis of this thesis posits that axis elongation and somite segmentation are integrated in the PSM via segmentation clock dynamics to ensure the production of a correct number of size-adjusted somites, regardless of PSM size. The work presented here explores this hypothesis in medaka (*Oryzias latipes*) through two independent projects.

Since axis elongation has not been characterized in medaka, the first project focused on providing the first tissue-level description of elongation and volumetric growth dynamics in this model organism. I used real-time imaging of medaka tail explants during secondary body formation and described a method to segment individual tissues from the resulting time-series data. Morphometric analysis of the paraxial mesoderm, neural tube, and notochord tissues revealed similar elongation rates, but significant tissue-specific differences in volumetric growth, with the notochord exhibiting a significantly higher fold volume increase than other tissues. Additionally, the study revealed that the PSM elongated over time despite a net decrease in its length and, intriguingly, that its elongation was accompanied by volumetric shrinkage.

The second project delved into the integration of axis elongation and somite segmentation in medaka tail explants, with a specific focus on segmentation clock dynamics. I used aphidicolin to disrupt axis elongation within the *her7-Venus* segmentation clock reporter line and assessed its impact on somite segmentation, in terms of both morphology and tissue-level signaling dynamics. This perturbation resulted in an accelerated reduction in the net length of the PSM, indicating an imbalance between tissue elongation and segmentation. Additionally, real-time imaging and quantitative analysis of Her7-Venus expression in the PSM revealed a reduction in the oscillation period across the tissue, leading to an upward

shift in the period gradient. Further examination of phase distribution in the PSM demonstrated that the phase gradient scaled with PSM length, such that a consistent phase amplitude was reached in the tissue irrespective of its size. This finding supports the notion that the phase gradient plays a functional role in the scaling mechanism, ensuring robust patterning of the anteroposterior axis.

To sum up, this thesis sheds light on previously unexplored aspects of medaka development and provides valuable insights into the intricate coordination of tissue-level processes essential for the robust patterning of the anteroposterior axis in vertebrates.

Zusammenfassung

Wirbeltierembryonen strukturieren ihre anterior-posteriore Achse robust mit einer relativ konsistenten, artspezifischen Anzahl von Somiten, trotz variationsbedingter Unterschiede in der Körpergröße. Die Periodizität, mit der Somiten von dem anterioren Ende des unsegmentierten präsomitischen Mesoderms (PSM) segmentieren, ist mit der Aktivität eines molekularen Oszillators, der als die ‘Segmentationsuhr’ bezeichnet wird, in Verbindung gebracht worden. Dieser Prozess beinhaltet oszillierende molekulare Signalwegsgebung auf Level des Gewebes im PSM. Ein bemerkenswertes Merkmal der Strukturierung der anteroposterioren Achse in Wirbeltieren ist, dass die Segmentierung der Somiten gleichzeitig mit der axialen Elongation erfolgt. Die zentrale Hypothese dieser Dissertation lautet, dass die axiale Elongation und die Somitensegmentierung im PSM über die Dynamik der Segmentationsuhr integriert sind, um die Formation einer korrekten Anzahl von größenangepassten Somiten unabhängig von der Größe des PSM sicherzustellen. Die hier vorgestellte Arbeit untersucht diese Hypothese anhand von zwei unabhängigen Projekten in Medaka (*Oryzias latipes*).

Da die axiale Elongation in Medaka bis dato noch nicht genauer beschrieben wurde, konzentrierte sich das erste Projekt darauf, die erste gewebespezifische Beschreibung der Elongations- und Volumenwachstumsdynamik in diesem Modellorganismus zu liefern. Hierfür wurde Echtzeitbildgebung von Medaka-tail-Explantaten während der sekundären Körperformation betrieben und eine Methode zur Segmentierung einzelner Gewebe aus den resultierenden Zeitraffermikroskopiedaten entwickelt. Die morphometrische Analyse von Geweben des paraxialen Mesoderms, des Neuralrohrs und der Chorda dorsalis zeigte vergleichbare Elongationsraten, aber signifikante gewebespezifische Unterschiede im Volumenwachstum, wobei die Chorda dorsalis eine signifikant höhere Volumenvergrößerung als andere Gewebe aufwies. Zusätzlich zeigte die Studie, dass das PSM im Laufe der Zeit trotz einer Nettoverkürzung seiner eigenen Länge elongiert und, interessanterweise, diese Elongation mit einer volumetrischen Schwindung einhergeht.

Das zweite Projekt beschäftigte sich genauer mit der Integration von axialer Elongation und Somitensegmentierung in Medaka-tail-Explantaten und konzentrierte sich

hierbei speziell auf die Dynamik der Segmentationsuhr. Hierfür wurde Aphidicolin verwendet, um die axiale Elongation in der *her7-Venus* Segmentationsuhr-Reporterlinie pharmakologisch zu inhibieren und die Auswirkung dieser Perturbation auf die Somitensegmentierung in Bezug auf sowohl Morphologie als auch Gewebesignalgebungsdynamik zu bewerten. Diese Perturbation führte zu einer beschleunigten Abnahme der Netto-Länge des PSM, was ein Ungleichgewicht zwischen Geweeelongation und Segmentierung suggeriert. Zusätzlich zeigte die Echtzeitbildgebung und quantitative Analyse der Her7-Venus-Expression im PSM eine Verringerung der Oszillationsperiode im gesamten Gewebe auf, was zu einer Aufwärtsverschiebung des Perioden-Gradienten führte. Weitere Untersuchungen der Verteilung an Oszillationsphasen im PSM zeigten, dass der Phasengradient mit der Größe des PSM skaliert, um sicherzustellen, dass, unabhängig von der Größe des PSMs, eine konsistente Phasenamplitude im Gewebe erreicht wird. Diese Ergebnisse unterstützen das Argument, dass der Phasengradient eine funktionelle Rolle im Skalierungsmechanismus spielt und somit die robuste Strukturierung der anteroposterioren Achse gewährleistet.

Zusammenfassend beleuchtet diese Arbeit bislang unerforschte Aspekte der Entwicklung von Medaka und liefert wertvolle Einblicke in die komplexe Koordination der Prozesse auf Gewebelevel, die für die robuste Strukturierung der anteroposterioren Achse bei Wirbeltieren von entscheidender Bedeutung sind.

Contents

Acknowledgements	iii
Summary	v
Zusammenfassung	vii
1 Introduction	1
1.1 Robustness of embryonic patterning	1
1.1.1 Scaling embryonic pattern to size	1
1.1.2 Regulative responses to embryo size reduction	2
1.1.3 Robust patterning of the anteroposterior axis	5
1.2 Anteroposterior axis elongation	7
1.2.1 Mechanisms based on cell rearrangements	8
1.2.2 Mechanisms based on volumetric growth	9
1.3 Anteroposterior axis segmentation	11
1.3.1 The clock-and-wavefront model	11
1.3.2 The phase-shift model	17
1.4 Integration of anteroposterior axis elongation and segmentation	19
1.4.1 FGF signaling gradient controls axis elongation	19
1.4.2 FGF signaling gradient acts upstream of the segmentation clock	20
1.5 Medaka as a model system to study robust patterning	21
1.5.1 Experimental advantages provided by the medaka embryo	21
1.5.2 Medaka anteroposterior axis patterning as a system for comparative developmental biology	22
1.6 Aims of the study	24
2 Results	25
2.1 Quantification of tissue-specific behaviors during secondary body formation	25
2.1.1 Visualization and segmentation of distinct tissues using the tail explant system	25
2.1.2 Elongation and volumetric growth dynamics in tail explants	30
2.2 Investigating the integration of axis elongation and somite segmentation	39
2.2.1 Surgical perturbation of axis elongation	39
2.2.2 Pharmacological perturbation of axis elongation	43
2.2.3 Impact of aphidicolin treatment on somite scaling	47
2.2.4 Impact of aphidicolin treatment on oscillatory gene expression dynamics	49
3 Discussion	61
3.1 Axis elongation during secondary body formation in medaka	61
3.1.1 Axis elongation is accompanied by volumetric growth	61
3.1.2 PSM elongation is associated with a decrease in volume	64
3.1.3 Paraxial mesoderm is the main contributor to overall volumetric growth in the tail explant	65
3.2 Integration of axis elongation and somite segmentation	67
3.2.1 Dissecting the regulative response to experimental size reduction in medaka embryos	67
3.2.2 Dissecting the lack of somite scaling in aphidicolin-treated tail explants	69
3.2.3 Period and phase gradients respond to aphidicolin treatment	70
3.3 Outlook	73
4 Materials and methods	75

4.1	Fish husbandry	75
4.2	General embryo handling	75
4.2.1	Dechoriation with hatching enzyme	75
4.2.2	Manual dechoriation and dissection of tail explants	76
4.3	Morphometric analysis	76
4.3.1	Whole-mount antibody staining	76
4.3.2	Mounting and imaging	77
4.3.3	Tissue segmentation	78
4.3.4	Tissue length and volume measurements	79
4.3.5	Quantification of PH3-positive cells in a tissue-specific manner	80
4.4	Surgical size reduction	80
4.4.1	Preparation	80
4.4.2	Cell removal and cell counting	81
4.4.3	DAPI staining	81
4.4.4	Embryo mounting and imaging	82
4.5	Pharmacological perturbation of axis elongation	82
4.5.1	Aphidicolin treatment	82
4.5.2	Antibody staining	83
4.5.3	Tail explant mounting and imaging	83
4.5.4	Quantification of PH3-positive cells	84
4.5.5	Time-series image registration	85
4.5.6	Length measurements	85
4.5.7	Quantification of signaling dynamics	85
5	Bibliography	87

1 Introduction

1.1 Robustness of embryonic patterning

Robustness describes the property of a biological system to produce a consistent, functionally reliable phenotype irrespective of genetic variation, environmental fluctuations, and the stochastic nature of biochemical reactions. It is often contrasted with plasticity, a property of genetically identical organisms to generate different phenotypes depending on the environmental input. Although seemingly diametrically opposed, these two properties often operate in concert during embryonic patterning, the process that organizes cell fates in space and time to establish the basic body plan of a mature organism, with intricately arranged tissues and organ systems. In this chapter, I introduce the topic of robustness in embryonic patterning by revisiting classical experimental embryology studies conducted in several vertebrate model systems.

1.1.1 Scaling embryonic pattern to size

The deeply intertwined nature of robustness and plasticity is beautifully illustrated by the relationship between patterning and size during embryonic development. Although embryonic size is constrained to a certain species-specific range, it remains a relatively plastic trait that is influenced by multiple factors, including genetic background and environmental conditions. In addition, embryos undergoing cell proliferation and extensive morphogenesis are bound to make some errors that can affect the overall cell number in the embryo. Given that cell proliferation is an exponential process, these errors, if not accounted for, can compound to give substantial size phenotypes. Due to the multifaceted interplay of the above-mentioned factors, conspecific embryos often display considerable variation in size. For example, the natural size variation in *Xenopus* embryos before mid-gastrula stages can exhibit approximately a 38% difference in diameter between extremes [1].

Despite this inherent variability in size, embryos are generally able to robustly pattern their bodies with invariant proportions, maintaining a characteristic size relationship between different body parts and the body as a whole throughout development. This fundamental property of embryonic development, called scaling, ensures the consistent generation of

complete and, therefore, functional body plans in accordance with the available tissue. As revealed by classical experimental embryology studies, the remarkable ability of embryos to scale their pattern to body size pertains not only in the context of natural variation, but also in the face of more severe experimental perturbations [2-10]. These studies, which have been instrumental in revealing the different regulative responses embryos rely on to correctly pattern their tissues, are introduced in the subsequent section.

1.1.2 Regulative responses to embryo size reduction

In 1901, Thomas Hunt Morgan coined the terms morphallaxis and epimorphosis to distinguish two modes of regulative response to disturbance [11]. Although mostly used in the field of regeneration, these terms have also been employed to describe the means by which the constancy of proportions is maintained in early embryos when part of the cells is removed from the embryonic field.

1.1.2.1 Morphallaxis

In morphallaxis, embryos respond to cell loss by adjusting the developmental trajectory of remaining cells in reference to their new position within an abnormally-sized field. Importantly, no compensatory mechanisms are put in place in morphallactic embryos to make up for the lost cellular material and reduced size. With fewer cells available to generate a complete body pattern, morphallactic embryos fall outside the normal size range, but are nevertheless correctly patterned. Tung and Tung were among the first to qualitatively describe the ability of vertebrate embryos to scale their patterns to a reduced size [2]. Using goldfish as a model system, the authors observed that embryo bisection at the stages of 2, 4, and 8 cells occasionally resulted in the normal development of one or both of the resulting halves, giving rise to normally proportioned embryos at half the typical size. The first quantifications of pattern scaling were later provided by Cooke in amphibians belonging to the genus *Xenopus* and *Ambystoma* [3, 4]. Ventral blastomere excision or destruction during the morula/early blastula stages led to miniaturized embryos with normally proportioned whole-body patterns at the tailbud stages. Despite containing 30-61% and 25-51% normal mesodermal cell counts in *Xenopus* and *Ambystoma*, respectively, the proportions of cells assigned to four different parts of the pattern – notochord, somites, pro-nephros, and lateral plate – were comparable between manipulated and normal embryos. More recently, similar observations were made in

zebrafish embryos, where removal of the vegetal yolk or a portion of cells near the animal pole from blastula stage embryos resulted in abnormally small yet correctly patterned individuals with correspondingly smaller organs (**Fig. 1**) [5-7]. Collectively, these findings demonstrate that achieving a complete pattern does not depend on reaching a set size in morphallactic embryos and that morphallaxis is a common feature of embryonic development across the vertebrate subphylum.

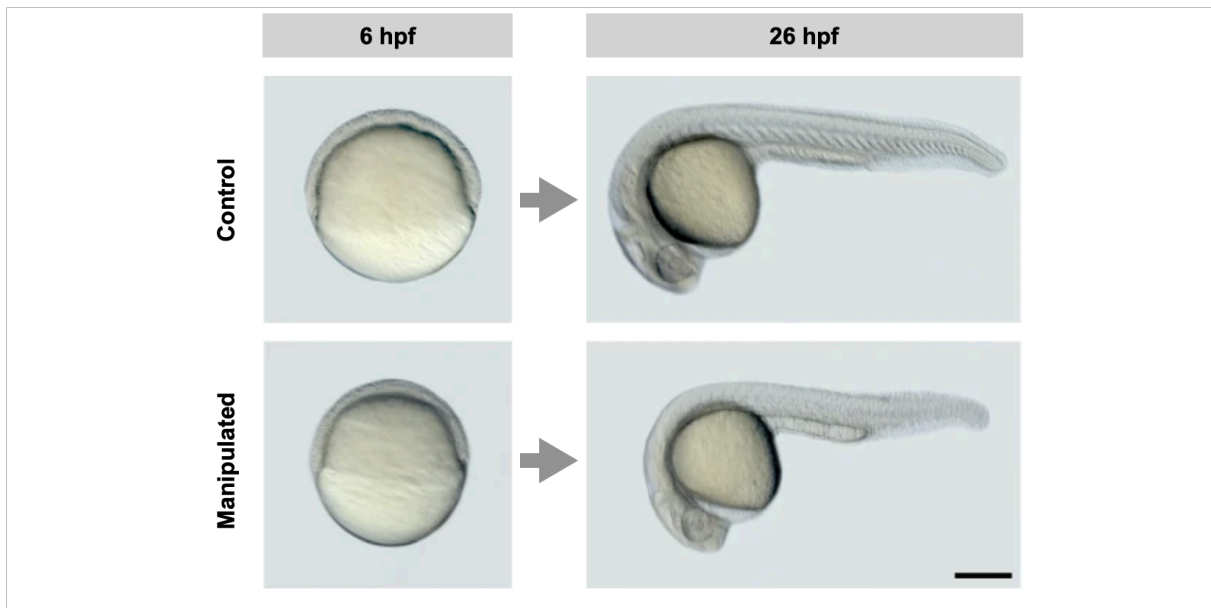


Figure 1. Morphallactic response to cell removal at the blastula stage in zebrafish. A comparison of embryo size at 6 hpf and 26 hpf between control (top) and manipulated (bottom) animals. Manipulated animals exhibit normal developmental rates and maintain correct patterning, but are smaller compared to control animals. Scale bar: 200 μ m. Adapted from [7], with permission from Springer Nature.

1.1.2.2 Epimorphosis

Epimorphosis, in contrast to morphallaxis, is characterized by the stimulation of the cell cycle to compensate for lost cellular material after size reduction. As epimorphic fields upregulate their cell count and, consequently, their overall size towards normal, they circumvent the challenge of having to derive an entire pattern from a reduced field. A paradigm of epimorphic regulative response to size perturbation is provided by the mouse embryo. Snow and Tam demonstrated that intraperitoneal injection of the teratogen Mitomycin-C into pregnant females at 6.5-7 days post-coitum (dpc) caused severe damage to embryos at 7.5 dpc, reducing their cell number by about 75% [8]. Importantly, Mitomycin-C-treated embryos delayed the initiation of gastrulation until a body size appropriate for the gastrulation stage was reached, consequently accumulating a morphological retardation of

approximately 12 hours by 8.5 dpc. Strikingly, this was followed by a period of compensatory growth, in which increased mitotic activity throughout the embryo enabled treated embryos to gradually catch up with normal embryos in terms of both size and morphology. As a result, treated and normal embryos were not noticeably different by the time of birth at 13.5 dpc [8]. A similar recovery capacity was also observed in surgically size-reduced mouse embryos. In this case, the removal of one blastomere from a 4-cell preimplantation embryo caused about a 30% reduction in normal cell counts and a delayed onset of gastrulation in 6.5 dpc embryos. Following the initial retardation phase, manipulated embryos exhibited an upregulation of cell proliferation during gastrulation, achieved by increasing the number of cells proliferating across the embryo and shortening their cell cycle. As a result, manipulated embryos successfully restored normal body size and morphology by 13.5 dpc (**Fig. 2**) [9].

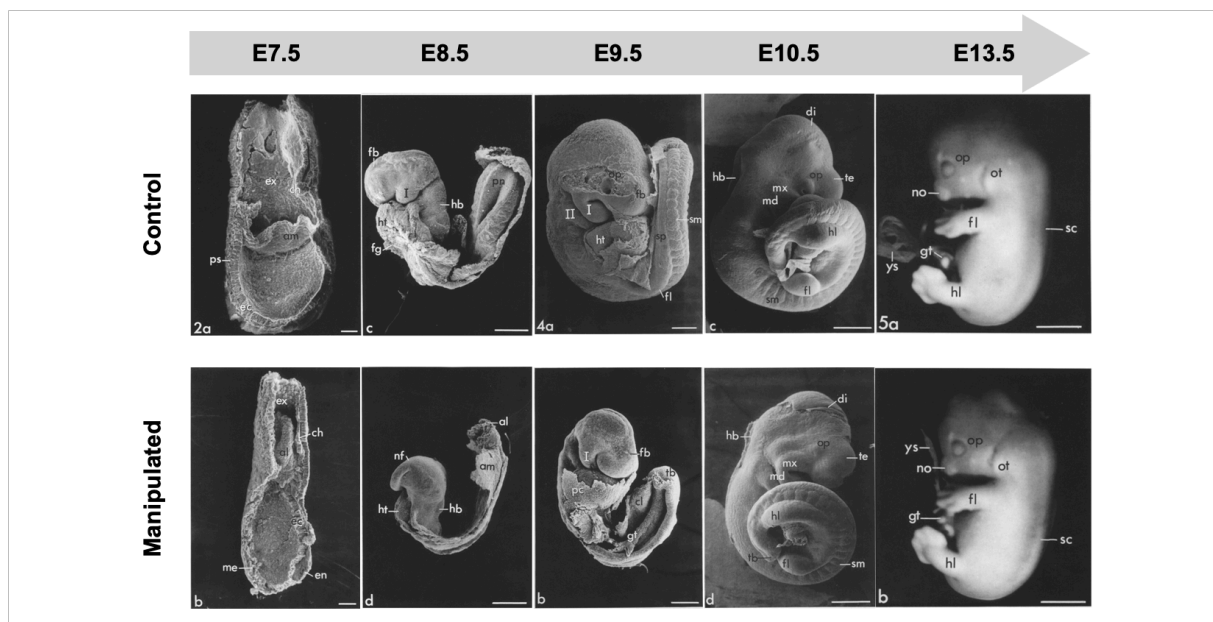


Figure 2. Epimorphic response to the removal of one blastomere at the 4-cell stage in mice. A comparison of embryo size at different time points (E7.5 – E13.5) between control (top) and manipulated (bottom) animals. Manipulated animals exhibit a different developmental rate; they initiate gastrulation after reaching the correct size, rather than at the correct chronological time, leading to an initial developmental retardation, which is then followed by accelerated development. Throughout development, tissues and organs are formed in normal proportion. Scale bars: 50 μm for E7.5, 200 μm for E8.5 and E9.5, 500 μm for E10.5, 2 mm for E13.5. Adapted from [9], with permission from Springer Nature.

As compensatory growth and embryonic patterning in the mouse embryo proceed concomitantly, it appears that in this model system the regulative response to size reduction is not purely epimorphic, but partakes in both morphallactic and epimorphic modes. In fact, Maden [12] has hypothesized that both morphallaxis and epimorphosis rely on the same basic mechanisms to produce scaled spatial patterns, with compensatory growth (which is

characteristic of epimorphic systems) acting as an additional component on top of morphallactic behavior. Interestingly, among the vertebrate species subjected to experimental embryo size reduction (mouse, frog, salamander, zebrafish, and goldfish), only mouse embryos demonstrate the capability for compensatory growth, enabling them to regulate their size back to normal [2-9]. It is therefore enticing to speculate that size regulation at the organismal level might be linked to the availability of large energy reserves associated with a viviparous mode of development.

1.1.3 Robust patterning of the anteroposterior axis

The vertebrate body plan exhibits segmental organization along the anteroposterior body axis. The foundation on which this segmental pattern is built is established early in embryonic development by somitogenesis. During somitogenesis, paired blocks of tissue, called somites, are periodically segmented in an anterior to posterior progression from the anterior end of the undifferentiated presomitic mesoderm (PSM) tissue, forming a repetitive striped pattern along the axis [13-15]. Later in development, somites mature to form the axial skeleton, skeletal muscles of the trunk, and dorsal dermis [13-15].

Somitogenesis is a remarkably robust process, generating a relatively invariant number of somites in a species-specific manner. For instance, zebrafish, *Xenopus*, chicks, and mice produce 32, 45, 55, and 65 somites, respectively. In line with previously discussed data, this consistency holds true not only in the context of natural variation, but also following experimental size perturbations. In his pioneering work, Cooke noted that *Xenopus* embryos, surgically reduced in size to approximately two-thirds of the normal length, accommodated a correct number of somites that were size-adjusted in proportion to the overall body size [3]. Synonymous observations have since been reported in surgically size-reduced zebrafish embryos and Mitomycin-C-treated mouse embryos [5, 10]. It should be noted that in the latter case, the rate of somite formation was initially delayed, leading to an accumulation of a 10-12 hour delay in trunk somite formation stages. In accordance with the reduced body size, the size of newly forming somites was initially scaled down, showing about a 50% reduction in the number of cells assigned to upper trunk somites. However, as the treated embryos initiated a compensatory growth response and started approaching the developmental stage and body size appropriate for their chronological age, both somite number and size began to catch up with normal values. Consequently, by 11.5-12.5 dpc, both normal and treated embryos

formed a full complement of somites, with the size of posterior nascent somites comparable between the two groups. Together, these studies demonstrate that regulation of somite number is brought about by adjusting the spatial scale with which somites are set up not only in morphallactic embryos, but also in epimorphic embryos that deviate from their normal growth profile due to compensatory growth.

Several studies have observed that somite length scales to that of the PSM throughout ontogeny in both normal and size-reduced systems [5, 10, 16]. The precision with which embryos regulate their somite number is particularly striking given that somite segmentation unfolds concomitantly with axis elongation, which provides new tissue for segmentation. This means that the generation of the correct number of somites involves more than a mere partitioning of pre-existing tissue; instead, it results from a dynamic integration of the rates of axis elongation and segmentation. Hence, both of these factors must be considered when exploring the fundamental principles governing robust anteroposterior axis patterning. Accordingly, the subsequent two chapters delve into the mechanisms involved in axis elongation (refer to **1.2**) and somite segmentation (refer to **1.3**), while chapter **1.4** looks into their potential integration.

1.2 Anteroposterior axis elongation

The vertebrate body plan is laid down progressively along the elongating anteroposterior axis. Based on developmental timing and structures that are formed in its wake, axis elongation can be divided into two phases - primary and secondary body formation. Primary body formation occurs during gastrulation and gives rise to the head anlage and anterior trunk structures. Secondary body formation initiates with the emergence of the tailbud and ends with the completion of somitogenesis, giving rise to structures of the posterior trunk and tail without breaking tissue continuity along the anteroposterior axis.

Tissues formed during primary and secondary body formation assume a stereotypic organization in three-dimensional (3D) space (**Fig. 3**). The notochord and neural tube extend longitudinally along the midline and the dorsal aspect of the embryo, respectively. These tissues are flanked on both sides by the paraxial mesoderm, which can be further subdivided into the anterior segmented somitic region and the posterior unsegmented PSM. Importantly, while the three tissues interact to coordinate their morphogenesis, they do not necessarily follow the same path to achieve elongation [13, 17, 18].

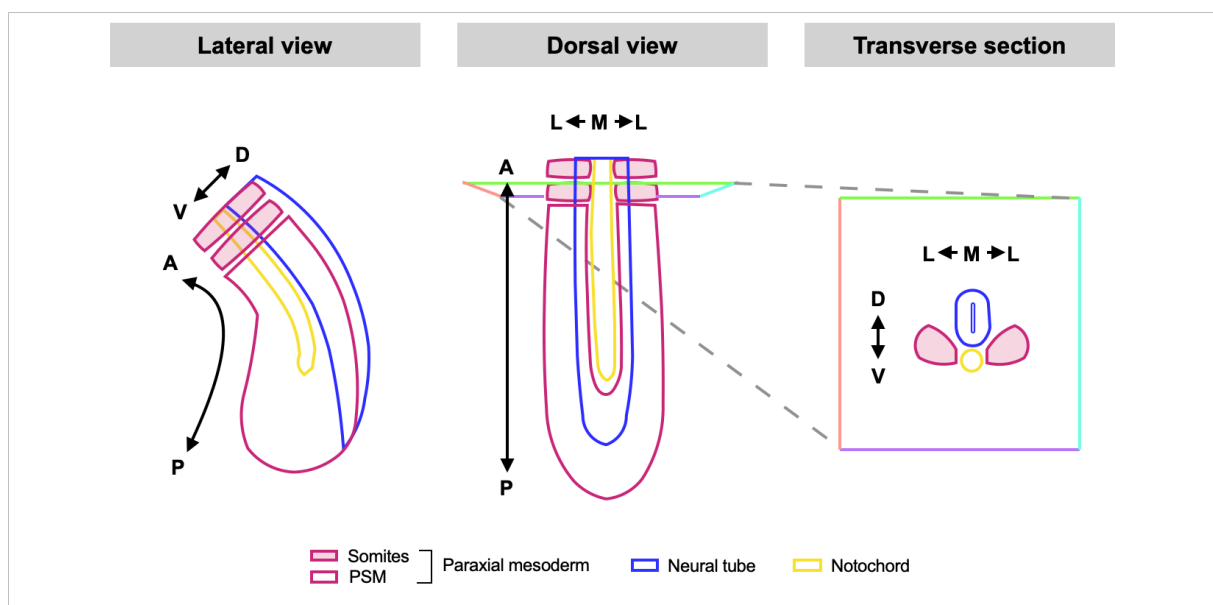


Figure 3. The arrangement of key tissues along the anteroposterior (AP), dorsoventral (DV), and mediolateral (ML) axes in a generalized vertebrate embryo.

The embryo's toolkit for axis elongation includes a limited number of cell behaviors that can be grouped into two major categories - those relying on tissue rearrangements

(through spatial reorganization of pre-existing cells) and those generating volumetric growth (through cell division and cell growth). Embryos of different species make use of different combinations of these cell behaviors to generate the same basic body plan. This is perhaps not surprising, given species-specific differences in initial geometries, nutritional environments, and developmental rates. Some generalizations can nonetheless be made regarding the differential employment of tissue rearrangement-based and volumetric growth-based mechanisms during the two phases of embryonic development. Particularly, the initial elaboration of the anteroposterior axis during primary body formation is generally dominated by tissue rearrangements, resulting in rapid changes in embryo shape. Volumetric growth, which is limited in speed by the rate of biomaterial synthesis, becomes more prominent in driving axis elongation during secondary body formation [19].

1.2.1 Mechanisms based on cell rearrangements

In all vertebrate species examined to date, the elongation of the anteroposterior axis during primary body formation is intimately linked with convergent extension movements. Outwardly defined as a concomitant lengthening of the anteroposterior axis and narrowing of the mediolateral axis of the embryo, convergent extension is a large-scale morphogenetic movement that brings cells towards the body midline by two distinct cellular mechanisms – mediolateral intercalation and collective cell migration.

Mediolateral intercalation was first identified as a major driver of convergent extension by Keller and colleagues in early *Xenopus* embryos. Tracings of small patches of labelled cells in histological preparations of unlabeled host embryos and real-time imaging of cell behavior in cultured explants revealed that cells from prospective mesodermal (i.e., paraxial mesoderm, notochord) and neuroectodermal (i.e., neural tube) tissues intercalate between their neighbors along the mediolateral axis, leading to rapid convergence towards the midline and concomitant extension along the anteroposterior axis [20-25]. Similar intercalations have also been detailed in zebrafish embryos during the formation of axial (i.e., notochord) and paraxial (i.e., paraxial mesoderm) dorsal tissues [26-28]. However, while convergent extension in *Xenopus* embryos is driven solely by mediolateral intercalation, early zebrafish embryos use it in combination with collective cell migration [29]. Specifically, laterally residing paraxial mesoderm progenitors initially converge towards the dorsal midline as a cohesive sheet, causing the tissue to narrow and thicken but not to extend. Subsequently,

as they get closer to the midline, cells begin to intercalate with their neighbors in a manner similar to that observed in *Xenopus*, leading to axis extension. Importantly, although convergent extension has been mainly studied during primary body formation in *Xenopus* and zebrafish embryos, it appears to play a ubiquitous role in shaping the vertebrate body plan throughout the embryonic development [30-35].

In chick and zebrafish embryos, the extension of the axis (but not the convergence) during secondary body formation is also believed to depend on a gradient of random cell motility in the PSM. Cell motility is highest in the posterior PSM, gradually decreasing anteriorly and finally ceasing as cells become incorporated into somites [36-38]. Locally, individual PSM cells exhibit random, Brownian-like movements, which is in contrast to oriented cell intercalations observed during primary body formation [37, 38]. Given that the PSM is confined anteriorly, dorsally, and laterally by stiff neighboring tissues, it has been proposed that the graded cell motility within the PSM can generate a posteriorly oriented force, causing the body axis to extend [39-41].

1.2.2 Mechanisms based on volumetric growth

The second category of mechanisms contributing to axis elongation involves cell behaviors that generate additional volume. Generally, the importance of volumetric growth-generating behaviors increases during secondary body formation, although different vertebrates demonstrate varying degrees of volumetric growth during this process. For instance, the elongation of the secondary body in mouse, chick, and dogfish embryos is significantly influenced by volumetric growth, while zebrafish and lamprey embryos elongate their axis with little volumetric growth [35, 39]. These differences seem to arise from the broader developmental context of these embryos, encompassing factors such as nutrient accessibility, the rate of embryonic development, biochemical kinetics, and others [19, 35, 42].

During secondary body formation, cell proliferation emerges as a major cell behavior associated with volumetric growth. However, it is important to emphasize that cell proliferation alone does not generate additional volume unless accompanied by cell growth. This is exemplified by early embryonic cleavages, where the absence of G1 and G2 phases in

the cell cycle leads to the progressive division of pre-existing egg cytoplasm into increasingly smaller blastomeres [43].

A widely accepted model in the field posits that the formation of the secondary body is driven by the proliferation of progenitor cells within a posterior growth zone [44]. This model gained significant traction with the discovery of a population of bi-competent neuromesodermal progenitors (NMps) in the tailbud of amniote embryos, which have the potential to give rise to both ectodermal (i.e., neural tube) and mesodermal (i.e., paraxial mesoderm) descendants [42, 45-50]. An equivalent bi-competent progenitor population has also been identified in the zebrafish tailbud. However, in this model organism, the accelerated pace of embryonic development, coupled with very low proliferation rates in the tailbud, restrict the capacity of NMps to self-renew and, consequently, realize their bi-competence under normal conditions [51-55].

Importantly, recent evidence challenges the idea that posterior growth is the primary contributor to secondary body elongation and invites a reconsideration of NMps as primary determinants of volumetric growth during vertebrate development. It is now evident that cells proliferate along the anteroposterior axis in both amniotes and anamniotes. While growth appears to be uniform along the axis in amniote embryos, in zebrafish, the proportion of cells undergoing mitosis is actually lower in the tailbud than in the rest of the axis [35, 55]. Therefore, the volumetric growth observed in a given species is a product of cell proliferation throughout the entire secondary body, rather than proliferation of progenitor cells confined to the tailbud [35, 39, 51, 56].

In addition to cell proliferation throughout the body axis, axis elongation is also accompanied by marked cell growth in the notochord. Following the formation of the notochord by mediolateral intercalation, intracellular vacuoles in the inner layer of notochord cells fill up with fluid and inflate, leading to significant cell swelling [57-61]. Combined with the constraint provided by an outer sheath of cells and a thick extracellular basement membrane, vacuolization not only produces the volumetric growth necessary for notochord elongation, but also exerts pressure to straighten the entire elongating axis [59, 60].

1.3 Anteroposterior axis segmentation

During the process of anteroposterior axis segmentation, somite pairs emerge one after the other with striking spatiotemporal periodicity, progressively subdividing the elongating axis into a relatively invariant number of somites, regardless of the overall size of the embryo [13-15]. Building a scaled metameric pattern within a dynamic and growing system poses a fascinating morphogenetic challenge, capturing the interest of researchers from both theoretical and experimental backgrounds for the past five decades. In this chapter, I introduce two prominent theoretical frameworks that offer insight into the emergence of periodic patterns and present experimental evidence supporting these models in the specific context of anteroposterior axis segmentation [62, 63].

1.3.1 The clock-and-wavefront model

For decades, the formation of scaled periodic patterns during somitogenesis has been interpreted according to the clock-and-wavefront model proposed by Cooke and Zeeman [62]. This model postulates the existence of two independent components, the clock and the wavefront, that interact in the PSM to define when and where the next somite pair will form. In this model, the clock is described as an oscillator that alternates synchronously between permissive and non-permissive states across the PSM, while the wavefront is described as a posteriorly regressing front of cell competence to undergo a sudden change of state that culminates in somite formation. According to the model, cells anterior to the regressing front are incorporated into somites with each permissive state of the clock, resulting in successive somite formation at the period dictated by the clock. To accommodate somite scaling, the model incorporates elements from Wolpert's positional information theory, assuming that the wavefront is governed by a long-range gradient that imparts positional identity to PSM cells [64].

In its conception, the clock-and-wavefront model presented these components as abstract entities, with no speculation as to what their molecular nature could be. Today, these theoretical postulations have significant experimental support, and our current understanding of the molecular identities of the clock and the wavefront is detailed below.

1.3.1.1 The clock - a network of coupled molecular oscillators in the PSM

The first molecular evidence for an internal oscillator involved in vertebrate segmentation, termed the segmentation clock, came with the discovery of periodic activation of *c-hairy* (now renamed *HES4*) expression in the chick PSM [65]. This gene encodes a protein belonging to the hairy and enhancer of split (HES)/HES-related (HER) family of basic helix-loop-helix (bHLH) transcriptional repressors that act downstream of the Notch signaling pathway [66-68]. Subsequent investigations, including *in situ* hybridization and genome-wide microarray hybridization studies across various vertebrate species, revealed additional genes displaying analogous periodic expression in the PSM, indicating that the segmentation clock comprises an intricate network of oscillating genes [14, 65, 69-91]. Periodic expression of genes related to the Notch signaling pathway has been consistently observed in all vertebrate species studied, emphasizing the conserved role of this pathway's oscillatory activity in the segmentation clock mechanism [14, 65, 69-84]. In addition, components of the fibroblast growth factor (FGF) and Wnt signaling pathways have been reported to exhibit periodic expression in the PSM of mouse and chick embryos, as well as in *in vitro*-derived human PSM cells [83-91]. Notably, at least one member of the HES/HER family is periodically activated in all vertebrate species examined to date, including human, mouse, chick, *Xenopus*, zebrafish, and medaka [65, 69-78, 92]. These collective findings suggest that HES/HER transcription factors play a central role in the segmentation clock machinery, despite variations in the topology of the segmentation clock network among different species.

In biological systems, self-sustained oscillatory behavior often hints at the presence of at least one delayed negative feedback loop in the underlying regulatory network [93]. The inhibitory nature of HES/HER transcription factors thus prompted the hypothesis that periodic activation of *HES/HER* genes in the PSM might be driven by an intracellular negative autoregulatory circuit. Supporting this idea, both *Hes7* mRNA and HES7 protein are expressed in an oscillating manner in the mouse PSM. Importantly, their expression domains are mutually exclusive, suggesting that HES7 inhibits transcription from its own promoter [94]. Indeed, HES1 and HES7 in mice and Her1 and Her7 in zebrafish have been shown to directly bind to and repress transcription from their own promoters [94-99]. In line with these findings, both upward and downward manipulation of HES/HER protein levels abolishes oscillatory expression of their respective genes. For example, *Hes7* is constitutively upregulated in *Hes7*-null mice and constitutively downregulated when HES7 is stabilized by proteasome inhibitors [94]. Similarly, Her1 and Her7 repress their own and each other's

transcription in zebrafish PSM, as demonstrated by heat shock-driven overexpression studies [97]. In support of a central role for the HES/HER family in the segmentation clock, this class of transcription factors is also involved in the generation of oscillations of other components of the Notch pathway. For instance, *Hes7*-null mice exhibit no oscillatory expression of Notch-based segmentation clock genes [70, 94, 100]. In addition, the oscillatory expression of *Lunatic fringe (Lnfg)*, an important segmentation clock gene in mice and chicks, is directly dependent on the repressive activity of HES7 [70, 94]. Consistent with these findings, reduction of *her1* and *her7* function through morpholino injections eliminates oscillations of *deltaC*, a gene encoding a Notch ligand, in zebrafish embryos [75].

According to mathematical modelling of HES/HER-based negative feedback loops, the time delay between activation and self-repression of HES/HER factors is a key parameter responsible for generating sustained oscillations and determining their period [101, 102]. Specifically, the oscillation period appears to be dictated by the totality of transcriptional and translational delays in the circuit, with mRNA splicing and nuclear export constituting the largest part of the period [103-105]. Consistent with these predictions, deletion of all three introns from the mouse *Hes7* gene completely abolishes its oscillations, while deletion of two introns results in faster but dampened oscillations of *Hes7* [103, 104]. On account of these data, intracellular negative feedback loops centered around HES/HER transcription factors appear to constitute the molecular core of the segmentation clock.

One of the most striking features of periodic gene oscillations in the PSM is their emergence as coherent wave-like patterns at the tissue level. These waves originate in the posterior PSM with a temporal periodicity matching that of somite formation and travel anteriorly before arresting at the anterior end of the PSM (**Fig. 4**). The progression of these patterns remains largely undisturbed even in dissected PSM fragments, suggesting that they are phase waves generated by autonomously oscillating cells with a slight temporal shift in the oscillation rhythm [65, 106]. Indeed, both early static snapshots and later real-time imaging of oscillatory gene expression in several vertebrate species indicate that the oscillation period is not uniform across the PSM. While the oscillation period of posterior PSM cells matches that of somite formation, it gradually increases as these cells progress anteriorly [16, 97, 107-113]. This gradual increase introduces a slight phase-shift in each cell relative to its posterior neighbor, building a phase gradient along the tissue. It is due to this

orderly distribution of phases along the PSM that oscillatory gene expression manifests as traveling waves [16, 65, 97, 114, 115].

While the segmentation clock operates at the single cell level, PSM cells rely on intercellular communication to refine and coordinate their oscillations across the tissue. Supporting this notion, cells dissociated from the PSM of mouse, chick, and zebrafish embryos exhibit less precise oscillations than those within intact tissue, eventually falling out of synchrony with each other [106, 116, 117]. A wealth of evidence indicates that oscillatory gene expression in neighboring PSM cells is synchronized through Notch-dependent intercellular signaling. This phenomenon has been studied primarily in zebrafish, where disruption of Notch signaling results in a gradual loss of synchrony in the posterior PSM, generating a ‘salt-and-pepper’ expression pattern in the tissue [82, 115, 118-120]. In mice, Notch signaling has also been proposed to maintain synchrony among autonomously oscillating PSM cells through an LNFG-mediated *trans*-repression mechanism [121]. In summary, the collective evidence underscores the pivotal role of Notch signaling in sustaining coherent wave patterns in the PSM across different vertebrate species.

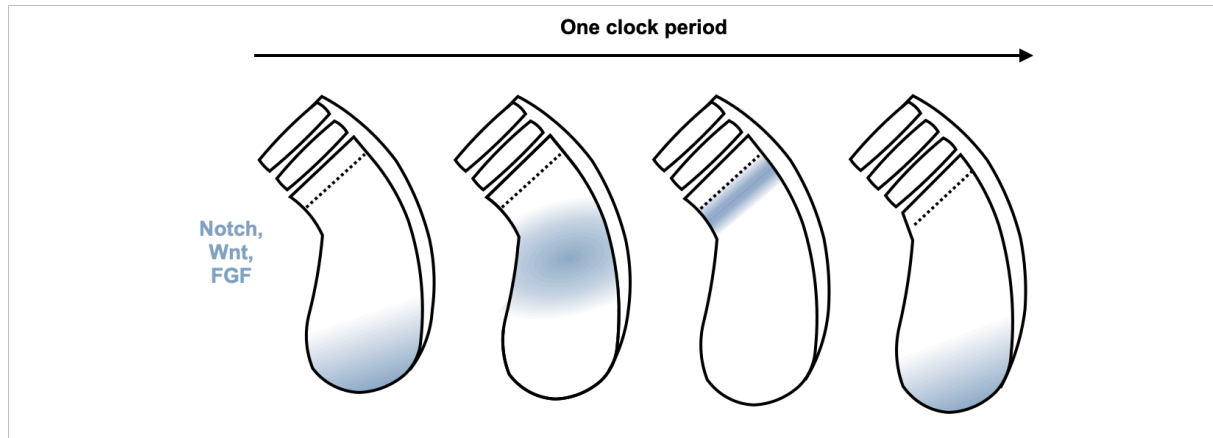


Figure 4. Periodic gene oscillations in the PSM. Genes associated with Notch, FGF, and Wnt signaling pathways exhibit oscillatory expression in the PSM, forming kinematic waves originating from the posterior tip and propagating anteriorly. Each time a wave reaches the anterior end of the PSM, a new pair of somites is formed (dotted lines indicate the anticipated position for the next somite). Lateral view.

Together, these studies have provided compelling evidence linking a clock mechanism in PSM cells to somite segmentation, consistent with the hypothesis of Cooke and Zeeman [62]. Furthermore, these investigations have unveiled an additional aspect of the segmentation clock that was not initially outlined in the clock-and-wavefront model. Specifically, they have demonstrated that individual cells coordinate oscillatory gene expression at the tissue level,

resulting in the formation of traveling wave patterns. How information is encoded at the level of these wave dynamics is discussed in greater detail in **1.3.2**.

1.3.1.2 The wavefront – a system of signaling gradients in the PSM

In the clock-and-wavefront model, the wavefront is essentially an expression of the observation that cells become increasingly differentiated as they assume more anterior positions along the axis. At a specific point in their differentiation path, PSM cells undergo an important transition in their differentiation status, acquiring the competence to segment upon the interaction with the segmentation clock. According to the model's formulation, this transition occurs at a fixed relative position in the anterior PSM, although its absolute position continuously shifts posteriorly in concert with axis elongation [62]. Numerous heat shock-based studies have now demonstrated that segmental determination occurs several somite cycles before the morphological boundary is formed, placing the anterior edge of the wavefront – also referred to as the determination front – more posteriorly than initially envisioned [97, 118, 122-126].

It is now widely accepted that the differentiation of PSM cells is controlled by the combined activity of signaling gradients in the PSM. The FGF and Wnt signaling pathways exhibit peak activity in the posterior tailbud, gradually diminishing toward the anterior, whereas the retinoic acid (RA) signaling pathway displays a graded activity in the opposite direction (**Fig. 5**) [88, 123, 124, 127-133]. A study using mouse and chick embryos has demonstrated that the establishment of the FGF gradient in the PSM relies on a time-dependent decay mechanism. Specifically, the *de novo* transcription of *Fgf8* mRNA is confined to the tailbud, meaning that cells experience a gradual decline in its concentration as they progress anteriorly [128]. The resulting posterior-to-anterior *Fgf8* mRNA gradient is then translated into a corresponding FGF8 protein gradient, which, in turn, correlates with gradients of phosphorylated Akt (in mice) and phosphorylated ERK (in chicks and zebrafish), both downstream effectors of the FGF signaling pathway [36, 128, 129]. Indirect evidence suggests a similar decay-based mechanism for the emergence of the Wnt signaling gradient, as *Wnt3a* transcription is also confined to the tailbud, generating a *Wnt3a* gradient in the PSM [88, 134]. However, a direct visualization of a corresponding *Wnt3a* protein gradient is yet to be achieved. In contrast to FGF and Wnt signaling pathways, the anterior-to-posterior gradient of RA activity is thought to be established through a classical source-sink mechanism. Specifically, the expression of *Raldh2*, an enzyme essential for the synthesis of

RA, is highest in somites and the anterior PSM (source), while Cyp26a1, an enzyme responsible for RA inactivation, is expressed in the tailbud (sink) [133, 135-139]. While FGF and Wnt signaling pathways appear to reinforce each other, the FGF and RA signaling pathways are mutually inhibitory [88, 127, 134, 140-144]. Functionally, the high activity of FGF and Wnt signaling in the tailbud has been linked to the maintenance of an undifferentiated progenitor state in several vertebrate species [123, 127, 129, 140, 141, 145]. As cells exit the tailbud and begin their journey towards the anterior PSM, exposure to RA signaling (accompanied by a gradual decline in FGF and Wnt signaling activity) induces their differentiation, ultimately resulting in the formation of a new somite pair [132, 141, 146].

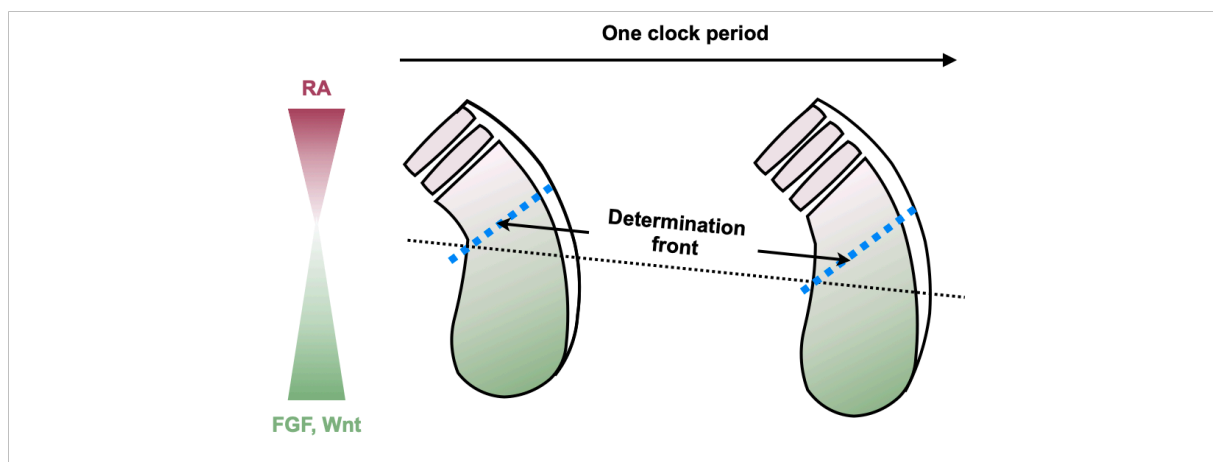


Figure 5. Signaling gradients in the PSM. FGF and Wnt signaling activity is high in the posterior PSM, gradually diminishing towards the anterior PSM. Conversely, RA signaling activity is high in the somitic region and the anterior PSM, gradually diminishing towards the posterior PSM. The combined activity of these signaling gradients determines the position of the determination front (indicated by blue dotted lines). While the relative position of the determination front remains constant in the anterior PSM, its absolute position regresses along the anteroposterior axis over time (indicated by a thin dotted line). Lateral view.

Several lines of evidence support the hypothesis that the combined activity of FGF, Wnt, and RA signaling gradients delimits the position of the determination front. Implantation of FGF8-soaked beads in the posterior PSM of chick and zebrafish embryos leads to smaller somite formation anterior to the bead, while pharmacological inhibition of the FGF signaling pathway results in larger somite formation [123, 129]. Likewise, implantation of Wnt3a-overexpressing cells in the posterior chick PSM shifts the position of future somite boundaries anteriorly, so that smaller somites are formed [88]. In zebrafish, inhibition of Wnt signaling through overexpression of Dkk1 has also been found to give rise to smaller somites, while Wnt activation through overexpression of Wnt3a leads to an opposite result [124]. Finally, local overexpression of FGF8 in chick and zebrafish embryos and constitutive activation of Wnt in mouse PSM have been shown to shift the position of oscillation arrest anteriorly in the

PSM, suggesting that these signaling pathways maintain cells in an immature oscillating state [123, 127, 129]. In contrast, inhibition of Wnt signaling in zebrafish embryos shifts the position of oscillation arrest posteriorly [124]. Together, these studies have shown that manipulation of FGF and Wnt signaling gradients can displace the position of the determination front, giving rise to abnormally sized somites. Therefore, consistent with the clock-and-wavefront model, the activity of this system of gradients appears to set the spatial periodicity for somite boundary formation by conferring positional information to cells along the PSM.

1.3.2 The phase-shift model

In 1969, Goodwin and Cohen proposed the phase-shift model to explain the emergence of periodic patterns in developing systems, introducing the idea that both temporal and spatial information can be embedded within the properties of the oscillator. The phase-shift model postulates the existence of two oscillating signals originating from a source and propagating through the tissue in a wave-like manner with distinct dynamics. The relative phase-shift between these signals, and hence the temporal discrepancy between their arrival, changes based on the distance from the source. Consequently, cells can map their relative position within the tissue by interpreting the temporal gap between the two signals, effectively converting temporal information into spatial cues [63].

Experimental evidence from our lab using real-time reporters has demonstrated that space can be encoded through phase differences between PSM cells, providing conceptual support for the phase-shift-based patterning model in the context of somitogenesis. In a study by Lauschke et al., real-time imaging of oscillatory gene expression was combined with an *ex vivo* segmentation assay that recapitulates key aspects of somitogenesis in a quasi-monolayer of mouse primary PSM cells (mPSM). In this assay, oscillations initially manifest as pulses, followed by the emergence of characteristic phase-shifted waves of expression. These waves propagate from the tissue center towards the periphery, where they come to a halt, coinciding with segment formation. Thus, in this experimental setup, the central-to-peripheral axis of the mPSM represents the anteroposterior axis of the intact PSM in embryos. With no growth in the tissue, segmentation gradually diminishes the available mPSM, leading to the formation of progressively smaller segments, akin to somite scaling in size-reduced embryos. Notably, a detailed analysis of oscillatory dynamics in the mPSM uncovered a persistent 2π phase-shift

between central and peripheral cells, indicating that the phase-shift between neighboring cells increases as the available tissue diminishes, resulting in a steeper phase gradient slope over time. Importantly, the observed phase-shift between cells was found to faithfully predict future segment size, suggesting that the phase gradient slope may harbor crucial information for somite scaling [16].

A subsequent investigation conducted by Sonnen et al. proposed that cells can decode this phase-shift relative to a second oscillator within the same cell, aligning with the model presented by Goodwin and Cohen [63, 147]. Through simultaneous imaging of Notch and Wnt signaling reporters in mPSM cultures, the study revealed that the relative phase relationship between these signals changes as a function of space, transitioning from an out-of-phase configuration in the center to an in-phase configuration in the periphery. This is due to distinct oscillation dynamics of Notch and Wnt signaling pathways in the tissue, with Wnt oscillations traversing the tissue more rapidly. Notably, experimental manipulations altering the phase relationship between these pathways in the periphery of the mPSM through a microfluidics-based entrainment approach resulted in a delayed arrest of oscillations, leading to prolonged oscillatory state in peripheral cells compared to controls. Remarkably, this manipulation impaired segment formation and segment polarity, providing functional evidence that the phase-shift between Notch and Wnt signaling encodes information for proper PSM segmentation in *ex vivo* culture [147].

1.4 Integration of anteroposterior axis elongation and segmentation

The concomitant nature of axis elongation and segmentation raises the question as to how these processes are integrated in the broader context of embryonic development to ensure the formation of an accurate number of somites that are size-adjusted in proportion to the overall embryo size. Throughout the years, it has become apparent that a handful of conserved signaling pathways can orchestrate a wide variety of developmental processes by imparting high-content biological information to the developing embryo by the means of dynamic signaling [148]. In the context of anteroposterior axis patterning, both axis elongation and segmentation are controlled by a network of overlapping signaling pathways – specifically, Notch, FGF, Wnt, and RA. Notably, accumulating evidence indicates that the FGF signaling pathway may exert influence over both axis elongation (conjointly with Wnt and RA signaling pathways) and the oscillations of the Notch signaling pathway in the PSM, providing a possible node for integration. In this chapter, I provide an overview of studies that look into these roles of FGF signaling during anteroposterior axis patterning and propose a hypothesis that it serves as a connecting link between axis elongation and segmentation.

1.4.1 FGF signaling gradient controls axis elongation

As introduced in **1.2**, distinct cell behaviors are invoked in a tissue- and species-specific manner to power axis elongation during the formation of the secondary body. For example, the predominant cell behavior contributing to axis elongation in amniote embryos is cell proliferation, whereas zebrafish embryos are heavily dependent on convergent extension. Interestingly, manipulations of FGF signaling result in axis elongation defects across vertebrate species, irrespective of which individual cell behavior is the most prevalent [140, 149, 150]. In mouse and chick embryos, FGF signaling plays a crucial role in preserving the undifferentiated state of tailbud progenitors. It achieves this by creating an RA-free environment, thereby protecting them from signals that induce differentiation [140, 149-152]. In chick, FGF has also been implicated in controlling cell motility in the PSM, as both upward and downward manipulation of FGF signaling disrupts the motility gradient and decelerates axis elongation [37]. In zebrafish, on the other hand, FGF signaling propels axis elongation by regulating convergent extension movements rather than cell proliferation, as pharmacological inhibition of FGF signaling during secondary body formation shortens the length of the

posterior tail without affecting its volume [35]. These collective findings underscore the conserved functional role of FGF signaling in driving axis elongation, even though it instructs different downstream cell behaviors depending on the organism under consideration.

1.4.2 FGF signaling gradient acts upstream of the segmentation clock

In the classical formulation of the ‘clock-and-wavefront’ model, the clock and the wavefront are regarded as two independent entities responsible for setting the temporal and spatial periodicity of somitogenesis, respectively. Early experimental studies supported this concept by showing that displacing the determination front (i.e., the wavefront) through FGF signaling modulation affects somite size but not the rhythm of somitogenesis (i.e., the clock) [123, 129]. However, it is important to acknowledge that oscillation periods are graded along the PSM, giving rise to wave-like expression patterns. Accumulating evidence suggests that while FGF signaling may not influence the posterior period (which matches the period of somitogenesis), it does impact the wave dynamics in the PSM [153-156]. Of note, recent findings from our lab using an *ex vivo* mouse somitogenesis assay revealed that a localized increase in FGF8b ligand concentration results in a shallower phase gradient on the manipulated side, causing the wave to traverse the tissue more rapidly. Based on these data, it was proposed that FGF signaling controls the evolution of the oscillation phase-shift in the PSM [155]. Importantly, these observations challenge the conventional view that the clock and the wavefront operate independently of each other by showing that FGF signaling, which is traditionally thought to define the position of the wavefront, acts upstream of the clock, modulating oscillations in the PSM at the level of phase.

1.5 Medaka as a model system to study robust patterning

To pursue questions related to robust patterning, it is essential to have a model that allows for the perturbation and monitoring of both axis elongation and signaling dynamics *in vivo*. This is possible in the small oviparous freshwater teleost fish medaka (*Oryzias latipes*), which combines the power of several complementary approaches, including surgical manipulations, the generation of transgenic and knock-in lines, and real-time imaging (refer to **1.5.1**). On top of that, certain aspects of anteroposterior axis patterning in medaka resemble the development of amniote embryos more than that of zebrafish embryos, making it a particularly interesting system for comparative evolutionary studies (refer to **1.5.2**).

1.5.1 Experimental advantages provided by the medaka embryo

Medaka embryos serve as a valuable experimental system for developmental biologists, offering several important advantages. First, they are transparent throughout embryogenesis and can be staged under the microscope according to a set of detailed morphological criteria described by Iwamatsu [157]. Importantly, this optical clarity, combined with the oviparous mode of development, makes medaka embryos suitable for *in vivo* imaging. Second, medaka embryos develop rather rapidly compared to most of the other vertebrate model systems, hatching within 7-14 days post-fertilization when grown at 27°C. This accelerated pace of development provides an opportunity to follow many developmental processes from start to finish. Furthermore, medaka embryos can tolerate a wide range of temperatures (4-35°C) in a stage-specific manner, allowing researchers to modulate the speed of their development by adjusting the incubation temperature. Third, with a diameter of approximately 1 mm, medaka embryos are sufficiently large for classical embryological manipulations, such as microinjection at the 1-cell stage or aspiration of blastula cells. Finally, embryos from the same mother develop rather synchronously, making stage-matched embryos readily available for experiments.

From a technical standpoint, medaka is exceptionally well suited for developmental biology studies due to its powerful genetics. Medaka has a relatively small genome of about 700 Mb, which is less than half the size of the zebrafish genome (about 1500 Mb) [158, 159]. Unlike other vertebrates, medaka fish are extremely tolerant to inbreeding, allowing the elimination of genetic variability as a confounding factor in interpreting experimental results.

In addition, due to their tolerance to inbreeding, a collection of 200 nearly isogenic medaka lines has been established from wild-caught individuals, providing the community with a valuable resource for dissecting genotype-environment-phenotype interactions during embryonic development [160]. Crucially, in recent years the community has also benefited from the establishment of highly efficient CRISPR/Cas9-mediated genome editing protocols, enhancing the efficiency of generating reporter lines and enabling real-time observation of developmental processes [161, 162].

1.5.2 Medaka anteroposterior axis patterning as a system for comparative developmental biology

Many of the technical advantages listed above are also offered by another popular teleost model, the zebrafish. However, significant biological differences exist between the two species. This is perhaps not surprising, given the estimation that their genomes have been evolving independently for about 230 million years (for comparison, mice and humans are separated by about 90 million years of independent evolution) [163]. Paired with a whole-genome duplication event at the base of the teleost radiation around 350 million years ago, this has resulted in differential inactivation, sub-functionalization, and neo-functionalization of their regulatory elements and genes [163]. Indeed, large-scale mutagenesis screens in zebrafish and medaka have isolated mutants with unique phenotypes in both species, including mutants with defective somitogenesis [164-167]. In the context of somitogenesis, important differences are also observed in the distribution of *her* gene transcripts in zebrafish and medaka PSMs. In zebrafish, the posterior U-shaped *her* expression domain gradually disappears with each somite formation cycle, whereas in medaka, it remains stable throughout somitogenesis. What is more, *her* genes exhibit a characteristic two or three-stripe pattern in the zebrafish PSM, while only a single stripe of expression is observed in medaka. The latter pattern more closely resembles the expression of *her* orthologues in mouse and chick embryos, suggesting a divergence in the segmentation mechanism in zebrafish or alternatively, a convergence in medaka and amniotes.

Considering the apparent connection between volumetric growth and maternal energy supply, it is interesting to see how the mechanisms that drive axis elongation in medaka compare to those in zebrafish and amniotes. While both medaka and zebrafish are oviparous, the yolk-to-embryo ratio is higher in medaka, suggesting that medaka embryos have access to

a more substantial energy supply [168]. Upon hatching, zebrafish larvae lack the ability to swim and forage independently, and therefore rely on nutrients in the remaining yolk to complete morphogenesis and acquire full sensory, motor, and digestive functions [169-174]. To avoid starvation in food-deprived environments, zebrafish larvae are forced to complete morphogenesis rapidly, which selects against time-consuming mechanisms based on volumetric growth. Although it is not known whether this constraint on volumetric growth has been lifted in medaka, medaka are known to hatch as freely swimming and feeding young adults [175, 176]. Consequently, they initiate exogenous feeding while their yolk sac is still largely unabsorbed, providing an opportunity for volumetric growth. Therefore, by blending aspects of both anamniote and amniote development, medaka emerges as an exciting complementary system for studying anteroposterior axis patterning.

1.6 Aims of the study

This thesis aims to explore the robust patterning of the anteroposterior axis in medaka, focusing on two fundamental, concomitant processes – axis elongation and somite segmentation. While oscillatory gene expression dynamics associated with somite segmentation have already been documented in medaka, our understanding of axis elongation in this species and the possible integration of axis elongation and somite segmentation in the broader context of vertebrate development is lacking. To address this, this thesis is guided by two major objectives.

The first objective is to obtain a tissue-level description of axis elongation dynamics in medaka, with a particular emphasis on the PSM tissue. This involves real-time imaging and image segmentation to address the following key questions:

- 1) Is the process of anteroposterior axis elongation accompanied by volumetric growth?
- 2) Do different tissues within the embryo contribute differently to axis elongation and volumetric growth?
- 3) Which cellular behaviors account for axis elongation and volumetric growth?

The second objective is to explore the integration of axis elongation and somite segmentation in the PSM, with a particular emphasis on tissue-level oscillatory gene expression dynamics. This involves manipulation of PSM length and axis elongation through surgical and pharmacological interventions to address the following key questions:

- 1) How does the perturbation of PSM length and axis elongation impact somite segmentation at the morphological level? Does the length of somites scale to the reduced PSM length, and how fast does scaling occur?
- 2) How does the perturbation of PSM length and axis elongation impact somite segmentation at the level of underlying oscillatory gene expression dynamics? Which, if any, dynamic features of oscillatory gene expression scale with the reduced PSM length?

2 Results

2.1 Quantification of tissue-specific behaviors during secondary body formation

Anteroposterior axis elongation relies on a combination of cell rearrangement- and volumetric growth-based behaviors that are utilized to different degrees in a species- and tissue-specific manner. Axis elongation has not yet been studied in medaka and thus the goal of this section is to use the medaka tail explant system to obtain tissue-level understanding of different cell behaviors involved in axis elongation during secondary body formation. The first part of this section is dedicated to introducing the medaka tail explant system and the image analysis strategy to segment individual tissues from time-series microscopy data. This is followed by a descriptive analysis of the dynamics of tissue-specific elongation and volumetric growth during secondary body formation. In addition to providing valuable comparative insight into the evolution of vertebrate axis elongation in and of itself, this knowledge is also of key importance in designing perturbation strategies to study the integration between axis elongation and somite patterning, which is covered in **2.2**.

2.1.1 Visualization and segmentation of distinct tissues using the tail explant system

In vivo imaging of secondary body formation in medaka embryos is made difficult by two major factors. First, a thin layer of stellate-shaped cells covering the yolk sac undergo Ca^{2+} -driven rhythmic contractions at Iwamatsu stages 14-24 (from mid-epiboly to 16 ss), causing extensive rotation of the embryo [177-179]. Second, the anteroposterior axis elongates along the curve of the yolk sac, making it difficult to capture the entire volume of the secondary body over time using confocal microscopy. As an alternative to *in vivo* imaging, embryonic tails can be separated from the rest of the embryonic body and the yolk sac, and cultured *ex vivo* under the confocal microscope (**Fig. 6A**). Importantly, removal of the yolk sac in this simplified system effectively eliminates the problem of embryo rotation. In addition, tail explants can be flat-mounted with their lateral side facing the objective, allowing for imaging of the elongating secondary body along the *xy*-plane, rather than the *z*-axis in dorsally-mounted whole embryos (**Fig. 6B,C**). Owing to these advantages, I chose to

use the tail explant system to quantitatively study the mechanisms driving axis elongation during secondary body formation.

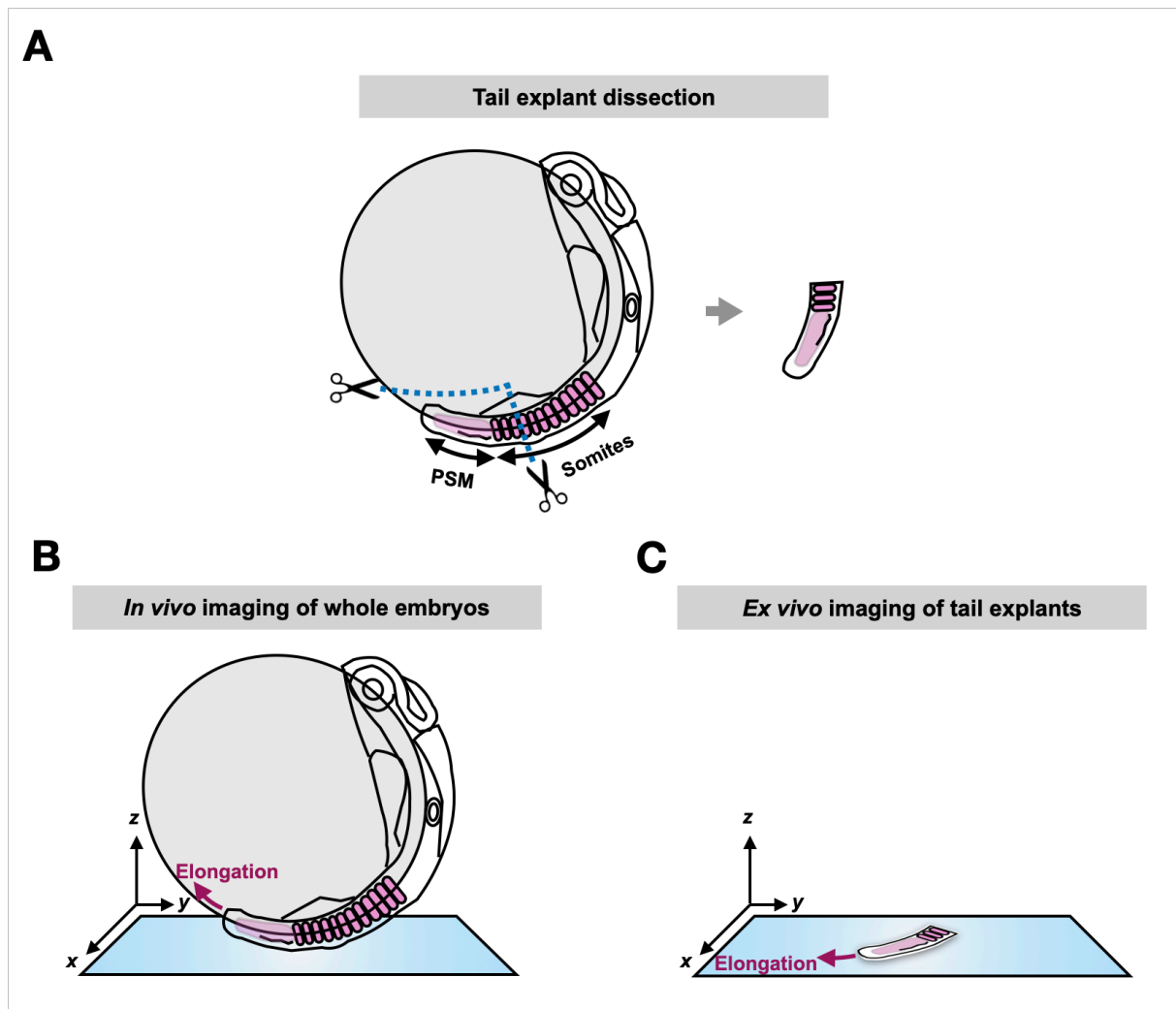


Figure 6. Schematic illustration of the tail explant system.

(A) The tail explant system involves dissecting embryonic tails at Iwamatsu stage 23 (12-14 ss) by introducing two cuts in the embryo. One cut separates the tail from the yolk sac and another cut, positioned 2-5 somites above the PSM, separates the tail from the rest of the embryo (indicated by blue dotted lines).

(B) For *in vivo* imaging, medaka embryos are positioned with their dorsal side facing the glass-bottom dish. In this configuration, the secondary body elongates along the yolk sac in the *z*-axis direction, making it challenging to capture the entire secondary body volume over time.

(C) For *ex vivo* imaging, tail explants are mounted with their lateral side facing the glass-bottom dish. In this configuration, the secondary body elongates in the *xy*-plane, ensuring a constant number of *z*-slices and allowing to capture the entire secondary body volume over time.

To visualize different tissues in the tail explant, I used two medaka lines available in our lab: (1) *mScarlet-pcna*, an endogenous knock-in reporter for the expression of proliferating cell nuclear antigen (Pcna), and (2) *Tg(brachyury:Venus)*, a transgenic reporter for the activity of the *brachyury* promoter. Previous studies have shown that the *mScarlet-*

pcna line acts as an organismal-wide reporter for proliferating cells, while the *Tg(brachyury:Venus)* line labels the notochord [162, 180]. Upon examining the expression of mScarlet-Pcna and Venus in *mScarlet-pcna*^{+/-}; *Tg(brachyury:Venus)*^{+/-} double-heterozygous tail explants, I noticed that the mScarlet-Pcna fusion protein was expressed in the nuclei throughout the secondary body, resembling a ubiquitous nuclear label (**Fig. 7A**). Unexpectedly, Venus was expressed not only in the notochord, but also throughout the paraxial mesoderm, albeit at noticeably lower levels (**Fig. 7A,B**). Consistently, the intensity histogram of the selected region shown in **Fig. 7B** showed three distinct peaks, the lowest one corresponding to the neural tube/background, the middle one corresponding to the paraxial mesoderm, and the highest one corresponding to the notochord (**Fig. 7C**). Owing to these patterns of expression, I was able to visually distinguish three distinct tissues in *mScarlet-pcna*^{+/-}; *Tg(brachyury:Venus)*^{+/-} tail explants. Specifically, the paraxial mesoderm expressed mScarlet-Pcna and low levels of Venus, the notochord expressed mScarlet-Pcna and high levels of Venus, whereas the neural tube expressed mScarlet-Pcna, but no Venus.

Next, I developed a two-part image analysis strategy to generate time-resolved 3D surface reconstructions of individual tissues using *mScarlet-pcna*^{+/-}; *Tg(brachyury:Venus)*^{+/-} tail explant data as an input. In the first part, I used a machine learning-based pixel classification tool called Labkit to categorize each pixel in the input image into one of the predefined classes (e.g., ‘background’, ‘paraxial mesoderm’, ‘neural tube’, etc.) [181]. This generated a multi-channel file, where each channel represented a probability map indicating the confidence of each pixel belonging to a specific class (**Fig. 8A**). In the second part, I imported this file into Imaris software and created 3D surface reconstructions of individual tissues by using the corresponding probability map channels as input for the segmentation algorithm (**Fig. 8B**). The resulting time-resolved 3D surface reconstructions were then used to quantify elongation and volumetric growth occurring in different tissues of the tail explant, as detailed in **2.1.2**.

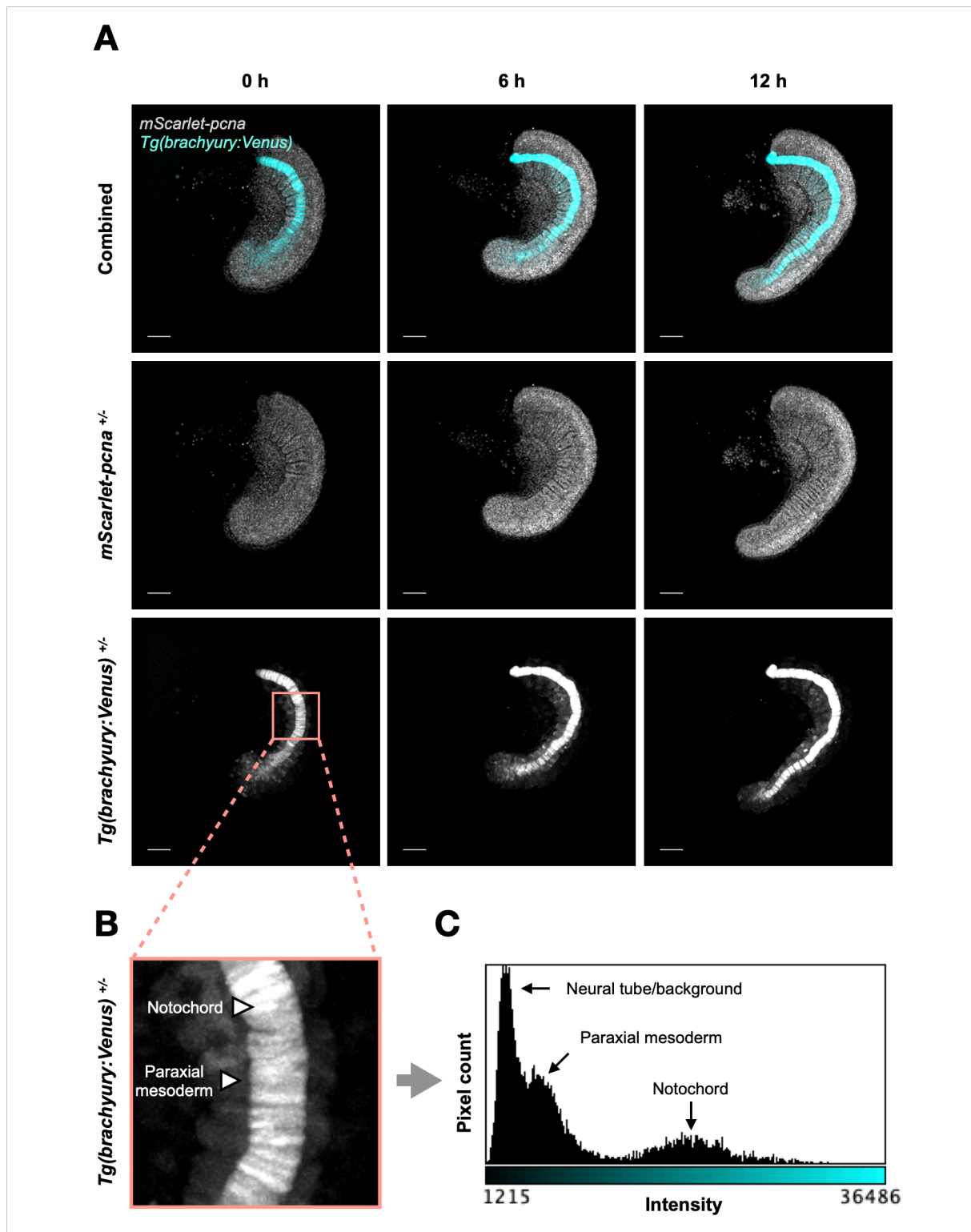


Figure 7. Visualization of different secondary body tissues over time in *mScarlet-pcna*^{+/-}; *Tg(brachyury:Venus)*^{+/-} tail explants.

(A) Maximum intensity projections of *mScarlet-pcna* and *Tg(brachyury:Venus)* channels in a representative tail explant at 0 h, 6 h and 12 h after the onset of imaging. Scale bars: 50 μ m.

(B) A closer view of the *Tg(brachyury:Venus)* channel in a magnified region from (A). Strong Venus expression marks the notochord, while weaker Venus expression marks the paraxial mesoderm. Notably, Venus is not expressed in the neural tube.

(C) A histogram depicting Venus intensity values in (B), revealing three peaks corresponding to the paraxial mesoderm, notochord and neural tube/background.

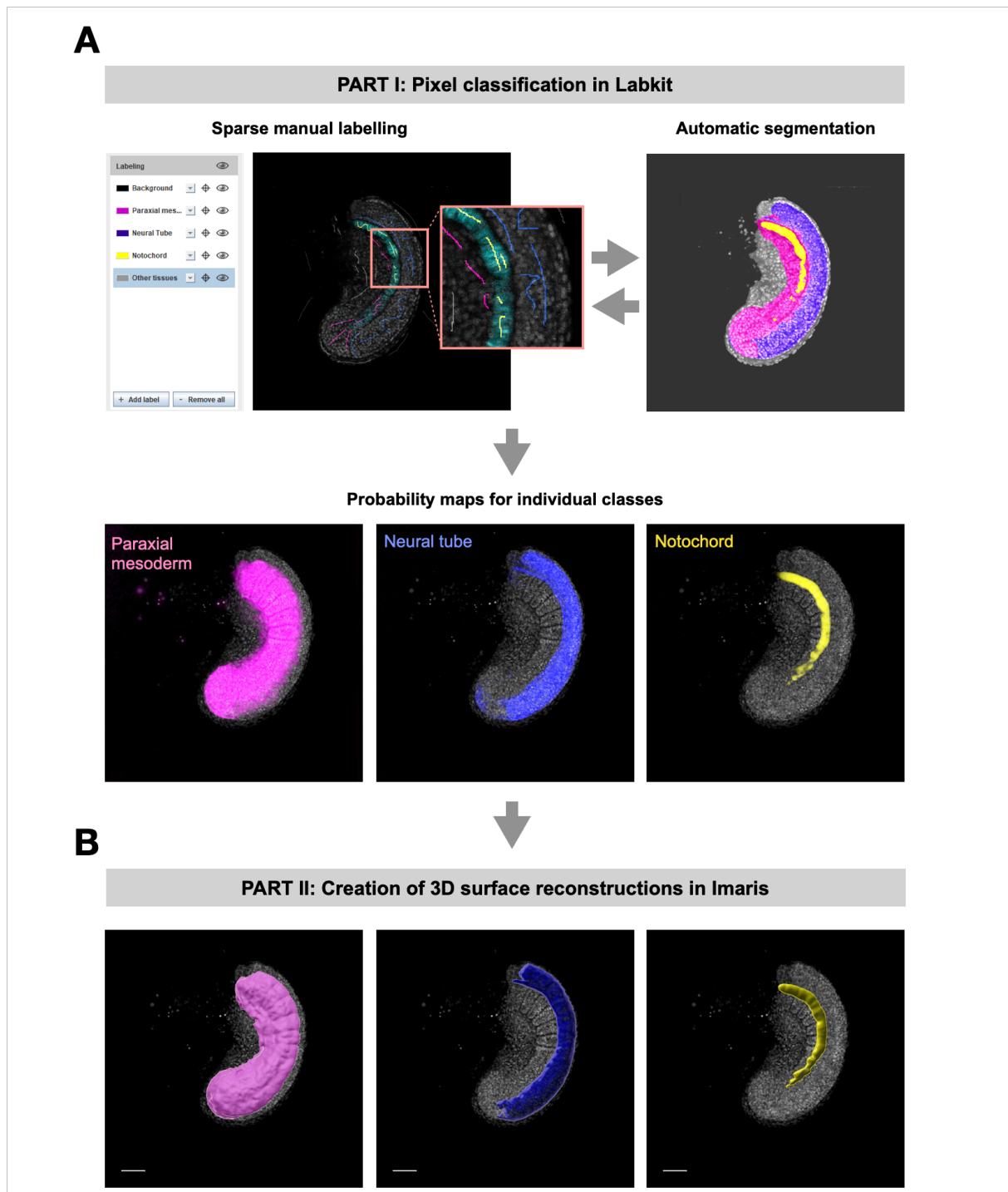


Figure 8. Image analysis workflow for 3D surface reconstruction of individual tissues.

(A) Individual tissues are labelled using Fiji/ImageJ plugin, Labkit [181]. A few pixels spanning different z-slices and time points are manually labelled by drawing scribbles over them (as shown in the inset), assigning them to one of the defined classes (in this particular example, these classes are: ‘Background’ in dark grey, ‘Paraxial mesoderm’ in magenta, ‘Neural tube’ in blue, ‘Notochord’ in yellow and ‘Other tissues’ in light grey). These labels are then used to train a random forest classifier, which is applied to the entire image to automatically assign all remaining pixels to one of the defined classes. Upon visual inspection of classification results, the labelling and automatic segmentation steps are iterated until a segmentation of desirable quality is achieved. Then, a probability map indicating the confidence of pixels belonging to a certain class is generated for each class.

(B) 3D tissue surface reconstructions are created using Imaris software. Probability maps corresponding to individual tissues are used as source channels for the automatic segmentation algorithm, producing 3D renderings of individual tissues. Scale bars: 50 μm .

2.1.2 Elongation and volumetric growth dynamics in tail explants

The extent to which volumetric growth-based mechanisms accompany secondary body elongation is thought to depend on the amount of nutrients available to the embryo [19, 35]. As medaka embryos appear to have a larger nutrient reserve than zebrafish but a smaller one than amniotes, I hypothesized that they would exhibit a corresponding trend in volumetric growth during secondary body formation. To test this hypothesis, I segmented the secondary body in *mScarlet-pcna*^{+/-}; *Tg(brachyury:Venus)*^{+/-} tail explants and quantified its elongation and volumetric growth over a 12-hour period (**Fig. 9A**). The data showed a continuous elongation of the secondary body, with tail explants accumulating a total length increase of $61.84 \pm 2.53\%$ ($n = 4$). Similarly, the secondary body continuously grew in volume, accumulating a total increase of $26.70 \pm 6.73\%$ ($n = 4$). Taken together, these findings demonstrate that axis elongation during secondary body formation in medaka tail explants is accompanied by volumetric growth.

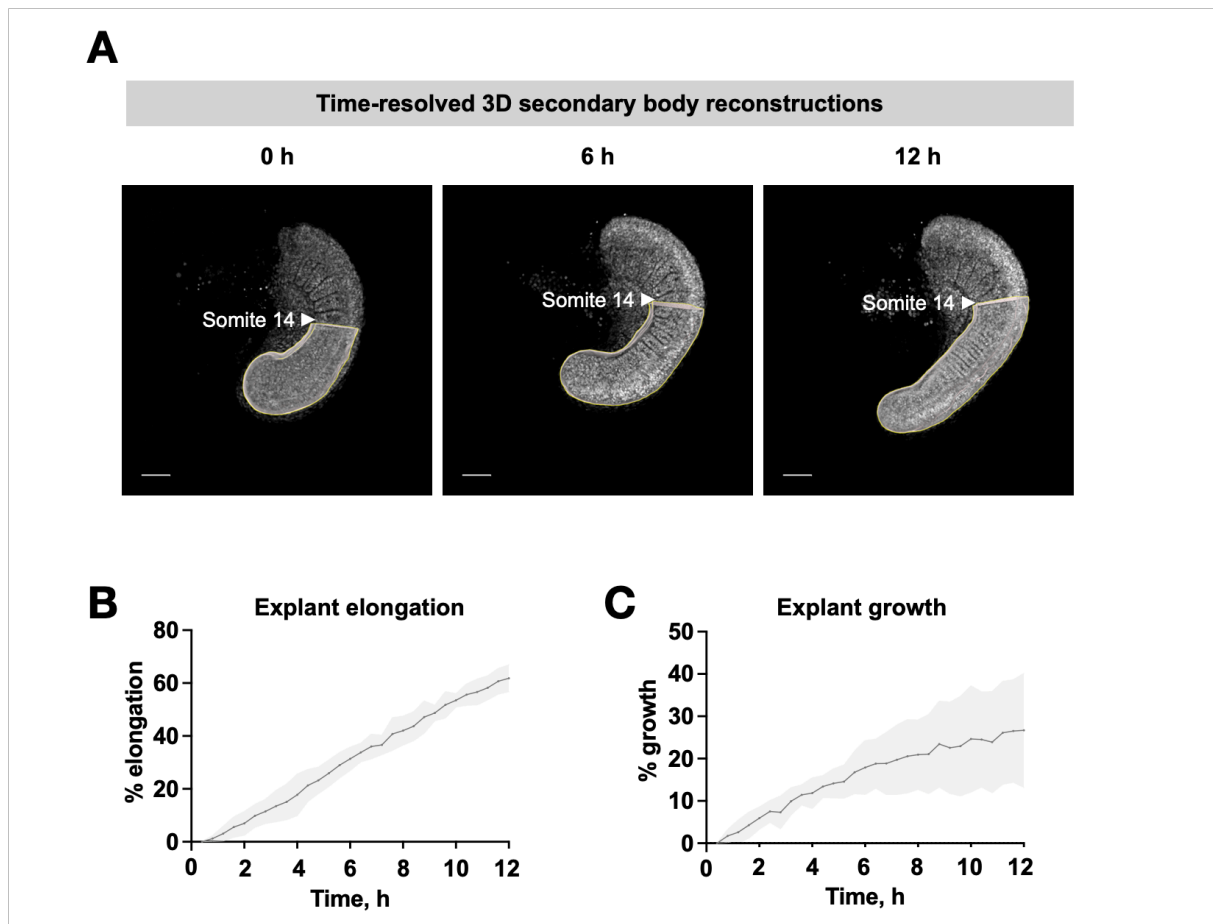


Figure 9. Dynamics of elongation and volumetric growth in the secondary body.

(A) 3D surface reconstructions of the secondary body in a representative tail explant during axis elongation (0 h, 6 h, and 12 h after the onset of imaging), overlaid on the mScarlet-Pcna channel. Somite 14 marks the nascent somite at the onset of imaging. Scale bars: 50 μ m.

(B, C) Percentage elongation (B) and percentage volumetric growth (C) in the secondary body plotted against time ($n = 4$, the data is presented as mean \pm SD).

Axis elongation is a complex process involving multiple tissues, each undergoing a combination of cell rearrangement- and volumetric growth-based behaviors [13, 17, 18]. To characterize elongation and volumetric growth dynamics in *mScarlet-pcna*^{+/-}; *Tg(brachyury:Venus)*^{+/-} tail explants in a tissue-specific manner, I created 3D surface reconstructions and measured the length and volume of the paraxial mesoderm, neural tube and notochord tissues over time (Fig. 10A). The morphometric analysis revealed a continuous increase in both length and volume for each of these tissues. Specifically, the paraxial mesoderm exhibited a $38.86 \pm 8.19\%$ ($n = 3$) increase in length and a $33.50 \pm 21.09\%$ ($n = 3$) increase in volume. The neural tube showed a $41.60 \pm 11.19\%$ ($n = 3$) increase in length and a $30.43 \pm 10.59\%$ ($n = 3$) increase in volume. Finally, the notochord displayed a $56.40 \pm 8.69\%$ ($n = 3$) increase in length and a substantial $117.88 \pm 44.33\%$ ($n = 3$) increase in volume (Fig. 10B,C). While the fold increase in length after 12 hours of imaging was similar among the

three tissues (1.39 ± 0.08 ($n = 3$), 1.42 ± 0.11 ($n = 3$), and 1.56 ± 0.87 ($n = 3$) for the paraxial mesoderm, neural tube, and notochord, respectively), the notochord exhibited a significantly larger fold increase in volume (2.18 ± 0.44 ($n = 3$)) compared to the paraxial mesoderm (1.34 ± 0.21 ($n = 3$)) and neural tube (1.30 ± 0.11 ($n = 3$)) tissues (**Fig. 10D,E**).

To assess the individual contributions of different tissues to the overall volumetric growth in the tail explant, I tracked volume changes in the paraxial mesoderm, neural tube, and notochord tissues as a percentage of the overall tail explant volume over time. Throughout the 12-hour observation period, the relative sizes of these tissues remained consistent, with the paraxial mesoderm constituting the largest part of the tail explant volume, averaging 60.87%. The neural tube accounted for 19.54% of the total volume, while the notochord contributed a relatively smaller proportion at 4.99% (**Fig. 10F**). Due to these variations in relative tissue sizes, the paraxial mesoderm generated more additional volume than the neural tube in absolute terms ($5.05 \times 10^5 \pm 3.29 \times 10^5 \mu\text{m}^3$ ($n = 3$) and $1.53 \times 10^5 \pm 4.85 \times 10^4 \mu\text{m}^3$ ($n = 3$), respectively), despite the similar fold volume change between the two tissues (**Fig. 10E,G**). Additionally, while the notochord exhibited the largest fold volume increase, it contributed the least in absolute volume ($1.00 \times 10^5 \pm 929 \mu\text{m}^3$, ($n = 3$)), owing to its relatively small share of the overall tail explant volume (**Fig. 10E,G**). In summary, these results underscore tissue-specific differences in volumetric growth, emphasizing the paraxial mesoderm as the primary contributor to the overall volumetric growth in the tail explant.

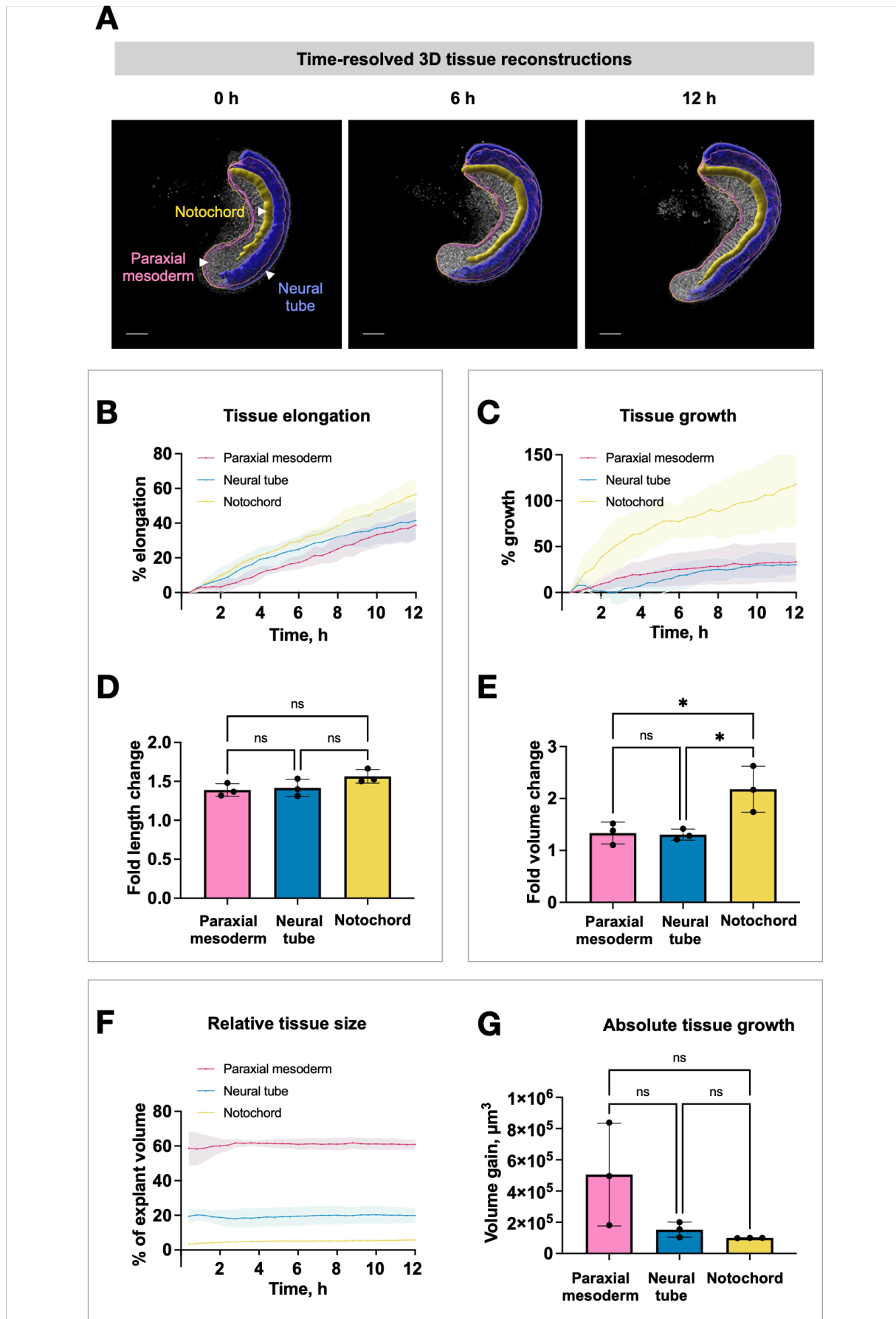


Figure 10. Dynamics of elongation and volumetric growth in distinct tissues during secondary body formation.

(A) 3D surface reconstructions of the paraxial mesoderm, neural tube and notochord tissues in a representative tail explant during axis elongation (0 h, 6 h, and 12 h after the onset of imaging), overlaid on the mScarlet-Pcna signal. Scale bars: 50 μ m.

(B, C) Percentage elongation (B) and percentage volumetric growth (C) in the paraxial mesoderm, neural tube and notochord tissues plotted against time (n = 3, the data is presented as mean \pm SD).

(D, E) Fold length change (D) and fold volume change (E) in the paraxial mesoderm, neural tube and notochord tissues after 12 h of imaging (n = 3, the data is presented as mean \pm SD).

(F) Volume of the paraxial mesoderm, neural tube and notochord tissues as a percentage of whole tail explant volume plotted against time (n = 3, the data is presented as mean \pm SD).

(G) Absolute volume gained by the paraxial mesoderm, neural tube and notochord tissues after 12 h of imaging (n = 3, the data is presented as mean \pm SD; the observed large SD can be explained by differences in the amount of tissue present in each tail explant at the start of imaging, depending on where the cut was made during dissection)). Statistical significance was determined by ordinary one-way ANOVA: ns, not significant $P > 0.05$; * $P < 0.05$.

Based on the position of cells in their differentiation path, paraxial mesoderm tissue can be further subdivided into segmented somites and an unsegmented PSM. Regulation of the length of the latter tissue is central to robust patterning of the anteroposterior axis and is achieved by a carefully balanced activity of two key processes – segmentation and elongation. While the length of the PSM generally decreases during secondary body formation, this does not necessarily mean that the tissue is not undergoing elongation *per se* [10, 107]. As somites continuously bud off from the anterior end of the PSM, any length gained by the PSM during one somite formation cycle may be counterbalanced by the length lost to segmentation. To gain a better understanding of PSM elongation and volumetric growth dynamics in medaka embryos, it is important to quantify them in both net and gross terms.

To measure net elongation and volumetric growth in the PSM, I created 3D surface reconstructions of the PSM (**Fig. 11A**). As expected, a continuous decrease in PSM length and volume was observed over a 12-hour imaging period, with the length decreasing by a total of $32.26 \pm 4.03\%$ (n = 3) and the volume decreasing by a total of $50.37 \pm 7.99\%$ (n = 3, **Fig. 11B,C**).

To evaluate the gross elongation and volumetric growth in the PSM, I combined measurements of both the PSM and the somites it gave rise to, while excluding any elongation and volumetric growth occurring in somites after their formation. As described in Thomson et al., this was done by summing the length/volume values for the following tissues at each consecutive somite stage: the PSM, the nascent somite, and all preceding nascent somites at the time of their formation [182]. Morphometric analysis revealed a trend of reduction in nascent somite length and volume with each consecutive somite formation cycle (**Fig.**

11A,D,E). Since previous research has suggested that somite size scales with PSM size, these findings are in agreement with the observed net decrease in PSM length and volume over time. Calculation of the gross elongation in the PSM revealed that its length increased by 47.39 ± 11.21 % ($n = 3$) during a 12-hour imaging period, indicating that the medaka PSM does undergo elongation over time (**Fig. 11F**). On the other hand, the gross volume of the PSM decreased by 40.66 ± 3.06 % ($n = 3$, **Fig. 11G**). Given that the gross elongation of the tissue was associated with volumetric shrinkage, it appears that the primary mechanism driving axis elongation in the medaka PSM is likely based on cell rearrangements rather than volumetric growth.

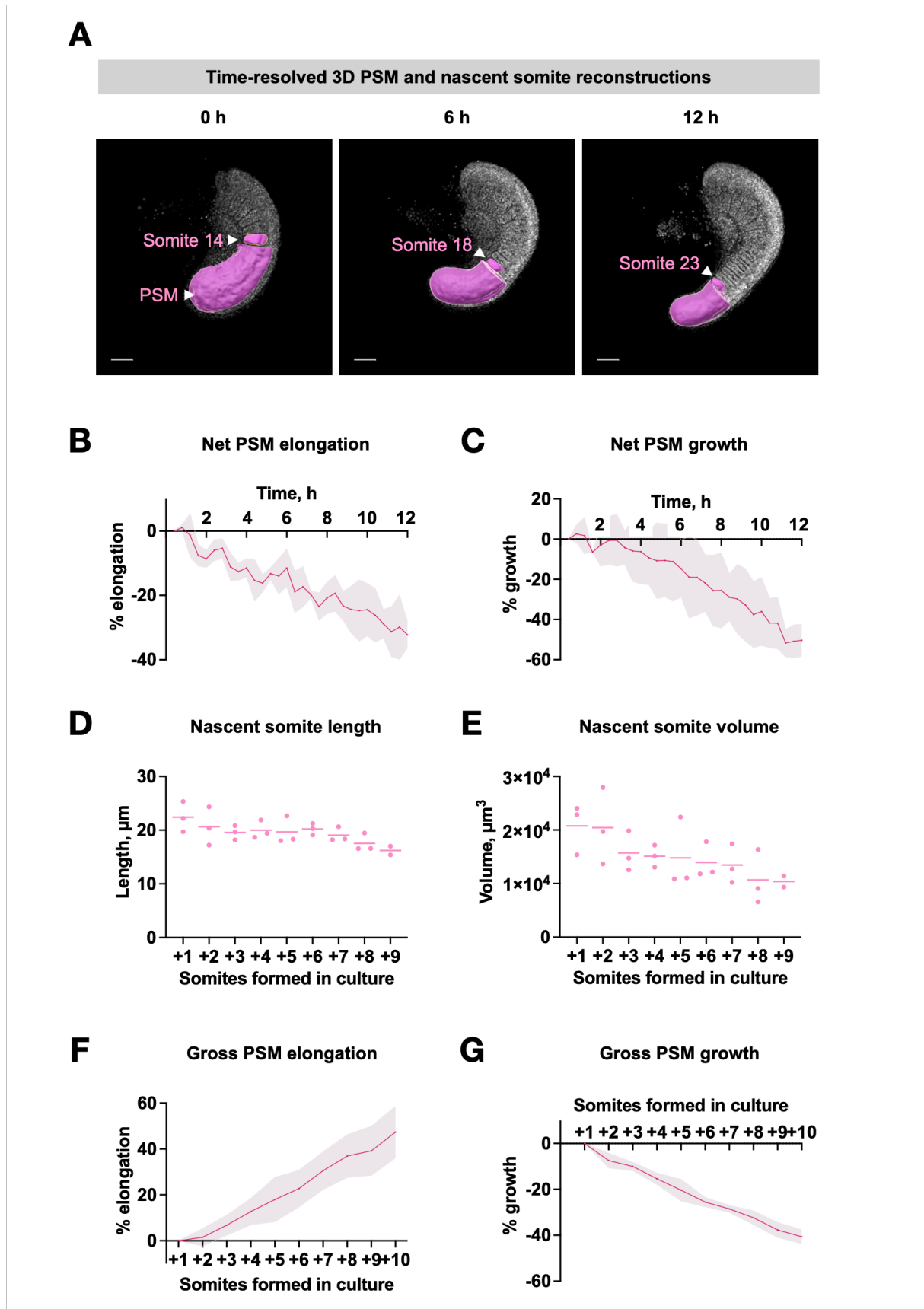


Figure 11. Dynamics of elongation and volumetric growth in the PSM during secondary body formation. (A) 3D surface reconstructions of the PSM and the nascent somite during axis elongation (0 h, 6 h, and 12 h after the onset of imaging), overlaid on the mScarlet-Pcna signal. Scale bars: 50 μm .

(B, C) Net percentage elongation (B) and net percentage volumetric growth (C) in the PSM plotted against time (n = 3, the data is presented as mean \pm SD).

(D, E) Length (D) and volume (E) of each nascent somite formed in culture (n = 3, horizontal lines indicate mean values).

(F, G) Gross percentage elongation (F) and gross percentage volumetric growth (G) of the PSM plotted against somites formed in culture (n = 3, the data is presented as mean \pm SD).

The degree to which volumetric growth accompanies secondary body formation is believed to be influenced by the proliferative activity of cells (which, in turn, is thought to be affected by nutrient availability) [19, 35]. To assess cell proliferation in different tissues of the secondary body, I stained whole wild-type *Cab* embryos with an antibody against Phospho-histone H3 (PH3), a marker for mitotic cells (**Fig. 12A**). Individual tissues were segmented as described before and mitotic activity was quantified as the number of PH3-positive cells per unit volume for each tissue (**Fig. 13B**). This analysis revealed that the neural tube exhibited the highest mitotic activity (151.5 ± 24.59 PH3-positive cells per $1 \times 10^6 \mu\text{m}^3$ (n = 8)), followed by the paraxial mesoderm (105.7 ± 15.66 PH3-positive cells per $1 \times 10^6 \mu\text{m}^3$ (n = 8)), while the notochord displayed significantly lower mitotic activity (8.76 ± 7.78 PH3-positive cells per $1 \times 10^6 \mu\text{m}^3$ (n = 8)) (**Fig. 12C**).

This data, along with tissue-specific morphometric analysis, provides several important insights. First, since no mitotic activity was detected in the notochord, the mechanism driving volumetric growth in this tissue must be cell proliferation-independent (**Fig. 10C,E; Fig. 12B,C**). This aligns with findings in other vertebrate systems, where notochord cells have been observed to expand via vacuolization [57-61]. Second, although cells were observed to undergo mitosis throughout the PSM, the gross volume of this tissue continuously decreased over time (**Fig. 11G; Fig. 12B,C**). This suggests that any volume gained in the PSM through cell proliferation (assuming that cell proliferation is accompanied by cell growth) is offset by the volume lost to other processes, such as increased cell density or cell death. Finally, mitotic activity was present throughout the paraxial mesoderm, which was identified as the primary contributor to the explant's volumetric growth (and, by deduction, to its elongation, **Fig. 10G; Fig. 12B,C**). Therefore, inhibition of cell proliferation could provide an attractive strategy to perturb axis elongation in medaka. This assumption is explored in more detail and serves as the foundation for experiments described in **2.2.2-2.2.4**.

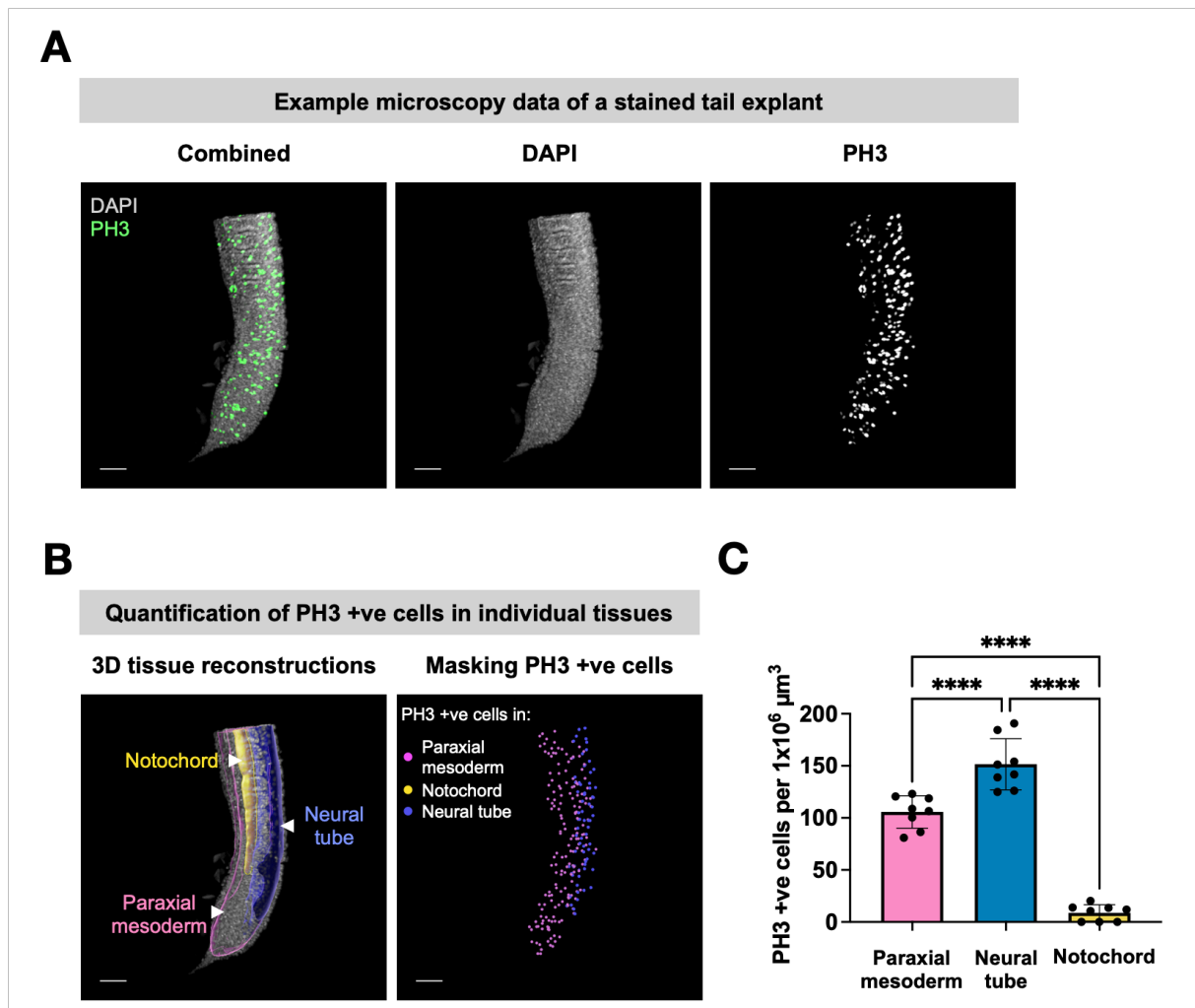


Figure 12. Cell proliferation in distinct secondary body tissues.

(A) Maximum intensity projection of a fixed *Cab* tail, stained with DAPI and anti-PH3 antibody.

(B) Counting of PH3-positive cells in the paraxial mesoderm, neural tube and notochord tissues was performed by creating 3D tissue surface reconstructions and masking the PH3 channel inside each individual tissue. Scale bars: 50 μm .

(C) PH3-positive cells per unit volume in the paraxial mesoderm, neural tube and notochord tissues ($n = 8$, he data is presented as mean \pm SD). Statistical significance was determined by ordinary one-way ANOVA: **** $P < 0.0001$.

2.2 Investigating the integration of axis elongation and somite segmentation

Anteroposterior axis patterning produces a relatively invariant species-specific number of somites. This is striking, given that somites periodically pinch off from the unsegmented PSM that elongates all the while being segmented. Since PSM length is influenced by both axis elongation rate and somite segmentation, it implies a possible integration between these processes to ensure that the PSM is not depleted before the correct somite number is achieved. A previous study from our lab using an *ex vivo* mouse segmentation model demonstrated that the shift in oscillation phase between neighboring PSM cells scales with PSM length, implicating tissue-level oscillatory gene expression dynamics in encoding not only temporal but also spatial information for the patterning process [16]. Building on this discovery, I hypothesized that axis elongation and somite segmentation are linked in the PSM through tissue-level oscillatory gene expression. To test this hypothesis, I perturbed axis elongation through surgical and pharmacological interventions and assessed the somite segmentation response at both the morphological level and the level of underlying oscillatory gene expression dynamics.

2.2.1 Surgical perturbation of axis elongation

Embryonic patterning shows a remarkable capacity to recover from perturbations that occur early in embryonic development. In combination with novel real-time reporters, classical surgical size perturbation experiments provide an exciting opportunity to study if/how the patterning process adjusts to reduced PSM size in real-time *in vivo*. In recent years, several studies have reported successful size reduction in zebrafish embryos by removal of a portion of cells at the blastula stage [5-7]. To replicate this in medaka, I aspirated some cells from the blastoderm of early blastula stage embryos (**Fig. 13A**). To ensure that this procedure did not affect developmental timing, I fixed control and cell removal embryos at different times after cell removal and compared the number of somites formed in each group (**Fig. 13B; Fig. 14**). In all experiments, I observed no significant difference between the average number of somites formed in control and cell removal embryos, with respective groups forming 6.667 ± 0.5164 ($n = 6$) and 6.500 ± 0.5477 ($n = 6$) somites in experiment I, 8.571 ± 0.5345 ($n = 7$) and 8.625 ± 0.5175 ($n = 8$) somites in experiment II, 10.50 ± 0.7071 ($n = 2$)

and 10.29 ± 0.4880 ($n = 7$) somites in experiment III, 17.50 ± 0.5477 ($n = 6$) and 17.20 ± 0.6325 ($n = 9$) somites in experiment IV, 19.25 ± 0.5000 ($n = 4$) and 19.50 ± 0.7071 ($n = 2$) somites in experiment V, 20.00 ± 0.000 ($n = 2$) and 19.50 ± 0.5477 ($n = 6$) somites in experiment VI, 21.75 ± 0.5000 ($n = 4$) and 21.60 ± 0.5477 ($n = 5$) somites in experiment VII, and 22.67 ± 0.5774 ($n = 3$) and 22.11 ± 0.6009 ($n = 9$) somites in experiment VIII (**Fig. 14**). As both control and cell removal embryos consistently formed an equal number of somites in a given period of time, these data suggest that cell removal does not impact the timing of embryonic development in medaka.

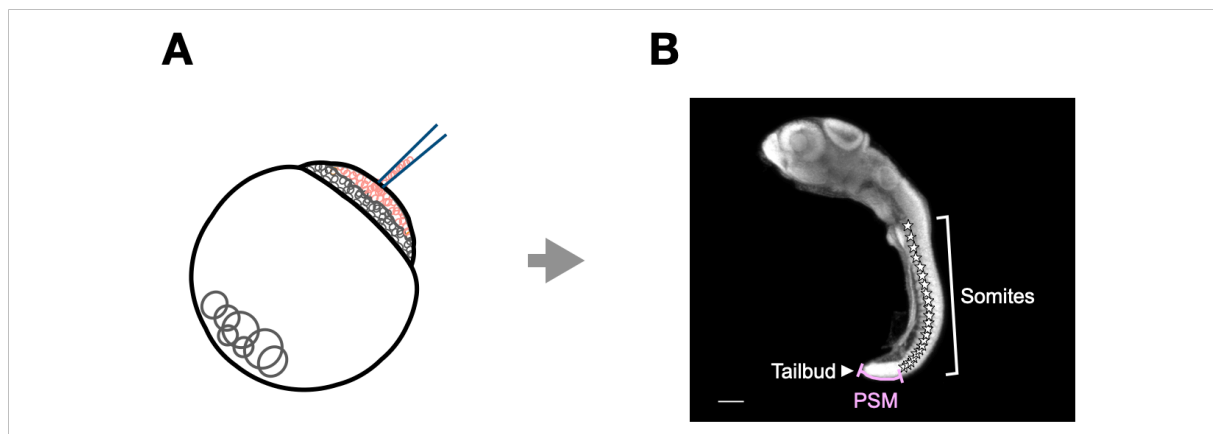


Figure 13. Illustration of the experimental design to size-reduce medaka embryos and measure PSM length.

(A) Cells (in red) were removed from medaka embryos at Iwamatsu stage 10 (early blastula, approximately 1,000 cells) using a glass microneedle. Subsequently, embryos were allowed to develop until the desired stages. (B) A maximum intensity projection of a representative embryo (Iwamatsu stage 26, i.e., 22 somites) stained with DAPI and de-yolked to facilitate flat-mounting. Somites are indicated by white stars. The length of the PSM (i.e., the distance between the anterior end of the PSM and the posterior tip of the tailbud) was measured along the dorsal side of the embryo. Scale bar: 100 μ m.

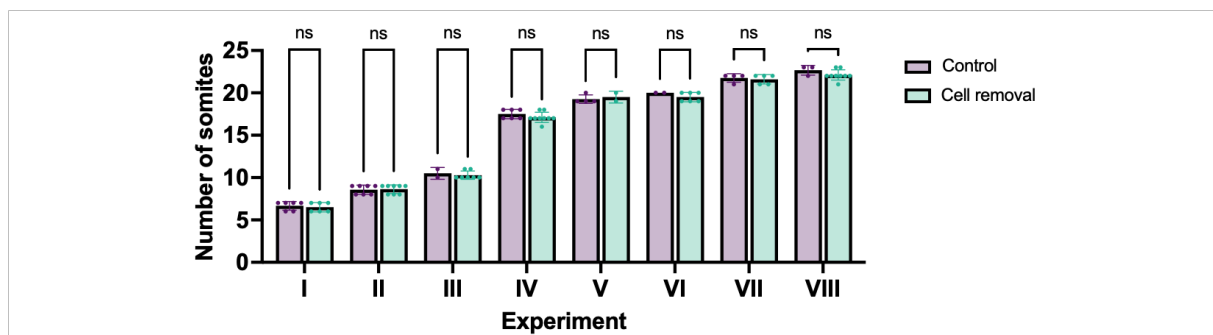


Figure 14. Impact of cell removal on developmental time. The number of somites formed in control and cell removal embryos fixed at various times after the intervention ($n = 6, 7, 2, 6, 4, 2, 4, 3$ control embryos and $n = 6, 8, 7, 9, 2, 6, 5, 9$ cell removal embryos for independent experiments I, II, III, IV, V, VI, VII, VIII, respectively). The data is presented as mean \pm SD. Statistical significance was determined by Šídák's multiple comparisons test: ns, not significant $P > 0.05$.

In the subsequent analysis, I focused on experiments V, VI, VII, and VIII from **Fig. 14**, which from hereafter are referred to as 19 ss, 20 ss, 21 ss, and 22 ss, respectively. I assessed whether cell removal from early medaka embryos affected the length of the PSM at these stages (**Fig. 13B**). The PSM was consistently shorter in cell removal embryos than in control embryos, with a length of $167.5 \mu\text{m} \pm 6.455 \mu\text{m}$ ($n = 4$) in controls and $145.5 \mu\text{m} \pm 4.950 \mu\text{m}$ ($n = 2$) in cell removal embryos at 19 ss, $162.5 \mu\text{m} \pm 3.536 \mu\text{m}$ ($n = 2$) in controls and $147.5 \mu\text{m} \pm 8.479 \mu\text{m}$ ($n = 6$) in cell removal embryos at 20 ss, $146.3 \mu\text{m} \pm 19.38 \mu\text{m}$ ($n = 4$) in controls and $129.8 \mu\text{m} \pm 11.39 \mu\text{m}$ ($n = 5$) in cell removal embryos at 21 ss, and $122.3 \mu\text{m} \pm 17.02 \mu\text{m}$ ($n = 3$) in controls and $102.8 \mu\text{m} \pm 11.81 \mu\text{m}$ ($n = 9$) in cell removal embryos at 22 ss (**Fig. 15A**). These findings demonstrate that surgical size reduction in early medaka embryos leads to a reduction in PSM length. Moreover, they reveal a regulatory response reminiscent of morphallaxis, a phenomenon observed in the vast majority of vertebrate species subjected to size reduction.

Subsequently, I plotted the length of the PSM against the somite stage for control and cell removal embryos, determining the best-fitting linear regression lines (**Fig. 15B**). The PSM length continuously decreased in both control and cell removal embryos, with the regression line for cell removal embryos shifted down on the y -axis. This downward shift was statistically significant, indicating a successful reduction in PSM length due to the perturbation. Notably, the difference in slope values between the fitted linear regression lines for control and cell removal embryos was not statistically significant, indicating that the rate of the net PSM length change was comparable between the two groups.

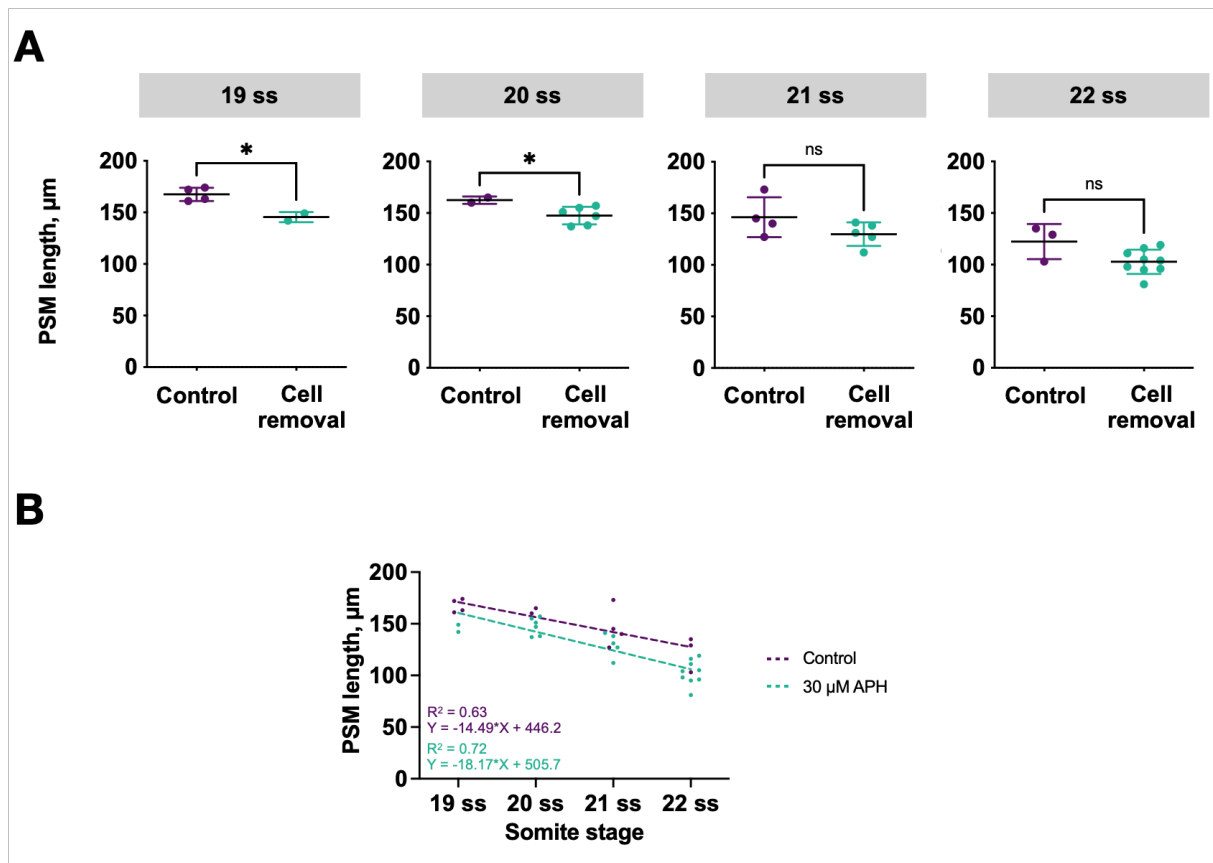


Figure 15. Impact of cell removal on PSM length.

(A) PSM length in control and cell removal embryos measured at 19 ss (n = 4 control embryos and n = 2 cell removal embryos), 20 ss (n = 2 control embryos and n = 6 cell removal embryos), 21 ss (n = 4 control embryos and n = 5 cell removal embryos), and 22 ss (n = 3 control embryos and n = 9 cell removal embryos). The data is presented as mean \pm SD. Statistical significance was determined by unpaired t test with Welch's correction: ns, not significant $P > 0.05$; * $P < 0.05$; ** $P < 0.005$.

(B) PSM length plotted against somite stage in control and cell removal embryos. Dotted lines show the best fit from linear regression. The goodness of fit (R^2) and trendline equations are indicated in the inset. Statistical significance of the difference between y-intercepts was determined by F test: *** $P > 0.05$. Statistical significance of the difference between slopes was determined by F test: ns, not significant $P > 0.05$.

Next, I hypothesized that the size variability observed in the cell removal group could be attributed to the varying number of cells removed from each embryo. To test this hypothesis, I expelled aspirated cells from the microneedle and counted them under the microscope. However, I observed no clear relationship between the number of removed cells and the length of the PSM (**Fig. 16**). Several potential explanations for this observation are discussed in **3.2.1**.

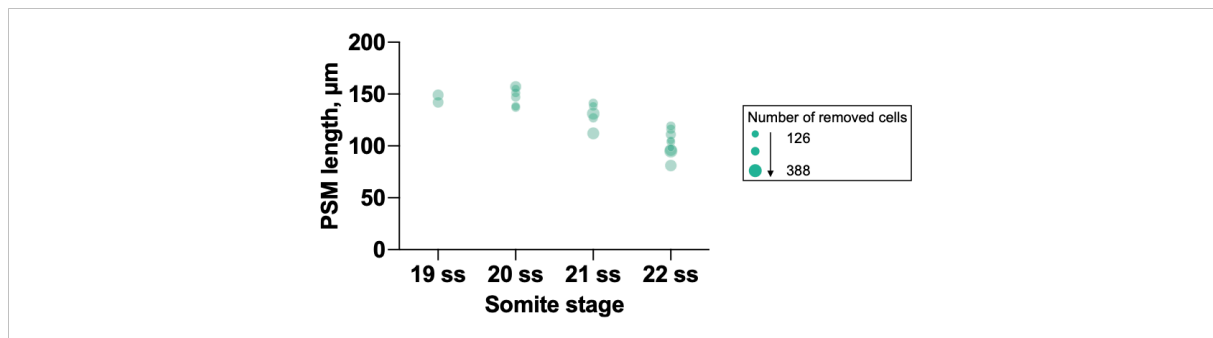


Figure 16. Influence of removed cell number on PSM length. Data from cell removal experiments presented in Fig. 15B. The size of each data point reflects the number of cells removed from the embryo, with larger sizes indicating the removal of more cells and *vice versa*.

The initial motivation for establishing a surgically size-reduced medaka model was to combine it with quantitative analysis of oscillatory gene expression dynamics in the PSM *in vivo*, offering insights into the mechanisms governing the generation of scaled spatial patterns along the anteroposterior axis. While the results presented above indicate that removing cells from early medaka embryos can result in individuals with smaller PSMs, this approach faced several significant limitations, such as poor embryo survival post cell removal and considerable variability in PSM size, which proved challenging to correlate with the number of removed cells. Consequently, an alternative system was explored for a more effective investigation into the intricacies of pattern scaling during embryonic development (refer to 2.2.2).

2.2.2 Pharmacological perturbation of axis elongation

The findings described in 2.1.2 suggest that inhibiting cell proliferation might provide an avenue to perturb axis elongation in medaka. To achieve this, I opted for the use of aphidicolin – a potent inhibitor of polymerases α , δ , and ϵ – known to induce cell arrest in the S-phase of the cell cycle [183]. Due to the challenges associated with imaging live embryos and the limited diffusion of molecules into intact medaka embryos, I conducted this perturbation in tail explants [184]. To assess the effectiveness of aphidicolin in inhibiting cell proliferation in tail explants, I cultured wild-type *Cab* tail explants in a medium containing aphidicolin for 1-4 hours and stained them with an antibody against PH3 (**Fig. 17A**). Utilizing 3D volume reconstructions of whole tail explants, I quantified mitotic activity as the number of PH3-positive cells per unit volume. Compared to control tail explants, aphidicolin-treated tail explants exhibited reduced mitotic activity as early as one hour into treatment, and this

phenotype persisted for at least four hours. These findings affirm that aphidicolin treatment effectively inhibits mitotic activity in tail explants (Fig. 17B).

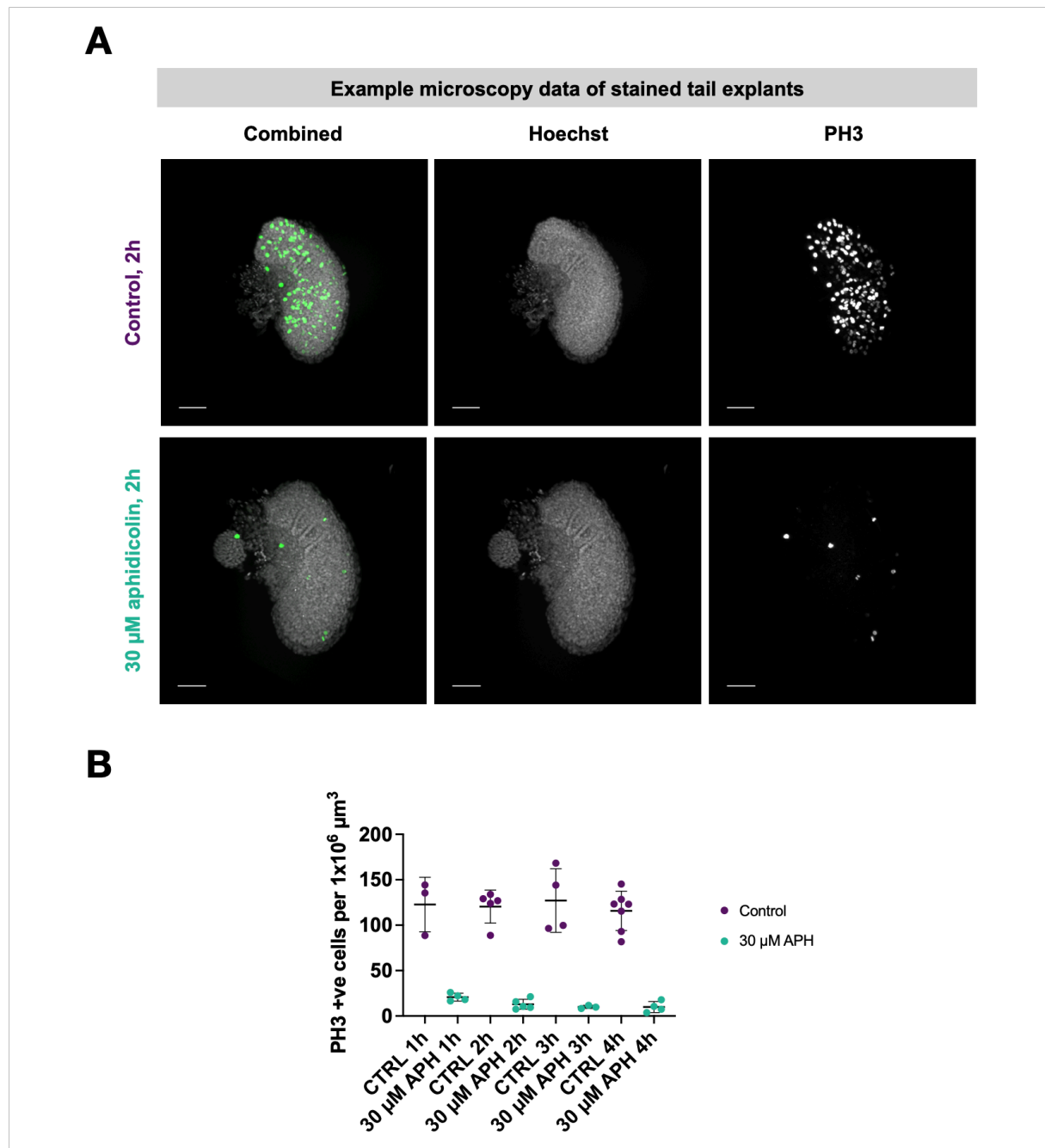


Figure 17. Impact of aphidicolin treatment on cell proliferation in medaka tail explants.

(A) Maximum intensity projections of fixed tail explants stained with Hoechst and anti-PH3 antibody. The top panel shows a representative control tail explant, while the bottom panel shows a representative tail explant treated with 30 μM aphidicolin. Scale bars: 50 μm.

(B) Quantification of PH3-positive cells per unit volume in control and 30 μM aphidicolin-treated tail explants after 1-4 h of treatment (n = 3, 5, 4, 7 control tail explants and n = 4, 5, 3, 4 aphidicolin-treated tail explants after 1 h, 2 h, 3 h, 4 h of treatment, respectively). The data is presented as mean ± SD.

To investigate the effect of reduced mitotic activity on axis elongation, I treated *her7-Venus*^{+/+} tail explants with aphidicolin and imaged them over a ten-hour period (for details about the *her7-Venus* line refer to **2.2.4**). To quantify axis elongation, I used the posterior boundary of the last formed somite at the onset of imaging as the anterior reference point and measured the distance between this point and the tip of the tailbud (**Fig. 18A**). During the initial two and a half hours of imaging (equivalent to three hours of treatment, as imaging was started 30 minutes after the onset of treatment), both control and aphidicolin-treated tail explants elongated in a similar manner, increasing their length by 13.95% (n = 14) and 14.31% (n = 15), respectively. However, between three and six hours of treatment, the aphidicolin-treated tail explants exhibited a pronounced reduction in axis elongation compared to the control group. While the control tail explants elongated by 17.36% in this period of time, the aphidicolin-treated tail explants only elongated by 2.07%. Subsequently, between six and ten hours of treatment, the elongation in the aphidicolin-treated group partially recovered, with control and aphidicolin-treated tail explants elongating by 21.75% and 17.38%, respectively (**Fig. 18B, Table 1**). Taken together, these results indicate a role for mitotic activity in driving axis elongation in medaka. In addition, the observed transient perturbation of axis elongation following aphidicolin treatment suggests that the drug may be depleted or lose its effectiveness over time.

To ensure that aphidicolin treatment did not affect the developmental timing, I counted the number of somites formed in both control and aphidicolin-treated tail explants after ten hours of imaging. The results showed that control tail explants formed an average of 6.50 ± 0.53 somites (n = 10), while aphidicolin-treated tail explants formed an average of 6.46 ± 0.52 somites (n = 11, **Fig. 18C**). This suggests that aphidicolin treatment did not alter the rate of somite formation. Of note, somite boundaries were less well defined in treated tail explants, particularly towards the end of the culture period, making it more challenging to discern them. Together, these findings provide evidence that perturbation of mitotic activity via chronic exposure to aphidicolin can transiently inhibit axis elongation in medaka tail explants without affecting the pace of somite formation.

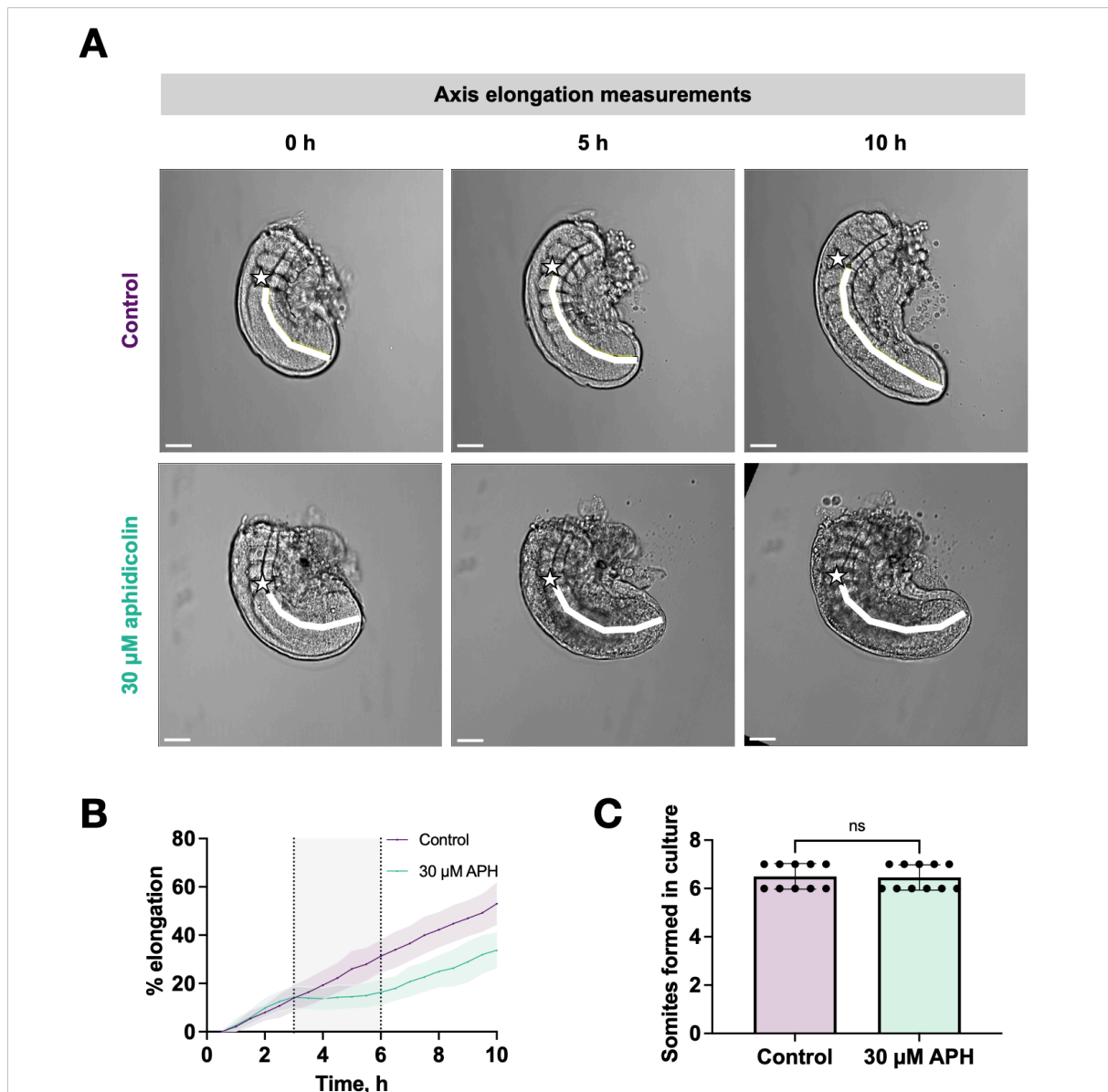


Figure 18. Impact of aphidicolin treatment on axis elongation in medaka tail explants.

(A) Maximum intensity projections of the brightfield channel of representative control (top panel) and 30 μM aphidicolin-treated (bottom panel) tail explants during axis elongation (0 h, 5 h, and 10 h after the onset of imaging). White lines indicate the distance between the reference somite (i.e., the last formed somite at the onset of imaging, marked by white stars) and the tailbud over time. Scale bars: 50 μm .

(B) Percentage elongation of control and 30 μM aphidicolin-treated tail explants plotted against time ($n = 14$ for control tail explants and $n = 15$ for aphidicolin-treated tail explants). The shaded area represents the time period corresponding to 3-6 h after the onset of treatment, during which the most severe axis elongation phenotype was observed.

(C) Number of somites formed after ten hours of culture in control and 30 μM aphidicolin-treated tail explants ($n = 10$ and $n = 11$, respectively). The data is presented as mean \pm SD. Statistical significance was determined by unpaired t test: ns, not significant $P > 0.05$.

Table 1. Percentage elongation of control and aphidicolin-treated tail explants over a ten hour treatment period (derived from Fig. 18B).

Time period	% elongation	
	Control	30 μ M aphidicolin
0.5-3 h	13.95	14.31
3-6 h	17.36	2.07
6-10 h	21.75	17.38
Total	53.06	33.76

2.2.3 Impact of aphidicolin treatment on somite scaling

Based on studies conducted in mice and zebrafish, somite size robustly scales with the length of the PSM throughout ontogeny [5, 10, 16]. To investigate whether medaka embryos possess a similar capacity to scale their morphology, I conducted a comparative analysis of PSM length, nascent somite length, and the ratio between them in control and aphidicolin-treated tail explants (**Fig. 19A**). As expected, PSM length decreased over time in both control and aphidicolin-treated tail explants, with treated PSMs shrinking more rapidly (slope of the best-fit line from linear regression: -5.729 for control tail explants (n = 10) and -14.00 for aphidicolin-treated tail explants (n = 10)), (**Fig. 19B**). This indicated an imbalance between tissue length gained through elongation and tissue length lost through segmentation in aphidicolin-treated tail explants. Consistent with this, somite length did not adjust to the altered axis elongation, as the mean length of the six nascent somites formed in culture remained unaffected by aphidicolin treatment (**Fig. 19C**). Consequently, the mean nascent somite/PSM ratio was disrupted. In control tail explants, this ratio consistently ranged from 0.12 to 0.13 for the six somites formed in culture, indicating that length of the nascent somite constituted 12-13% of the PSM length. In contrast, aphidicolin-treated tail explants showed a progressive increase in the nascent somite-to-PSM ratio with newly forming somites, ranging from 0.12 to 0.16, demonstrating that aphidicolin treatment disrupts scaling (**Fig. 19D**).

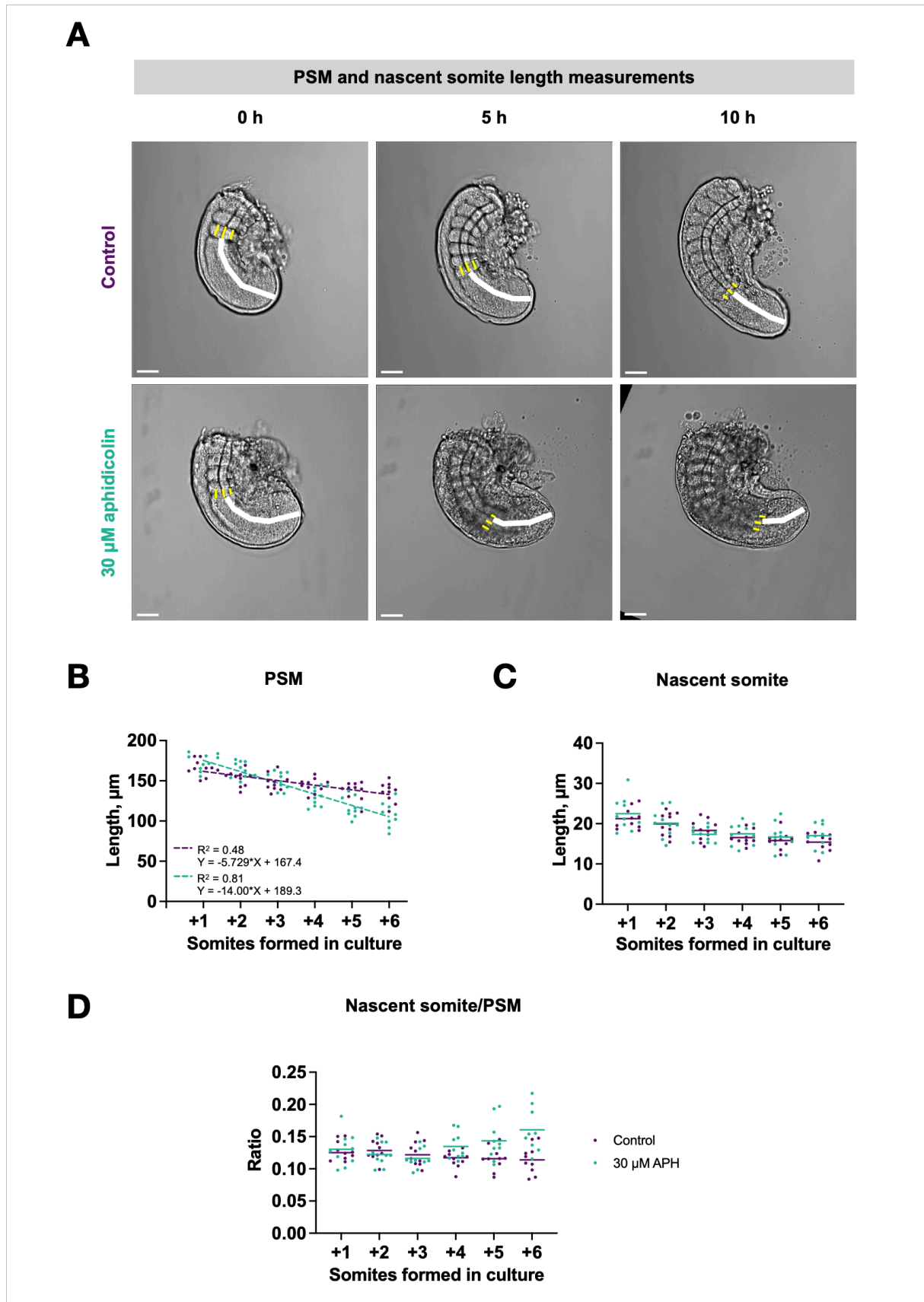


Figure 19. Impact of aphidicolin treatment on pattern scaling.

(A) Maximum intensity projections of the brightfield channel in representative control (top panel) and 30 μM aphidicolin-treated (bottom panel) tail explants during axis elongation (0 h, 5 h, and 10 h after the onset of imaging). White lines indicate the PSM. Three yellow lines mark each nascent somite; nascent somite length was determined by averaging the length of the three lines. Scale bars: 50 μm .

(B-D) PSM length (B), nascent somite length (C) and nascent somite/PSM ratio (D) plotted against somites formed in culture in control and 30 μ M aphidicolin-treated tail explants (n = 10 for both groups). Dotted lines in (B) show the best fit from linear regression, with inset indicating the goodness of fit (R^2) and trendline equations. Statistical significance of the difference between slopes was determined by F test: ****P < 0.0001. Horizontal lines in (C-D) indicate mean values.

The observed absence of somite scaling in response to perturbed axis elongation does not definitively indicate that axis elongation and somite patterning are not integrated. There are several possible explanations for this observation, such as the system not having sufficient time to adapt to the perturbation (refer to **3.2.2** for a more detailed discussion). One approach to test whether this is the case is by extending the imaging period. Alternatively, one can explore indications of scaling at the level of oscillatory gene expression in the PSM, which is hypothesized to integrate axis elongation and somite segmentation and, therefore, is expected to respond to the perturbation faster than somite size. This link is explored below.

2.2.4 Impact of aphidicolin treatment on oscillatory gene expression dynamics

Combined with real-time imaging of segmentation clock reporters, the medaka tail explant system provides an opportunity to observe if and how oscillatory gene expression in the PSM responds to perturbed axis elongation. To this end, I performed aphidicolin treatment in *her7-Venus*^{+/-} tail explants (three still frames from representative control and aphidicolin-treated tail explants are shown in **Fig. 20A**). *Her7-Venus* is an endogenous knock-in reporter line for the expression of the segmentation clock gene *her7*, enabling visualization and quantification of oscillatory gene expression dynamics in the medaka PSM [112]. Consistent with earlier characterizations of Her7-Venus oscillations in medaka, control tail explants exhibited rhythmic waves of Her7-Venus expression originating from the posterior tailbud and arresting at the anterior end of the PSM, predetermining the position of the future somite boundary [112]. Although some aphidicolin-treated tail explants did not exhibit clear traveling waves of Her7-Venus expression, especially towards the end of the imaging period, intensity kymographs revealed that oscillatory gene expression persisted throughout the ten-hour imaging period in both control and aphidicolin-treated tail explants (see representative intensity kymographs in **Fig. 20B**). This data indicates that aphidicolin treatment does not abolish the fundamental oscillatory gene activity in the PSM.

To determine whether aphidicolin treatment impacted the rate of segmentation, I counted the number of full waves present in intensity kymographs derived from control and

aphidicolin-treated tail explants, as shown in **Fig. 20B**. During ten hours of imaging, 7.11 ± 0.33 ($n = 9$) and 6.60 ± 0.55 ($n = 5$) full waves of Her7-Venus expression were found to traverse the PSM in control and aphidicolin-treated tail explants, respectively (**Fig. 20C**). Therefore, although there was no apparent impact on the number of somites formed, aphidicolin treatment seems to slightly decelerate the segmentation clock period (**Fig. 18C**, **Fig. 20C**).

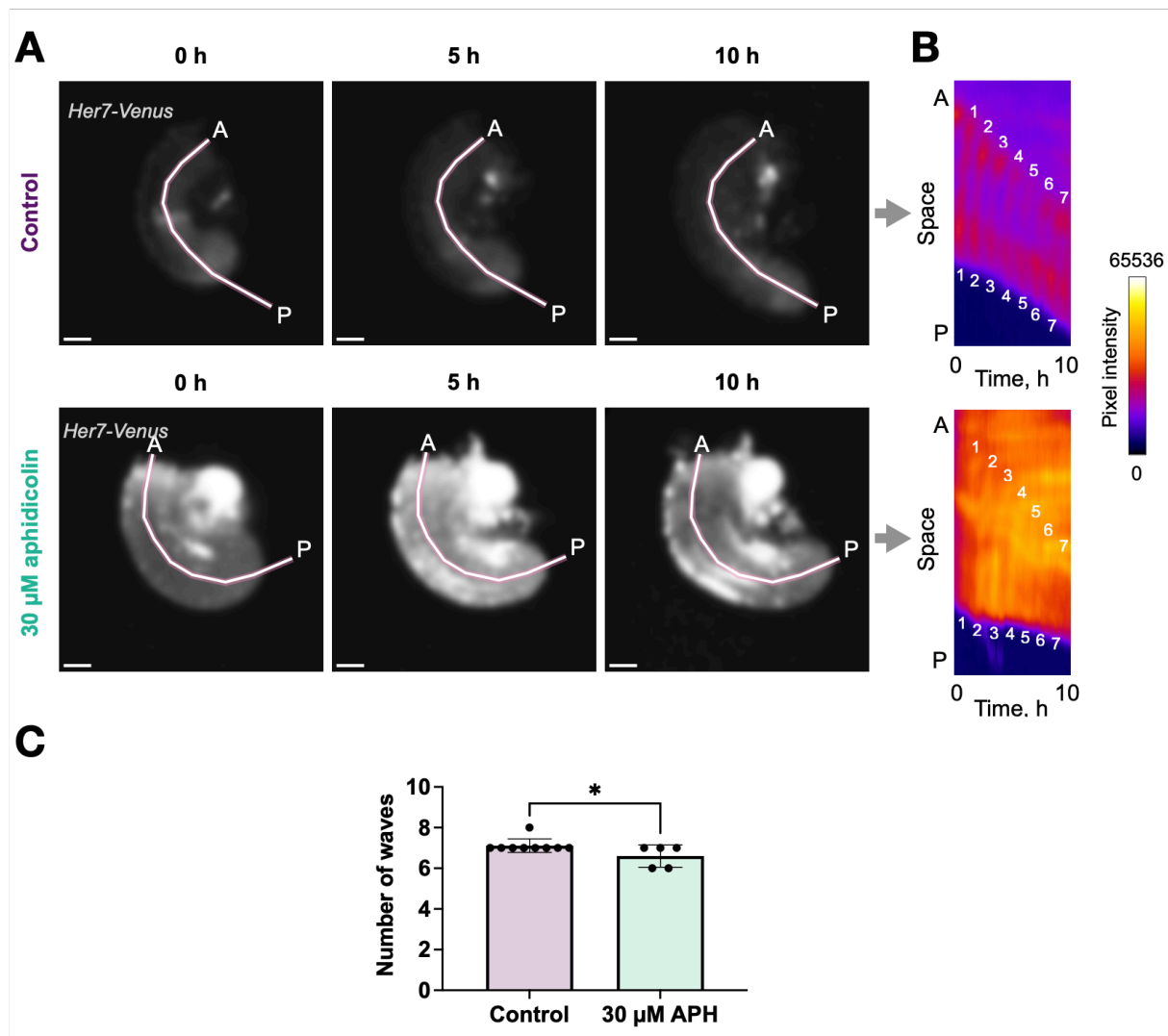
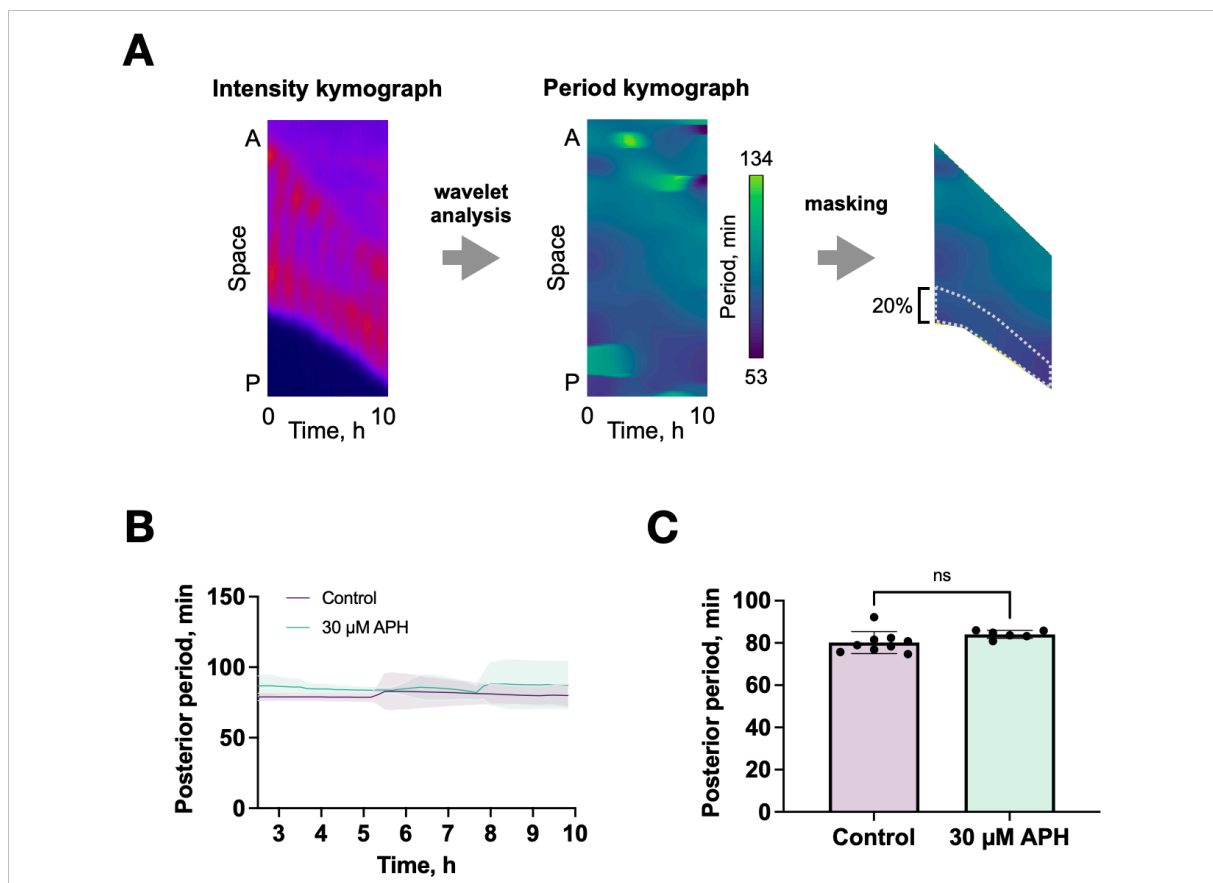


Figure 20. Qualitative examination of Her7-Venus expression dynamics in medaka tail explants. (A) Maximum intensity projections of the blurred Her7-Venus signal in representative control (top panel) and 30 μ M aphidicolin-treated (bottom panel) tail explants during axis elongation (0 h, 5 h, and 10 h after the onset of imaging). The increased Her7-Venus signal intensity in aphidicolin-treated tail explants may be attributed to drug autofluorescence of the drug, as these samples also exhibited increased background autofluorescence (data not shown). Scale bars: 50 μ m.

(B) Intensity kymographs derived from the representative time-series data in (A). These kymographs were generated by drawing a line across the tail explant (as indicated by white lines in (A)) and extracting pixel intensities along this line for each time point. Each complete wave of Her7-Venus expression is numbered at its initiation and termination points. A – anterior; P – posterior.

(C) The number of complete waves observed in intensity kymographs generated from control and 30 μM aphidicolin-treated tail explants ($n = 9$ and $n = 5$, respectively). The data is presented as mean \pm SD. Statistical significance was determined by unpaired t test: * $P < 0.05$.

To quantify the segmentation clock period, I applied wavelet analysis on the intensity kymographs, using the open-source tool pyBOAT that was developed in our lab (Fig. 21A) [185]. This analysis revealed that the posterior period was stable over the course of ten hours in both control and aphidicolin-treated tail explants, with an average posterior oscillation period of 80.17 ± 1.74 minutes ($n = 9$) in controls and 84.07 ± 0.78 minutes ($n = 5$) in aphidicolin-treated tail explants (Fig. 21B,C). While the difference in these periods lacks statistical significance, the data aligns with the wave number calculation in Fig. 20C, indicating a potential rise in the posterior oscillation period in aphidicolin-treated tail explants.



posterior. The data is presented as mean \pm SD. Statistical significance was determined by unpaired t test: ns, not significant $P > 0.05$.

Previous studies in several vertebrate species have established that the oscillation period is graded along the PSM, with posterior cells oscillating faster [16, 97, 107-113]. The gradual slowing of oscillations as a function of distance along the PSM introduces a slight phase-shift between adjacent PSM cells, creating a phase gradient along the tissue [16, 65, 97, 112, 114, 115]. A previous study from our lab using medaka embryos grown at 27°C demonstrated that the period of Her7-Venus oscillations slows down from approximately 80 minutes in the posterior to about 100 minutes in the anterior PSM, with the resulting phase gradient spanning 4.69 radians [112]. To test whether axis elongation phenotype ensuing from aphidicolin treatment affects the behavior of Her7-Venus oscillations in space, I quantified Her7-Venus period and phase gradients along the PSM in control and aphidicolin-treated tail explants. To this end, I generated period and phase wavelet movies by applying wavelet analysis on every pixel in the time-series dataset, using the open-source tool Spatial pyBOAT (SpyBOAT) [185] (**Fig. 22**). I copy pasted ROIs delineating the PSM from brightfield movies (as shown in **Fig. 19A**) into the resulting wavelet movies (as shown in **Fig. 22B**) and extracted period and phase values along the tissue at subsequent somite formation cycles.

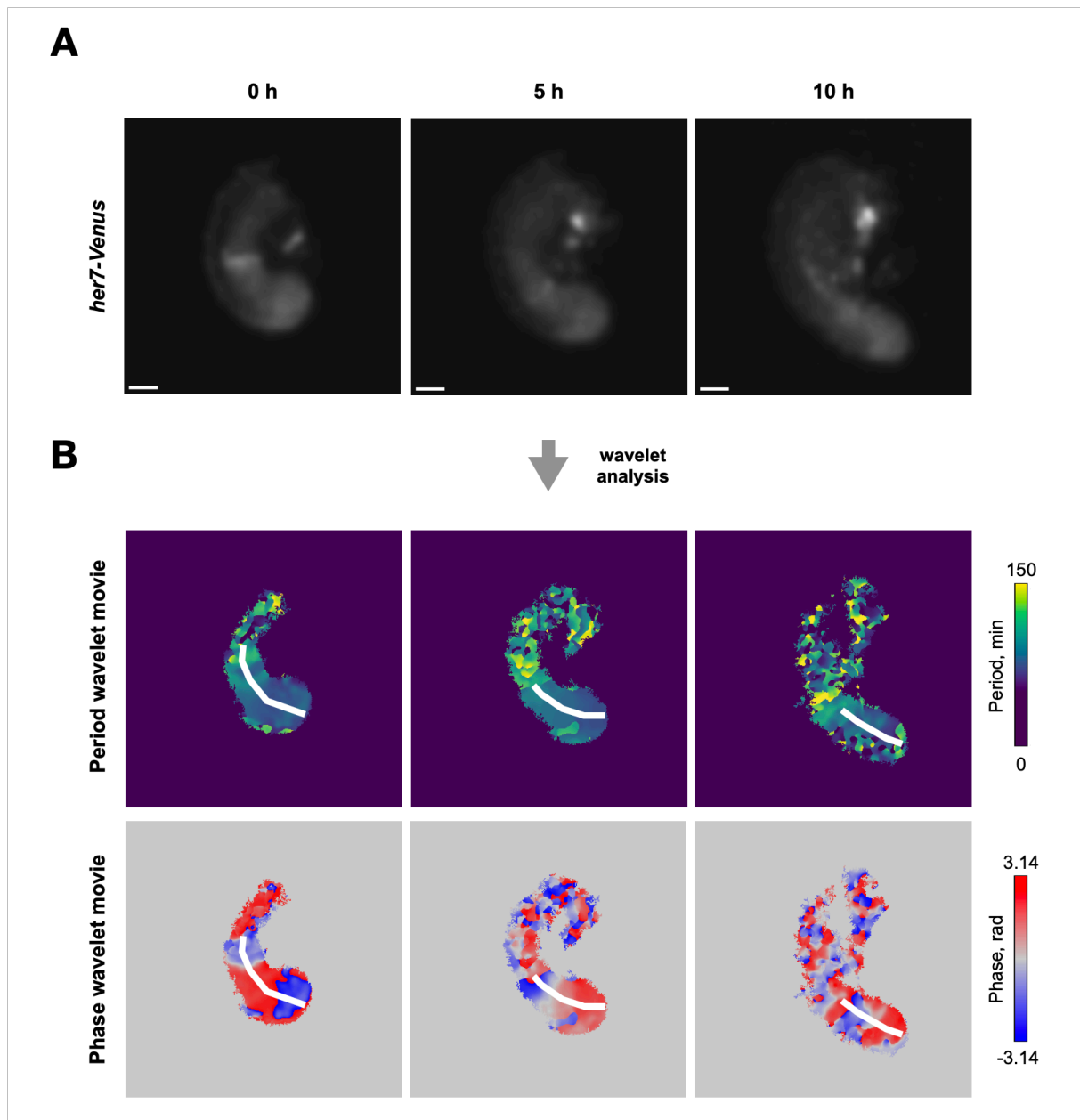


Figure 22. Her7-Venus period and phase gradient extraction in medaka tail explants.

(A) Maximum intensity projections of the blurred Her7-Venus signal in a representative control tail explant during axis elongation (0 h, 5 h, and 10 h after the onset of imaging). Scale bars: 50 μ m.

(B) Corresponding period (top panel) and phase (bottom panel) wavelet movies, generated by applying wavelet analysis on each pixel in the time-series. Period and phase values are extracted along the white lines demarcating the PSM length. The resulting measurements are plotted in **Fig. 23** and **Fig. 24** and further detailed in **Appendices A** and **B**.

When plotted against absolute distance, measurements extracted from period wavelet movies revealed a clear Her7-Venus period gradient in the PSM for both control and aphidicolin-treated tail explants. Specifically, cells in the posterior PSM exhibited faster oscillations than those in the anterior PSM (**Fig. 23A**). Notably, the entire period gradient was shifted upwards in aphidicolin-treated tail explants, indicating that aphidicolin treatment led to an increased Her7-Venus oscillation period not only in the posterior-most PSM but across

the full length of the tissue. The slope of the period gradient in aphidicolin-treated tail explants appeared to steepen compared to controls during successive somite formation cycles, as demonstrated by the increasing ratio of a values obtained from the best-fitting linear regression lines for aphidicolin-treated and control tail explants (**Fig. 23C**). Interestingly, when the period gradient was plotted against normalized distance, the difference in the steepness of the period gradient between aphidicolin-treated and control tail explants lessened (**Fig. 23B,C**). Indeed, the ratio of their respective a values hovered close to one for the majority of somite formation cycles (**Fig. 23C**). This finding suggests that the absolute time by which Her7-Venus oscillations decelerate between the posterior and anterior PSM is comparable in both aphidicolin-treated and control tail explants. The persistence of a relatively constant absolute period gradient amplitude in aphidicolin-treated tail explants, even with an increased oscillation period throughout the PSM, suggests that this aspect of the period gradient may play a functional role in anteroposterior axis patterning.

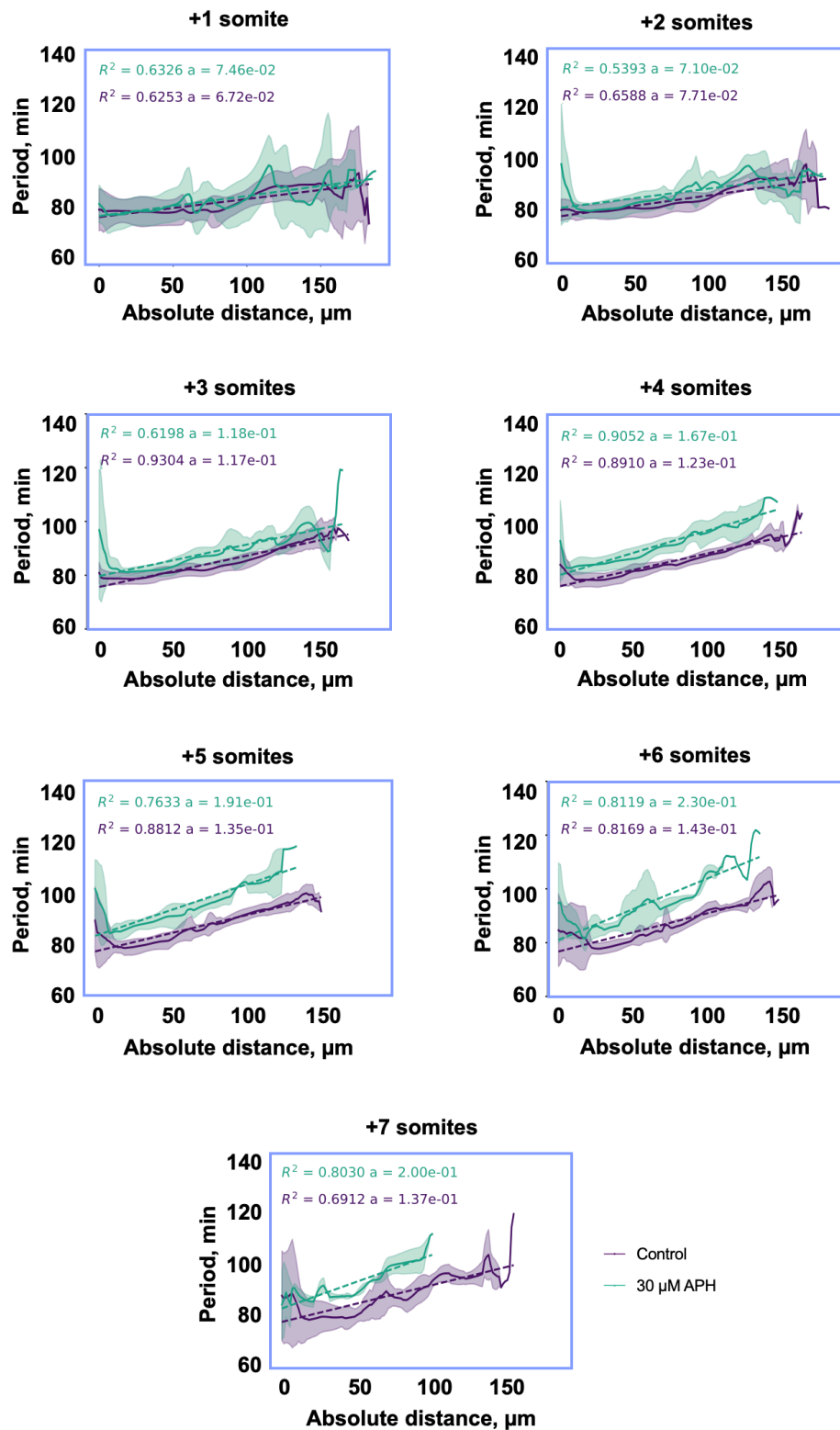
A

Figure 23 (continued on the next page).

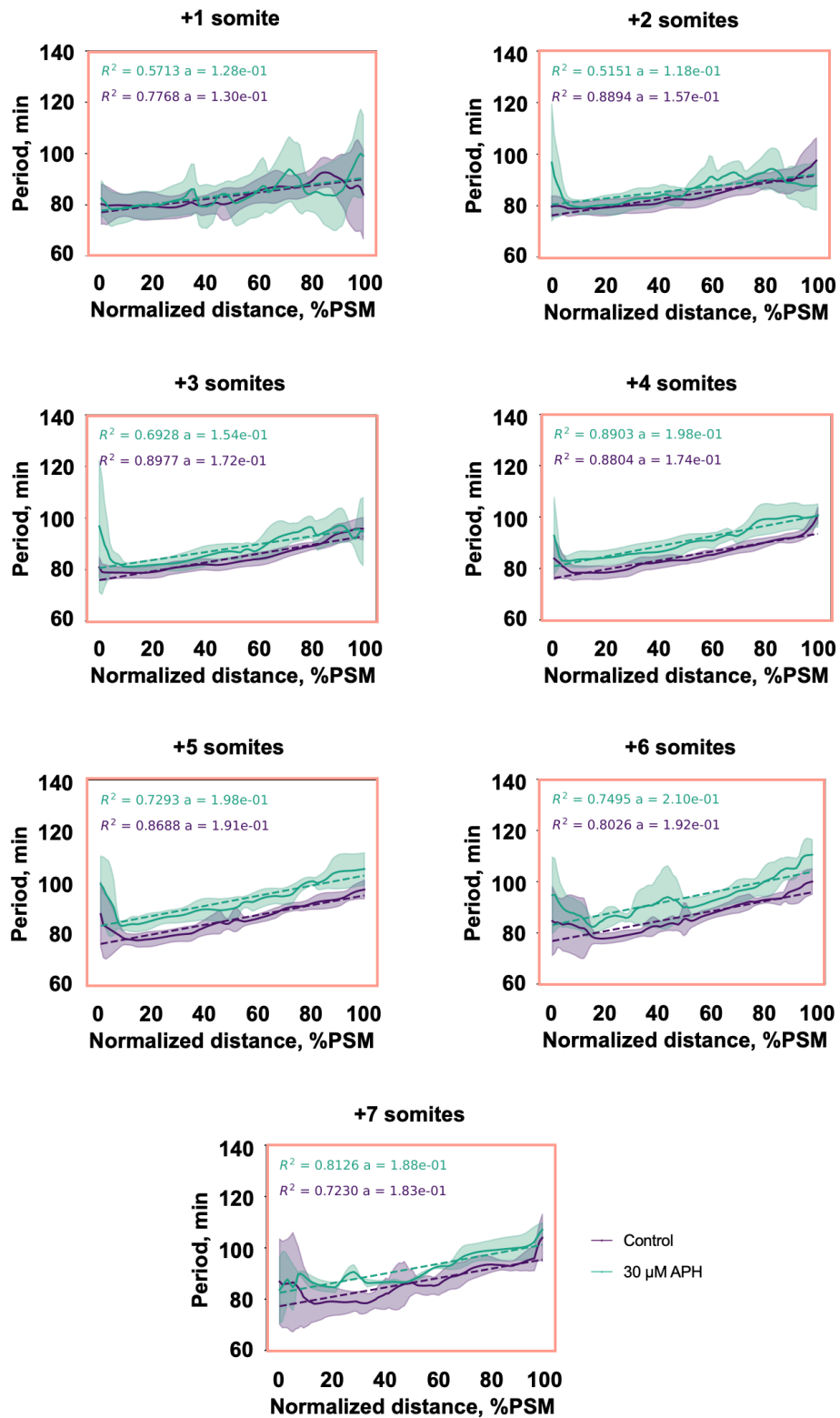
B

Figure 23 (continued on the next page).

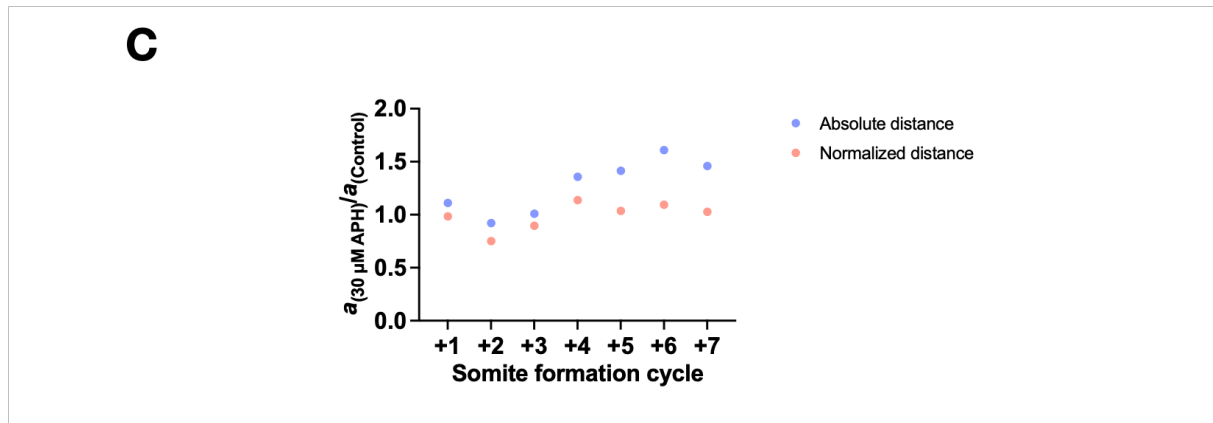


Figure 23. Impact of aphidicolin treatment on Her7-Venus period gradient in medaka tail explants.

(A, B) Period measurements for control and 30 μM aphidicolin-treated tail explants ($n = 9$ and $n = 5$, respectively) plotted against absolute distance (A) or normalized distance (B) during successive somite formation cycles (from +1 to +7). The posterior end of the PSM is set to 0. The data is presented as mean \pm SD. Dotted lines show the best fit from linear regression ($y = ax + b$). The goodness of fit (R^2) and a values are indicated in the inset.

(C) $a_{(30 \mu\text{M APH})}/a_{(\text{Control})}$ ratio plotted against somite formation cycle, using a values obtained from the best-fitting linear regression lines representing the period gradient.

Subsequently, I examined the phase gradient in control and aphidicolin-treated tail explants. Phase measurements, when plotted against absolute distance, revealed that samples with shorter PSMs exhibited a slightly steeper phase gradient than those with longer PSMs. This effect became more pronounced over time as the length difference increased between PSMs in control and aphidicolin-treated tail explants (Fig. 24A). Excitingly, the fact that the phase gradient adjusted its slope in shorter PSMs, rather than maintaining the same slope while ‘cropping’ the absolute phase span, indicated that the phase gradient may scale with the PSM length.

Of note, β values extracted from the best-fitting exponential functions, representing the rate of phase delay across space, tended to be lower in aphidicolin-treated tail explants compared to controls at corresponding somite formation cycles (Fig. 24A). This was unexpected, as the opposite outcome would be anticipated in a scenario where scaling occurs. It seems that higher β values were extracted for control tail explants when their phase gradients were actually shallower due to the shape of the gradient, specifically the dip at the posterior PSM. In the future, this could be addressed by constraining the A value, thereby imposing all differences on β .

When plotted against normalized PSM length, phase gradients of control and aphidicolin-treated tail explants displayed a substantial overlap during equivalent somite formation cycles, providing additional evidence for a scaling relationship between the phase

gradient and the length of the PSM (**Fig. 25B**). To compress a normal amplitude of phases within the reduced space, the relative phase-shift between neighboring PSM cells must have been increased in aphidicolin-treated tail explants (rather than decreased, as indicated by β values). Together, these observations suggest that the relative phase-shift between cells is regulated to match the spatial context, such that a fixed phase gradient amplitude is achieved regardless of variations in PSM length.

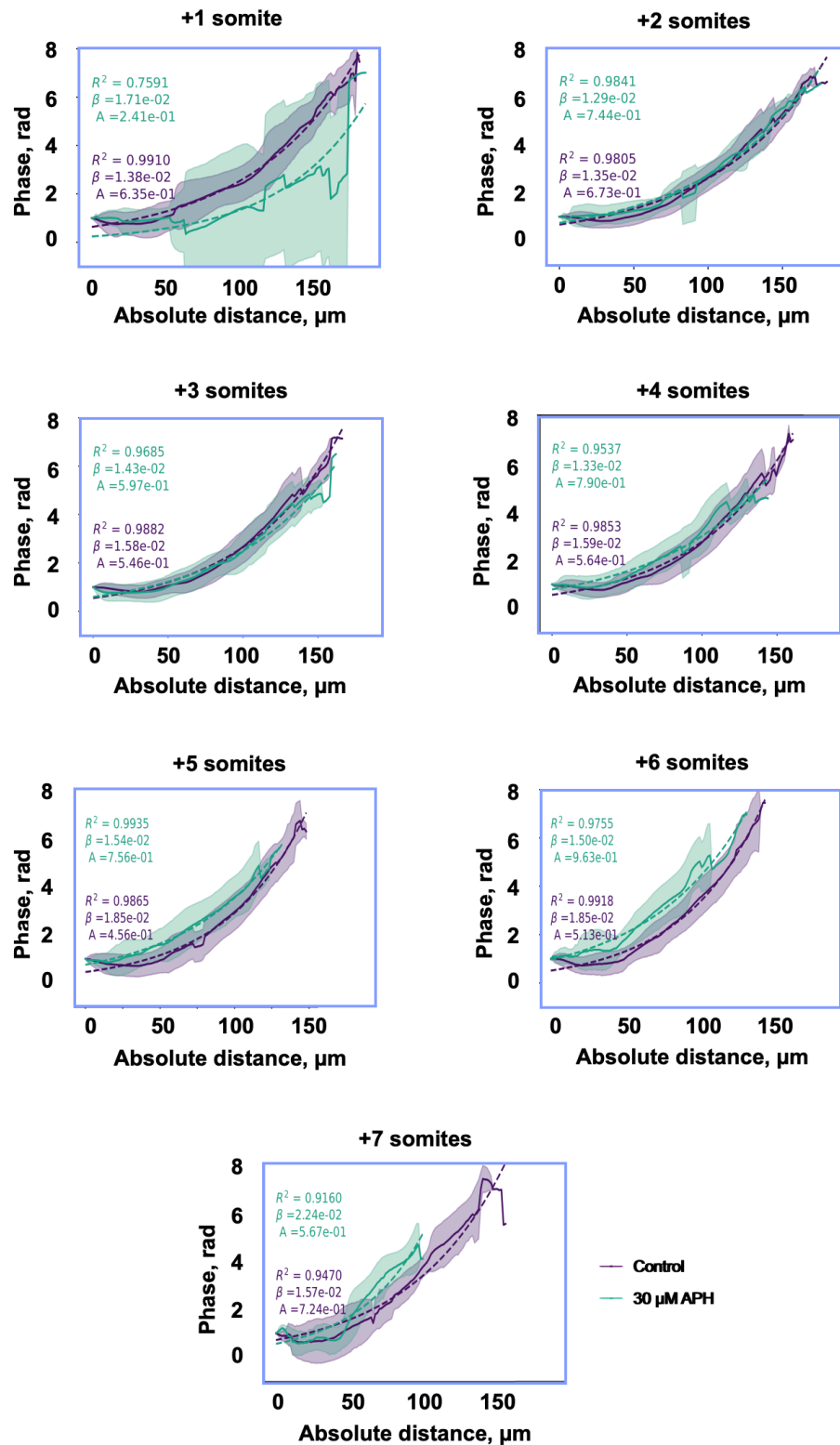
A

Figure 24 (continued on the next page).

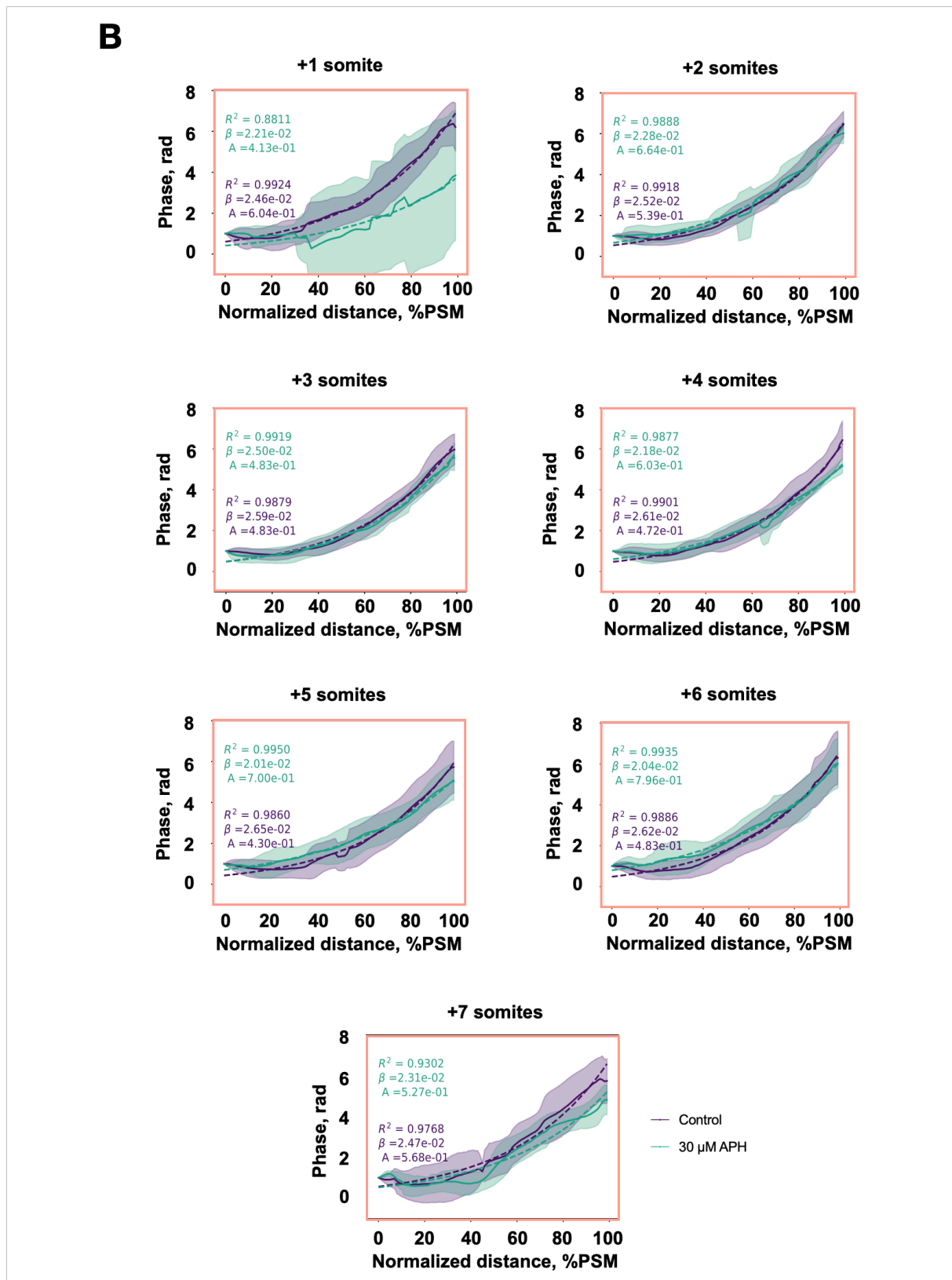


Figure 24. Impact of aphidicolin treatment on Her7-Venus phase gradient in medaka tail explants.

(A, B) Phase measurements for control and 30 μM aphidicolin-treated tail explants ($n = 9$ and $n = 5$, respectively) plotted against absolute distance (A) or normalized distance (B) during successive somite formation cycles (from +1 to +7). The posterior end of the PSM is set to 0. The data is presented as mean \pm SD. Dotted lines show the best fit from exponential function ($y = Ae^{\beta x}$). The goodness of fit (R^2), A , and β values are indicated in the inset.

3 Discussion

3.1 Axis elongation during secondary body formation in medaka

3.1.1 Axis elongation is accompanied by volumetric growth

In this study, I observed a 26.70% increase in the volume of the elongating secondary body in medaka tail explants over a developmental period corresponding to nine somite formation cycles (from 12-14 ss to 21-23 ss). Interestingly, zebrafish embryos elongate their secondary body with little volumetric growth during comparable developmental stages [35]. In this regard, medaka embryos show more similarities to amniotes such as mice and chicks, where volumetric growth plays an important role in axis elongation during secondary body formation [35, 39]. Below, I discuss the potential factors contributing to these species-specific differences in volumetric growth in the broader context of vertebrate development.

3.1.1.1 Linking volumetric growth and nutritional environment

Axis elongation involves cell rearrangement- and volumetric growth-based cell behaviors. While cell rearrangement-based mechanisms play a conserved role in driving axis elongation during both primary and secondary body formation, the extent to which volumetric growth contributes to the elongation of the secondary body differs significantly among different vertebrate species. As volumetric growth depends on the synthesis of biomaterials, these differences have been proposed to stem from differential constraints imposed on embryos by the unique nutritional environments in which they develop [19, 35]. This hypothesis has been supported by several studies showing that embryos equipped with a large yolk (e.g., dogfish and chick) or nourished through a placenta (e.g., mouse) undergo significantly more volumetric growth than those that have limited yolk reserves (e.g., lamprey and zebrafish) [35, 39].

In the light of this hypothesis, the discrepancy between the degree of volumetric growth in medaka and zebrafish raises the question as to how their nutritional environments compare to each other. Both medaka and zebrafish embryos are laid externally and thus rely on a finite supply of nutrients deposited in the yolk sac by the mother to complete their

morphogenesis and transition to exogenous feeding. In addition, periods of endogenous and exogenous feeding overlap in both species, enabling them to prevent or postpone starvation in food-deprived environments [174, 186]. Despite these shared characteristics, several lines of evidence suggest that medaka fish may experience a more favorable nutritional environment compared to zebrafish during early developmental stages. First, medaka embryos have a higher yolk-to-embryo ratio, implying that they are equipped with a greater reserve of nutrients [168, 175]. Second, sensory, motor, and digestive functions appear to be more developed in medaka than in zebrafish at the time of hatching [169-174, 176]. Therefore, while medaka larvae can start foraging for exogenous food soon after hatching, zebrafish larvae must first complete morphogenesis by expending resources in the remaining yolk. As a result, the period between the initiation of exogenous feeding and the complete absorption of the yolk sac appears to be longer in medaka, potentially making them less prone to starvation and providing an opportunity for volumetric growth.

To sum up, maternal nutrient provisioning could explain the observed variation in the extent to which volumetric growth contributes to secondary body formation in medaka and zebrafish, aligning with the existing literature on the subject. However, more research into the early nutritional requirements of medaka and zebrafish is needed. Importantly, we lack a precise understanding of how the specific yolk components and their concentrations compare in these two species [187-189]. Additionally, it is important to consider that the volumetric growth data for zebrafish was derived from intact embryos nourished by the yolk, while the corresponding data for medaka was obtained from tail explants separated from the yolk and grown in a culture medium supplemented with critical nutrients, such as glucose and glutamine. How the composition of the culture medium compares to the natural yolk composition in medaka and how differences in nutrient availability impact volumetric growth remains unclear, further complicating the interpretation of findings within this thesis.

3.1.1.2 Linking volumetric growth and embryonic development rate

Despite the fundamental preservation of the general sequence of developmental events, the rate of embryonic development varies from one species to another. This variability is particularly evident in the segmentation clock, which exhibits species-specific periodicity in vertebrate embryos. Given that tissue rearrangements and volumetric growth actualize axis elongation at distinct timescales, it is reasonable to expect that slower developmental rates

may create more opportunities for volumetric growth through mechanisms like cell division, cell growth, or extracellular matrix deposition in the pericellular space. Indeed, the period of the segmentation clock generally exhibits a positive correlation with volumetric growth. However, the relationship between developmental rate and volumetric growth is not that straightforward. Taking cell proliferation as an example, the likelihood of proliferation is not solely determined by the developmental rate. It is also influenced by the cell cycle length, which may or may not scale proportionally with the rate of development. Therefore, when examining the connection between developmental rate and volumetric growth, it is crucial to consider additional variables, such as cell cycle length.

In mice, where the segmentation clock has a period of 2 hours and the PSM cell cycle lasts approximately 14 hours, around 0.143 cell divisions occur per somite formation cycle [190, 191]. In chick embryos, with a segmentation clock period of 1.5 hours and a paraxial mesoderm cell cycle lasting 9-11 hours, cells divide around 0.136-0.167 times per somite formation cycle [107, 192]. Zebrafish embryos have an indirectly measured PSM cell cycle length of approximately 5.5 hours, although this is likely an underestimate, given that similar indirect measurements in other vertebrate species tended to be shorter than corresponding direct cell cycle measurements [107]. Consequently, with a segmentation clock period of 0.5 hours, zebrafish PSM cells undergo at most 0.09 cell divisions per somite formation cycle. While it is important to acknowledge that values for cell cycle length may vary between studies, the segmentation clock in zebrafish appears to run faster relative to the cell cycle compared to mice and chicks, providing fewer opportunities for volumetric growth. This aligns with observed differences in the extent of volumetric growth during secondary body formation in these species.

As the length of the cell cycle in the medaka PSM is yet to be determined, additional research is required to elucidate how the findings presented in this thesis align with our current understanding of the interplay between embryonic development rate and volumetric growth. Nevertheless, drawing from the observed volumetric growth during secondary body formation in medaka, one could hypothesize that medaka embryos undergo a greater number of cell divisions per somite cycle compared to zebrafish but fewer than mouse and chick embryos.

3.1.2 PSM elongation is associated with a decrease in volume

Over the course of somitogenesis, the evolution of PSM length is shaped by two processes – tissue segmentation and tissue elongation – that have an opposing effect on its length. As length lost to segmentation may exceed that gained by elongation, direct measurements of net PSM length can obscure the full extent of gross elongation happening in the tissue or give a false impression that the tissue does not elongate at all. The results presented in this thesis using an indirect approach to assess gross elongation in the PSM showed that the medaka PSM did indeed undergo elongation during secondary body formation, even though a continuous decrease in its net length was observed over time.

Interestingly, my results showed that elongation in the medaka PSM was not accompanied by volumetric growth. On the contrary, a consistent reduction in PSM volume, both in net and gross terms, was observed over time. This indicates that volumetric growth observed in the paraxial mesoderm tissue during secondary body formation occurs in the segmented somites, rather than in the PSM.

Surprisingly, the gross volume in the medaka PSM decreased despite the presence of mitotic cells in the tissue. Intriguingly, mitosis in the PSM appears to be a conserved feature of vertebrate development, regardless of differences in the extent of volumetric growth observed in embryos of different species [35, 39]. While it is conceivable that species-specific differences in the proportion of mitotic cells and/or the length of the cell cycle might dictate how much volumetric growth is possible in the tissue, stage-matched data required for a systematic comparison of these parameters and the evaluation of their contribution to volumetric growth across species is currently lacking. That said, while species-specific differences related to the cell cycle may explain differences in the amount of volume gained by the tissue, they alone cannot account for the observed loss of volume in the medaka PSM. To counterbalance the volume gained through mitotic activity and accommodate volumetric shrinkage, additional mechanisms must be involved.

In line with the findings reported in this thesis, a recent study by Thomson et al. observed that the zebrafish PSM elongated despite the observed net decrease in its length and that this elongation was also accompanied by reduction in PSM volume [182]. In the zebrafish system, the volumetric shrinkage was linked to an increase in cell density and a

decrease in the volume of individual cells over time. While this raises the possibility of an analogous mechanism taking place in the medaka PSM, the extent of its conservation among vertebrates remains uncertain. For example, cell density, while graded along the tissue, appears to be regionally conserved across developmental stages in the quail PSM [39]. Another plausible mechanism that could lead to a gross reduction in PSM volume is the predominance of cell death over cell proliferation in the PSM. Indeed, cell death is known to gradually outweigh mitosis towards the end of somitogenesis in the chick PSM [193]. Together, these studies demonstrate that rather than relying solely on cell proliferation, axis elongation involves multiple intricate processes in the PSM that can vary among different vertebrates. To discern which mechanisms are important for axis elongation in medaka, further experiments are required.

3.1.3 Paraxial mesoderm is the main contributor to overall volumetric growth in the tail explant

The relative contribution of different cell behaviors to anteroposterior axis elongation varies not only in a developmental stage- and species-specific manner, but also in a tissue-specific manner. In this study, I provided the first tissue-level characterization of elongation and volumetric growth dynamics during secondary body formation in medaka. Notably, I found that the paraxial mesoderm accounted for approximately 60% of the tail explant volume. However, it is plausible that this value may overstate the actual paraxial mesoderm volume, as certain components of the non-paraxial mesoderm, such as intermediate and lateral plate mesoderm cells or extracellular matrix, might have been misclassified as paraxial mesoderm during segmentation. To address this, future research would benefit from obtaining reporter lines for paraxial mesoderm-specific genes, such as *mesogenin 1*, to aid in delineating this tissue with greater precision and improving overall segmentation accuracy.

Regardless of this potential overestimation, the substantial difference in the relative size of the paraxial mesoderm compared to the neural tube and notochord (approximately 20% and 5% of the total explant volume, respectively) highlights the paraxial mesoderm as the primary contributor to absolute volumetric growth in medaka tail explants. This finding aligns with observations in quail embryos, where the paraxial mesoderm exhibits the largest relative participation in the overall volume increase along the axis [39]. In contrast, during late stages of secondary body formation in zebrafish embryos, volumetric growth is primarily

generated by the neural tube and notochord, while the paraxial mesoderm does not contribute additional volume to the elongating axis [35]. While the potential impact of nutrient accessibility and developmental rate on volumetric growth in the paraxial mesoderm remains unexplored, it is clear that, in this context, medaka exhibits more similarities to amniotes than its teleost relative, the zebrafish.

3.2 Integration of axis elongation and somite segmentation

3.2.1 Dissecting the regulative response to experimental size reduction in medaka embryos

Experimental size reduction has long served as a valuable tool for investigating the regulative mechanisms governing robust embryonic patterning. In this study, surgical removal of cells from early medaka embryos resulted in individuals with smaller PSMs at somite stages 19-22. Importantly, the length of the PSM decreased at a similar rate in control and cell removal embryos, suggesting an absence of a compensatory growth mechanism to counterbalance the loss of cellular material during these stages. Additionally, despite size reduction, no apparent developmental delay was observed in cell removal embryos during the period spanning somite stages 6-22. This observation suggests that medaka embryos do not rely on specific size checkpoints to progress from one developmental stage to the next. Taken together, these observations align with the morphallactic response observed in size-reduced zebrafish and *Xenopus* embryos, indicating that medaka embryos may employ a similar regulative strategy for the robust establishment of their body plans.

Despite this, the observed discrepancy between the number of cells removed and the subsequent reduction in PSM length suggests that medaka embryos may also engage in a form of epimorphosis, similar to the response seen in mouse embryos. Specifically, the removal of a substantial percentage of cellular material (10-40% of total cellular content, assuming that embryos contained approximately 1,000 cells when subjected to the cell removal procedure) resulted in a relatively moderate decrease in PSM length. One possible explanation for this discrepancy lies in the confinement of the evaluation of PSM length to late somitogenesis stages, as this constraint may have hindered the study's ability to detect compensatory growth that potentially took place during earlier embryonic stages. To conclusively determine the presence or absence of compensatory growth in medaka, a more comprehensive analysis that encompasses earlier embryonic stages is necessary. As compensatory growth in mouse embryos is characterized by an accelerated rate of cell proliferation and an increased proportion of proliferating cells, investigating alterations in the cell cycle following cell removal in medaka embryos could provide valuable initial insights into the occurrence of compensatory growth (or lack thereof) in this model organism [8].

Other than compensatory growth, the mismatch between the severity of the experimental procedure and the resulting moderate phenotype can also be attributed to certain limitations inherent to the experimental design. In this study, I used the length of the PSM as a proxy for overall embryo size, thereby assuming the preservation of a constant size relationship (i.e., isometric scaling) between the PSM and the entire body size in differently sized embryos. However, this size relationship has not been empirically defined in medaka or any other vertebrate system. Notably, studies in *Drosophila* have demonstrated varying scaling properties among different internal organs in response to changes in whole body size. For example, the heart exhibits strong isometric scaling with embryo length, the hindgut shows isometric scaling in the face of large-scale perturbations of size, but not within the limits of natural size variation, while the ventral nerve cord displays weak scaling behavior in both contexts [194]. On top of that, different scaling relationships can be generated between the same two traits in differently sized *Drosophila* embryos depending on which of the three environmental factors – nutrition, temperature, or rearing density – is manipulated to generate variation in body size [195]. Together, these findings underscore the complexity of relating a single trait to overall body size and raise uncertainties about the PSM length accurately representing the true size of medaka embryos. To address this, direct measurements of whole body size are essential, although this is difficult to achieve in medaka embryos due to their curved geometry.

In addition, cell removal may have anisotropically affected PSM size, resulting in a more significant reduction along axes other than the anteroposterior. To ascertain whether or not this is the case in medaka, PSM measurements should include also the dorsoventral and mediolateral axes.

Another factor that may contribute to the observed discrepancy is the uncertainty regarding the relative amount of cells removed from individual embryos. This uncertainty arises from the difficulty in distinguishing medaka embryos at morula stages (i.e., 256-512 cells) and blastula stages (i.e., 1,000 cells), compounded by their rapid progression from one developmental stage to another. Consequently, there is a possibility that a smaller or larger portion of cells was removed from certain embryos than initially assumed. Importantly, this ambiguity also has the potential to explain the absence of a clear relationship between the number of removed cells and the length of the PSM across samples. To gain better understanding of the impact of cell removal on embryo size, future experiments should focus

on quantifying the volume of removed cellular material, rather than relying solely on the absolute cell count.

While this project established the groundwork for future exploration into the regulative responses triggered by size reduction in medaka embryos, these limitations highlight the complexity of interpreting the consequences of early cell removal, emphasizing the need for further investigations to refine our understanding of the regulatory mechanisms governing robust embryonic patterning across embryos of varying sizes.

3.2.2 Dissecting the lack of somite scaling in aphidicolin-treated tail explants

Vertebrate embryos robustly pattern their anteroposterior axis with a species-specific number of somites. The existing body of research in mouse and zebrafish embryos indicates that somite length exhibits robust scaling with the PSM throughout ontogeny in both normal and size-reduced systems, making sure that the PSM is not depleted before a complete set of somites is formed [5, 10, 16]. Interestingly, in the present study, I observed an accelerated reduction in the length of the PSM in aphidicolin-treated tail explants compared to controls, as evidenced by a significantly steeper negative slope in the aphidicolin condition. Indeed, within the observed timeframe, nascent somite length did not appear to adjust to the aphidicolin-induced perturbation of axis elongation, suggesting a lack of scaling. That said, it is important to note that measurements of nascent somite length exhibited substantial variability among individual samples in both the aphidicolin-treated and control tail explant groups. Moreover, the boundaries of nascent somites became progressively more challenging to discern in aphidicolin-treated tail explants, potentially introducing a source of error in the measurements.

The failure of aphidicolin-treated tail explants to adjust somite length in response to perturbed axis elongation can be interpreted in several ways. First, it may indicate a potential lack of integration between axis elongation and somite patterning. If this scenario holds true, and considering the persistent elongation phenotype, the net change in PSM length would be expected to maintain a steeper slope in aphidicolin-treated tail explants than in controls throughout somitogenesis, resulting in the production of only a fraction of normal-sized somites by the end of this process. In contrast to prevailing literature, this would imply robust regulation of somite size rather than somite number. Second, insufficient time for the system

to adapt to the perturbation could be a contributing factor. In this scenario, the scale with which somites are set up would eventually adjust to the altered axis elongation, leading to a shallower slope in the change in net PSM length, akin to control embryos. To distinguish between these scenarios, extending the imaging duration to observe whether scaling is restored when the system is given more time is essential. Unfortunately, the culture conditions were not optimized for longer imaging at the time of this study, with the viability of control tail explants beginning to deteriorate after approximately ten hours of culture. Recently, Iris Markja has improved the experimental setup for medaka tail culture, doubling the imaging duration to 20 hours, providing a promising avenue for further exploration (Master thesis). Excitingly, her results showed a significant reduction in nascent somite length in aphidicolin-treated tail explants after only four somite formation cycles, suggesting that medaka embryos possess the capacity to scale their morphology.

3.2.3 Period and phase gradients respond to aphidicolin treatment

While the role of oscillatory gene expression in regulating the temporal periodicity of somite segmentation is clear, recent evidence from *ex vivo* studies suggests its involvement in regulating the spatial periodicity as well. Specifically, the gradual change in period along the PSM results in the accumulation of a relative phase-shift between neighboring cells, which is believed to encode positional information for somite segmentation.

The wavelet analysis presented in this thesis demonstrated an increase in the Her7-Venus oscillation period across the length of the PSM in aphidicolin-treated tail explants, resulting in an upward shift in the period gradient. The maintenance of the period gradient despite the perturbation implies a functional importance of the deceleration of oscillations along the PSM, aligning with findings in other systems. For instance, the period gradient was observed to emerge *de novo* in dissociated and re-aggregated mouse PSM cells, even when exclusively using posterior PSM cells with closely matched periods [109]. In addition, the absolute period gradient amplitude was reported to be temperature-invariant in medaka [112].

In this study, the characterization of the phase gradient in control and aphidicolin-treated tail explants revealed a possible scaling relationship between the phase gradient and the length of the PSM. Specifically, aphidicolin-treated tail explants with shorter PSMs exhibited a steeper phase gradient, indicating an increased relative phase-shift between

neighboring cells. Consequently, despite the shorter PSM lengths in aphidicolin-treated tail explants, both control and aphidicolin-treated tail explants accommodated a similar phase gradient amplitude in their PSMs. Building upon insights from prior studies in our lab, the adaptive nature of the phase gradient suggests that oscillatory gene expression may integrate both temporal and spatial information for the robust patterning of the anteroposterior axis, challenging the conventional clock-and-wavefront model [16, 112, 147].

3.2.3.1 Does relative phase-shift encoding underlie somite scaling in medaka?

In the presented data, changes in the phase gradient slope in response to aphidicolin treatment manifested gradually over time, becoming noticeable by the formation of the fourth somite in culture. Interestingly, no evident somite scaling was observed over the six somite formation cycles in culture, as discussed in **3.2.2**. Assuming the validity of this observation and ruling out errors in somite measurements attributed to the challenge of visualizing somite boundaries in aphidicolin-treated tail explants, it is important to note that some delay between the response in the phase gradient and that in somite size is expected, as adjustments in the former should precede those in the latter. To determine whether the phase gradient indeed underlies the somite scaling mechanism in the medaka PSM, further investigation requires an extension of the imaging duration using the improved medaka tail culture protocol (refer to **3.2.2**).

3.2.3.2 Relative phase-shift encoding as a general mechanism for robust anteroposterior axis patterning

Research in our lab suggests that relative phase-shift encoding may provide phenotypic robustness to anteroposterior axis patterning, not only in response to size variation but also under different temperature conditions. Specifically, Lauschke et al. demonstrated a consistent maintenance of a 2π phase-shift between central and peripheral mouse mPSM cells at both 33°C and 37°C [16]. In addition, experiments in medaka tail explants revealed that while the period of oscillatory gene expression in the PSM is highly temperature-dependent, the phase dynamics, as well as somite size, remain unchanged when embryos are grown within a broader temperature range between 22° and 32°C [112]. Unlike mouse embryos, which generally develop at approximately 37°C due to their internal mode of development, medaka embryos are laid externally and encounter a wide range of constantly changing

temperatures in the wild, depending on the season and the time of day. Therefore, relative phase-shift encoding, in addition to providing phenotypic robustness in the face of size variations, may also indicate an ancestral mechanism behind temperature-invariant anteroposterior axis patterning.

3.2.3.3 Candidate reference oscillators in the medaka PSM

According to the model by Goodwin and Cohen, the encoding of spatial information through relative phase-shift requires a second, reference oscillator in the system [63]. Notably, a study in mice, utilizing dynamic Notch and Wnt signaling reporters, provided empirical evidence that changing the phase-shift between Notch and Wnt signaling pathways – resulting in out-of-phase oscillations in the posterior and in-phase oscillations in the anterior – is essential for proper segmentation of the tissue [147].

Currently, there is no evidence of oscillatory activity in the Wnt signaling pathway in medaka. Nevertheless, *in situ* hybridization studies have identified two additional oscillating genes downstream of the Notch signaling pathway, namely *her1/11* and *her5*, exhibiting traveling wave patterns in the PSM. Intriguingly, double fluorescent *in situ* hybridization images revealed that while *her1/11* and *her5* expression overlapped in the posterior PSM, in some instances, only *her5* was expressed in the anterior stripe domain, indicating a possible change in the phase-shift between these genes as a function of space [78]. In addition, *her12* and *hey1* transcripts were found to oscillate in the posterior and intermediate PSM, respectively [77, 78].

In fact, the list of genes showing oscillatory expression patterns in the medaka PSM is likely more extensive. Analysis of posterior PSM transcriptomes collected at different points in the somite formation cycle in mouse, chick, and zebrafish embryos identified 56, 182, and 24 highly robust candidate oscillating genes in each respective species, mainly associated with Notch, FGF, and Wnt signaling pathways [84]. While the oscillatory expression of the vast majority of these genes has not yet been confirmed through *in situ* hybridization or real-time imaging studies, these findings suggest that an oscillating gene network is an evolutionarily conserved feature of the segmentation clock, shared between amniotes and anamniotes. Therefore, obtaining similar genome-wide data for medaka embryos may further expand the list of genes likely to function as a reference oscillator.

3.3 Outlook

In this thesis, I focused on investigating pattern scaling in medaka through surgical size reduction in whole embryos and aphidicolin treatment in the tail explant system. Moving forward, it is essential to refine these size reduction techniques further.

A key aspect is gaining a deeper understanding of the relationship between the timing and severity of surgical cell removal and resulting embryo size. This refinement is essential for achieving more reliable and pronounced size phenotypes, which, in turn, would enable us to explore how somite size and Her7-Venus dynamics adapt to alterations in body size within an *in vivo* context. Additionally, it would be interesting to explore the possibility of increasing embryo size in medaka, as has been reported in goldfish after the fusion of two eggs in the 4-cell stage [2].

Regarding the tail explant system, the optimization of culture conditions to enhance the viability of tail explants has already been achieved in the lab. With this improved protocol, the next step will be to repeat aphidicolin treatment in *her7-Venus^{+/-}* tail explants to observe whether and how somite length and Her7-Venus dynamics adjust to reduced PSM length given sufficient time after the perturbation.

Another exciting avenue for future research is exploring potential differences in regulative capacity during primary and secondary body formation in medaka. Evidence from *Xenopus* suggests that surgically size-reduced embryos progressively normalize the scale with which somites are set up, such that posterior somites recover normal size [196]. Excitingly, aphidicolin wash-out experiments in the tail explant culture offer an opportunity to investigate whether medaka can regulate its size back towards normal during secondary body formation once the inhibition of mitosis is lifted.

Finally, recent research from our lab using an *in vitro* mouse system has shown that FGF signaling operates upstream of the clock, influencing the oscillation phase-shift in the PSM [155]. As FGF signaling also plays a conserved role in guiding cell behaviors essential for axis elongation, it could potentially serve as a node for integrating axis elongation and somite segmentation, ensuring the formation of an accurate number of scaled somites. Complementing measurements of Her7-Venus oscillations with those of FGF activity using

the *snai1a-Venus* reporter line available in our lab would allow us to examine the interplay between FGF signaling, Her7-Venus oscillations, and axis elongation simultaneously.

In summary, the ongoing optimization of techniques and the exploration of dynamic signaling responses to size alterations, combined with the investigation of the role of FGF signaling in linking axis elongation and somite segmentation, will collectively contribute to forming a more complete and nuanced understanding of pattern scaling in medaka. Furthermore, relating these findings to other model organisms will help establish the generality of these principles in vertebrate development.

4 Materials and methods

4.1 Fish husbandry

Inbred medaka (*Oryzias latipes*) animals of the *Cab* strain were kept as closed stocks in a fish facility at EMBL. Adult fish were maintained at 27°C under a 14 hour light/10 hour dark cycle. The following transgenic lines were used in this study:

Line	Reporter type	Source
<i>mScarlet-pcna</i>	Endogenous knock-in	Generated by Ali Seleit
<i>Tg(brachyury:Venus)</i>	Transgenic	Purchased from NBRP Medaka, #TG1003
<i>her7-Venus</i>	Endogenous knock-in	Generated by Carina Vibe

4.2 General embryo handling

Embryos were grown in 1X embryo rearing medium (ERM) at 27°C until desired stages. Any eggs stuck together via their long attachment filaments were separated by grasping and tangling attachment filaments with two forceps, until individual embryos were released from the cluster. Embryos were staged according to Iwamatsu [157].

4.2.1 Dechoriation with hatching enzyme

In experiments involving whole embryos, embryos were dechorionated with a hatching enzyme (purchased from the NBRP). To improve the penetration of the hatching enzyme, the short villi that cover the embryonic chorion were removed by gently rolling embryos (not more than ten at a time) on a sandpaper (p2000 grit size, waterproof). Next, embryos were lined along the edge of an empty glass dish tilted at a 45° angle, which reduced the amount of hatching enzyme needed to fully cover the embryos. Embryos were submerged in the hatching enzyme and incubated at 27°C from 30 minutes to 2 hours until the chorion disintegrated (time varied depending on the batch and on whether the hatching enzyme was fresh or re-used). Dechorionated embryos were carefully transferred to a glass dish filled with sterile 1X ERM supplemented with 1% Penicillin-Streptomycin (Sigma, P4333) and washed a

couple of times to remove any residual hatching enzyme. The remaining hatching enzyme was saved for re-use.

Due to their fragility, dechorionated embryos were handled with extra care. They were kept in glass dishes and moved from one dish to another with a wide-mouthed glass transfer pipette. Care was taken to not expose them to air in between transfers and washes.

4.2.2 Manual dechoronation and dissection of tail explants

In experiments involving tail explants, embryos were dechorionated manually using two pairs of fine forceps (Dumont, 11252-20). First, embryos were moved to a 10 cm plastic petri-dish filled with sterile CO₂-independent medium (Gibco, 18045054), supplemented with 0.1% BSA (Equitech-Bio, BAC62), 1% Penicillin-Streptomycin (Sigma, P4333) and 2 mM L-Glutamine (Gibco, 25030). One pair of forceps was used to puncture and grasp the chorion, while the second pair was used to gently peel off the chorion piece by piece, starting at the puncture site. While puncturing, care was taken not to extend the forceps too far through the chorion in order to avoid damaging the embryo. At Iwamatus stage 23 (12-14 ss), yolk sacks of dechorionated embryos were torn open and deflated using forceps, so that embryos could be laid flat on the dish. With the lateral side of the embryo facing the bottom of the dish, the posterior tail was cut off by using a scalpel to first separate the tail from the surrounding yolk tissue, and then to make another cut along the dorsoventral axis 2-5 somites above the PSM. Dissected tails were washed in a 3.5 cm petri dish filled with fresh culture medium.

4.3 Morphometric analysis

4.3.1 Whole-mount antibody staining

Cab embryos at Iwamatsu stage 23 (12 ss) were fixed in 4% paraformaldehyde (Electron Microscopy Sciences, 15710) in 2X PTw overnight at 4°C. After fixation, embryos were washed in PTw. Next, embryos were dehydrated in 100% methanol and stored for four days at -20°C. Then, embryos were rehydrated in gradually decreasing concentrations of methanol in PTw (75%, 50% and 25%, 5 minutes each), followed by 3 x 10 minutes washes in PTw. Antibody staining was performed as previously described [197]. Primary rabbit monoclonal anti-PH3 antibody (Cell signaling technology, #3642) was used at a 1:200

dilution from the stock solution. Secondary donkey anti-rabbit Alexa Fluor 488 antibody (Thermo Fisher, A32790) was used at a 1:1000 dilution from the stock solution. DAPI (Merck, 10236276001) was used at a 1:500 dilution from the 10 mg/ml stock solution.

4.3.2 Mounting and imaging

Live imaging. Wells of an 8-well glass bottom dish were filled with 400 μ l culture medium pre-heated to 27°C. Double positive tail explants from the cross of *mScarlet-pcna*^{+/-} males and *Tg(brachyury:Venus)*^{+/-} females were collected in up to 2 μ l volume and transferred to separate wells of an 8-well glass bottom dish. Tail explants were directed towards the center of the well with a P2 filter tip. The dish containing tail explants was then transferred to the Zeiss LSM 780 laser-scanning microscope with a preheated incubation chamber set to 27°C. Tail explants were left undisturbed for 15 minutes to allow them to equilibrate to the correct temperature and to settle at the bottom of the well. Tail explants were imaged with the following settings:

	Venus imaging	mScarlet imaging
Objective lens	Plan-Apochromat 20x/0.8	
Zoom	0.8x	
Dimensions	512 x 512 pixels, 38-42 slices, 16-bit	
xy resolution	1.038 μ m/pixel	
z interval	2.5 μ m	
Pixel dwell	6.27 μ sec	
Averaging	Line, 4	
Pinhole	90 μ m	
Imaging interval	25 min	
Imaging duration	12.5 h	
Excitation	514 nm (25 mW Argon laser)	561 nm (20 mW DPSS laser)
Laser power	0.5-0.8%	1.5%
Emission detection	518-578 nm	578-712 nm

Imaging of stained embryos. Embryos stained for PH3 and DAPI were cleared in 50% glycerol (Merck, 1370282500) in PTw for 1 hour at 4°C, followed by an overnight incubation in 100% glycerol at 4°C. Embryos were de-yolked and flat mounted in 100% glycerol. Embryos were imaged on the Zeiss LSM 780 laser-scanning microscope with the following settings:

	DAPI imaging	Alexa 488 imaging
Objective lens	Plan-Apochromat 20x/0.8	
Zoom	0.7x	
Dimensions	512 x 512 pixels, 68-102 slices, 8-bit	
xy resolution	1.19 $\mu\text{m}/\text{pixel}$	
z interval	1 μm	
Pixel dwell	1.58 μsec	
Averaging	1	
Pinhole	90 μm	
Excitation	405 nm (30 mW Diode laser)	488 nm (2 mW Helium-neon laser)
Laser power	1 %	2 %
Emission detection	410-585 nm	493-630 nm

4.3.3 Tissue segmentation

Time-series microscopy data of *mScarlet-pcna*^{+/-}; *Tg(brachyury:Venus)*^{+/-} tail explants and images of whole embryos stained for PH3 and DAPI were opened in Labkit, a machine learning-based pixel classification tool available as a Fiji/ImageJ plugin [181]. As a first step in classifying pixels in the input image, multiple classes were defined; for data described in **Fig. 9**, these classes were ‘*embryonic tissue*’, ‘*extraembryonic tissue*’, and ‘*background*’; for data described in **Fig. 10**, **Fig. 11**, and **Fig. 12**, these classes were ‘*paraxial mesoderm*’, ‘*neural tube*’, ‘*notochord*’, ‘*extraembryonic tissue*’ and ‘*background*’. Next, some pixels corresponding to each class and spanning different z-slices – and, where applicable, different time points – were identified using morphological and gene expression landmarks. These pixels were manually labelled by drawing scribbles over them. The resulting labels were used to train a random forest classifier, which was then applied to the entire image to automatically assign all remaining pixels to one of the defined classes. Specifically, training was performed using sigma values 1.0, 2.0, 4.0, 8.0 and 16.0 and default filters (‘*original image*’, ‘*gaussian blur*’, ‘*difference of gaussians*’, ‘*gaussian gradient magnitude*’, ‘*laplacian of gaussian*’, ‘*hessian eigenvalues*’). Manual labelling and automatic segmentation steps were iterated multiple times until segmentation of desirable quality was achieved. Instead of using a single classifier to segment all samples, the above-described classification steps were performed for each sample independently, as this produced better segmentation.

The output of the segmentation was opened in Fiji by selecting *Segmentation > Show Probability Map in ImageJ*. The order of the dimensions in the resulting hyperstack was changed by selecting *Image > Hyperstacks > Stack to hyperstack* and choosing *xyztc*. This created a multi-channel file, where each channel corresponds to one class and indicates the confidence of each pixel belonging to that particular class by assigning pixels with continuous values from 0 to 1. This file was converted to 8-bit or 16-bit to match the raw data file. The raw data file was opened, following which channels from the probability map file and the raw data file were merged together.

The resulting *.tiff* file was converted to the *.ims* file format and imported in Imaris software. The voxel size was corrected in the *Edit > Image properties* menu. Time-resolved 3D surface reconstructions of each tissue were created automatically by using corresponding probability map channels as source channels in the Surfaces Creation Wizard. 3D surface reconstructions of the secondary body were created by clicking on the ‘*embryonic tissue*’ surface reconstruction and going to the *Edit > Cut* menu to cut it, at every consecutive stage, posterior to the somite that was the last formed somite at the onset of imaging. 3D surface reconstructions of the unsegmented PSM were created by clicking on the ‘*paraxial mesoderm*’ surface reconstruction and going to the *Edit > Cut* menu to cut it, at every consecutive stage, at the border between the last formed somite and the PSM at that stage.

4.3.4 Tissue length and volume measurements

Tissue length measurements were performed in Fiji. 3D surface reconstructions generated by Imaris were transformed into binary masks that can be opened in Fiji by clicking on the surface, selecting *Edit > Mask All*, choosing the mScarlet-pcna channel, and setting voxels outside the surface to 0 (‘*Duplicate channel before applying mask*’, ‘*Random color map*’, and ‘*Apply to all time points*’ checkboxes were ticked). This resulted in the creation of new channels, each representing a binary mask of one of the tissues. These channels were then opened in Fiji. Tissue length along the anteroposterior axis was measured at each consecutive time point by manually drawing a segmented line through the middle of the tissue, following its curvature. Tissue volume was extracted directly from Imaris by clicking on each surface, selecting *Statistics*, and exporting the data as a *.csv* file.

4.3.5 Quantification of PH3-positive cells in a tissue-specific manner

PH3-positive cells were masked in each individual tissue by clicking on a corresponding 3D surface reconstruction, selecting *Edit > Mask All*, choosing the PH3 channel, and setting voxels outside the surface to 0 (*'Duplicate channel before applying mask'* checkbox was ticked). This resulted in the creation of new channels, each representing PH3 expression in one of the tissues. These channels were then used as source channels in the Surfaces Creation Wizard to segment PH3-positive cells. Tissue-specific counts of PH3-positive cells were obtained directly from Imaris by clicking on the surface, selecting *Statistics*, and exporting the data as a .csv file.

4.4 Surgical size reduction

4.4.1 Preparation

Agarose plate. To hold embryos in place during cell removal, an agarose plate was prepared by pouring 1.5% agarose (Sigma, A9539) in H₂O into a 10 cm petri dish and placing a plastic mold containing 1 mm-wide protruding channels on top of it. Once agarose solidified, the mold was carefully lifted off with tweezers. The resulting agarose plate was filled with pre-chilled sterile 1X ERM, supplemented with 2% BSA (Equitech-Bio, BAC62) and 1% Penicillin-Streptomycin (Sigma, P4333).

Microneedles. Microneedles for cell removal were pulled from 1.2 mm (outer diameter) x 0.69 mm (inner diameter) x 150 mm (length) borosilicate glass capillaries without filament (Warner Instruments, W3 30-0041) on a needle puller (Sutter Instrument, P-97), using the following parameters: Heat = Ramp value + 5; Pull = 80; Vel = 70; Time = 100; P = 500. The tip of the needle was opened by gently touching it with fine forceps.

Cell removal device. A cell removal device was assembled with the help from the Centanin lab. 1 ml syringe (BD Plastipak, 300013) was connected to the PTFE tubing (Narishige, CT-1) via a tube connector (Narishige, CI-1). The other end of the PTFE tubing was attached to the needle holder (World Precision Instruments, order code MPH412) with a handle probe (World Precision Instruments, order code 2505). The microneedle was inserted

into the needle holder. The handle of the resulting cell removal device was then mounted on a micromanipulator (Narishige, MN-153).

4.4.2 Cell removal and cell counting

Dechorionated embryos at the Iwamatsu stage 10 (early blastula, approximately 1,000 cells) were gently transferred into the agarose plate. Using fine forceps, embryos were pushed into the troughs in the agarose plate and oriented with their blastoderms facing upwards. The microneedle was gently inserted into the embryo blastoderm at a 45° angle using the micromanipulator. Cells were slowly taken up into the microneedle by slowly pulling up the plunger of the syringe. To count the number of removed cells, cells were slowly expelled from the microneedle into the agarose plate and counted twice for each embryo under the microscope. After cell counting, each embryo was carefully transferred into a separate well of a 24-well cell culture dish, coated with 1.5% agarose and filled with sterile 1X ERM supplemented with 1% Penicillin-Streptomycin (Sigma, P4333). In experiments where cells were not counted, all cell removal embryos and all control embryos were pooled together and transferred into two separate 10 cm glass dishes. Dishes were then transferred to a 27°C incubator where embryos were allowed to develop until desired stages.

4.4.3 DAPI staining

All embryos for which cells were counted were kept in individual Eppendorf tubes throughout the following staining steps. In experiments where cells were not counted, all cell removal embryos and all control embryos were pooled into two separate Eppendorf tubes. Embryos were fixed in 4% paraformaldehyde (Electron Microscopy Sciences, 15710) in 2X PBS for 4 hours at room temperature. After fixation, they were washed 4 x 5 minutes in PTw. Embryos were dehydrated in gradually increasing concentrations of methanol in PTw (25%, 50%, 75% and 100%, 10 minutes each). 100% methanol was then replaced with fresh 100% methanol and embryos were kept overnight at -20°C. On the next day, embryos were rehydrated in gradually decreasing concentrations of methanol in PTw (75%, 50% and 25%, 5 minutes each), followed by 3 x 10 minutes washes in PTw. *In situ* hybridization chain reaction was performed following the protocol detailed on the Molecular Instruments web page (MI-Protocol-RNAFISH-Zebrafish; Revision Number: 9). Following *in situ*

hybridization chain reaction, embryos were incubated in 50 µg/ml DAPI (Merck, 10236276001) in 5X SSCT for 7 hours at 4°C.

4.4.4 Embryo mounting and imaging

Stained embryos were cleared in 50% glycerol (Merck, 1370282500) in PBS for 1 hour at 4°C, followed by an overnight incubation in 100% glycerol at 4°C. Embryos were de-yolked and flat mounted in 100% glycerol. Embryos were imaged on the Zeiss LSM 780 laser-scanning microscope with the following settings:

	DAPI imaging
Objective lens	Plan-Neofluar 10x/0.30
Zoom	0.6x
Dimensions	1024 x 1024 pixels, 63-118 slices, 16-bit
xy resolution	1.384 µm/pixel
z interval	2 µm
Pixel dwell	0.79 µsec
Pinhole	90 µm
Excitation	405 nm (30 mW Diode laser)
Laser power	5.5%
Emission detection	410-585 nm

4.5 Pharmacological perturbation of axis elongation

4.5.1 Aphidicolin treatment

Aphidicolin (Merck, A0781) was used to inhibit the cell cycle in developing tail explants. A stock solution of 3.75 mM was prepared by dissolving aphidicolin powder in DMSO (Merck, D2650). It was then aliquoted and stored in the dark at -20°C until needed. Tail explants dissected at Iwamatsu stage 23 (12-14 ss) were incubated in culture medium supplemented with aphidicolin at a final concentration of 30 µM (DMSO concentration – 0.4%). Control tail explants were incubated in culture medium supplemented with DMSO at a final concentration of 0.4%.

4.5.2 Antibody staining

Tail explants were fixed in 4% paraformaldehyde (Electron Microscopy Sciences, 15710) in 1X PBS for 2 hours at room temperature (some of them were also moved to 4°C for up to 3 hours before commencing with the next step). After fixation, tail explants were washed 4 x 5 minutes in PTw, followed by a wash in dH₂O. Next, samples were moved into a glass vial and permeabilized with pre-chilled acetone for 5 minutes at -20°C. This was followed by washes in dH₂O and PTw. Samples were then incubated in blocking buffer (1% BSA (Equitech-Bio, BAC62), 0.1X PTw, 1% DMSO (Merck, D2650), 4% donkey serum (abcam, ab7475) in dH₂O) for 1 hour at room temperature with rotation. The primary antibody, rabbit monoclonal anti-PH3 (Cell signaling technology, #3642), was diluted 1:200 in blocking buffer and tail explants were incubated in this solution overnight at 4°C with rotation. On the next day, tail explants were washed 6 times in PTw. In all subsequent steps, care was taken to minimize sample exposure to light. The secondary antibody, donkey anti-rabbit Alexa Fluor 594 (Thermo Fisher, A-21207), and the nuclear stain Hoechst 33342 (Thermo Fisher, H3570) were diluted 1:1000 and 1:500, respectively, in blocking buffer and tail explants were incubated in this solution for 2 hours at room temperature with rotation. Tail explants were washed 6 times in PTw.

4.5.3 Tail explant mounting and imaging

Live imaging. Tail explants from the cross of *her7-Venus^{+/+}* females and *Cab* males were mounted as described in 4.4.2 and imaged on the Zeiss LSM 780 laser-scanning microscope with the following settings:

	Venus imaging
Objective lens	Plan-Apochromat 20x/0.8
Zoom	0.6x
Dimensions	512 x 512 pixels, 5 slices, 16-bit
xy resolution	1.384 $\mu\text{m}/\text{pixel}$
z interval	7 μm
Pixel dwell	2.55 μsec
Averaging	Line, 8
Pinhole	601 μm
Imaging interval	10 min
Imaging duration	10 h
Excitation	514 nm (25 mW Argon laser)
Laser power	6.5%
Emission detection	517-577 nm

Imaging of stained tail explants. Tail explants stained for PH3 and Hoechst were cleared in 50% glycerol (Merck, 1370282500) in PTw for 30 minutes at 4°C and subsequently flat mounted in 50% glycerol in PTw. Tail explants were imaged on the Zeiss LSM 780 laser-scanning microscope with the following settings:

	Hoechst imaging	Alexa 594 imaging
Objective lens	Plan-Apochromat 20x/0.8	
Zoom	1.0x	
Dimensions	512 x 512 pixels, 35-50 slices, 16-bit	
xy resolution	0.830 $\mu\text{m}/\text{pixel}$	
z interval	2.5 μm	
Pixel dwell	2.54 μsec	
Averaging	Line, 4	
Pinhole	90 μm	
Excitation	405 nm (30 mW Diode laser)	594 nm (2 mW Helium-neon laser)
Laser power	0.6%	2.8%
Emission detection	410-579 nm	599-734 nm

4.5.4 Quantification of PH3-positive cells

Stained tail explants were segmented, their 3D surface reconstructions created, and tissue volume extracted as described in 4.3.3 and 4.3.4. PH3-positive cells were segmented

using the Surfaces Creation Wizard. Tissue-specific counts of PH3-positive cells were obtained directly from Imaris by clicking on the surface, selecting *Statistics*, and exporting the data as a .csv file.

4.5.5 Time-series image registration

Image registration was performed in Fiji using the *MultiStackReg* plugin (available at <http://bradbusse.net/downloads.html>).

4.5.6 Length measurements

All measurements were performed in Fiji using the brightfield channel. To quantify anteroposterior axis elongation, the last somite boundary that had been formed at the onset of imaging was used as an anterior reference point. Axis elongation was measured by drawing a segmented line through the middle of the tissue between this point and the tailbud over time. PSM length along the anteroposterior axis was measured at each time point a new somite pair had formed by manually drawing a segmented line through the middle of the tissue between the tailbud and the posterior boundary of the nascent somite. The length of nascent somites along the anteroposterior axis was measured at the time of their formation by averaging the length of three parallel lines drawn from the anterior to the posterior boundary of the somite.

4.5.7 Quantification of signaling dynamics

Quantification of posterior period. To generate intensity kymographs, image stacks of *her7-Venus^{+/-}* tail explants were projected in the *z*-axis by maximum intensity and smoothed with a Gaussian blur filter ($\sigma = 4$) in Fiji. A ten-pixel wide segmented line was drawn along the length of the tail explant, in the posterior to anterior direction. Pixel intensities along this line were extracted for each time point and plotted as a two-dimensional intensity kymograph (where the *x*-axis represents time and the *y*-axis represents space) using the *KymoResliceWide* plugin (available at <https://github.com/UU-cellbiology/KymoResliceWide>). Next, period kymographs were generated by applying wavelet analysis on each horizontal line in the intensity kymograph, using the open-source tool pyBOAT (available at <https://github.com/tensionhead/pyBOAT>) with the following parameters:

	Wavelet analysis
Sampling interval	10 min
Range of periods to scan for	50-150 min
Number of periods to scan for	600
Cut-off period	150 min
Max power	15

A binary mask was created to separate pixels corresponding to Her7-Venus signal in the PSM and those corresponding to the background. This was done by manually outlining the oscillatory region in the intensity kymograph using the polygon selection in Fiji. The mask was then applied to the period kymograph. To obtain posterior period values, periods found in the posterior-most 20% of the masked period kymograph were averaged for each time point (starting from 150 min), using a script by Carina Vibe. Next, posterior periods were averaged across time for each tail explant to obtain a single posterior period value per sample.

Extraction of period and phase gradient profiles. *her7-Venus*^{+/-} tail explant data was projected in the z-axis by maximum intensity and smoothed with a Gaussian blur filter ($\sigma = 4$) in Fiji. Wavelet movies were generated by applying wavelet analysis on each pixel in the time-series data, using the open-source tool Spatial pyBOAT (available at <https://github.com/tensionhead/SpyBOAT>) and the following parameters:

	Wavelet analysis
Sampling interval	10 min
Range of periods to scan for	50-150 min
Number of periods to scan for	120
Cut-off period	150 min
Max power	15

Segmented lines corresponding to the length of the PSM (described in 4.5.6) were reused in this analysis to obtain period and phase gradient profiles along the PSM at each time point a new somite pair had formed. 20 pixel and one-pixel wide lines were used to extract period and phase gradient data along the PSM, respectively. Phase unwrapping using the *numpy.unwrap* function in Python was used to make phase values continuous. Period and phase gradients were plotted and analyzed using scripts by Carina Vibe and Takehito Tomita.

5 Bibliography

1. Leibovich, A., et al., *Natural size variation among embryos leads to the corresponding scaling in gene expression*. *Developmental Biology*, 2020. **462**(2): p. 165-179.
2. Tung, T.C.T., Y. F. Y, *The development of egg-fragments, isolated blastomeres and fused eggs in the goldfish*. *Proceedings of the Zoological Society of London*, 1944. **114**: p. 46–64.
3. Cooke, J., *Control of somite number during morphogenesis of a vertebrate, Xenopus laevis*. *Nature*, 1975. **254**(5497): p. 196-9.
4. Cooke, J., *Scale of Body Pattern Adjusts to Available Cell Number in Amphibian Embryos*. *Nature*, 1981. **290**(5809): p. 775-778.
5. Ishimatsu, K., et al., *Size-reduced embryos reveal a gradient scaling-based mechanism for zebrafish somite formation*. *Development*, 2018. **145**(11).
6. Huang, Y. and D.M. Umulis, *Scale invariance of BMP signaling gradients in zebrafish*. *Scientific Reports*, 2019. **9**.
7. Almuedo-Castillo, M., et al., *Scale-invariant patterning by size-dependent inhibition of Nodal signalling*. *Nature Cell Biology*, 2018. **20**(9): p. 1032-+.
8. Snow, M.H.L. and P.P.L. Tam, *Is Compensatory Growth a Complicating Factor in Mouse Teratology*. *Nature*, 1979. **279**(5713): p. 555-557.
9. Power, M.A. and P.P.L. Tam, *Onset of Gastrulation, Morphogenesis and Somitogenesis in Mouse Embryos Displaying Compensatory Growth*. *Anatomy and Embryology*, 1993. **187**(5): p. 493-504.
10. Tam, P.P.L., *The Control of Somitogenesis in Mouse Embryos*. *Journal of Embryology and Experimental Morphology*, 1981. **65**: p. 103-128.
11. Morgan, T.H., *Regeneration*. Columbia University biological series VII. 1901, New York, London,: The Macmillan Company; Macmillan & Co., ltd. xii p., 1 l., 316 p.
12. Maden, M., *Morphallaxis in an Epimorphic System - Size, Growth-Control and Pattern-Formation during Amphibian Limb Regeneration*. *Journal of Embryology and Experimental Morphology*, 1981. **65**: p. 151-167.
13. Benazeraf, B. and O. Pourquie, *Formation and Segmentation of the Vertebrate Body Axis*. *Annual Review of Cell and Developmental Biology*, Vol 29, 2013. **29**: p. 1-26.
14. Bone, R.A., et al., *Spatiotemporal oscillations of Notch1, Dll1 and NICD are coordinated across the mouse PSM*. *Development*, 2014. **141**(24): p. 4806-4816.
15. Maroto, M., R.A. Bone, and J.K. Dale, *Somitogenesis*. *Development*, 2012. **139**(14): p. 2453-2456.
16. Lauschke, V.M., et al., *Scaling of embryonic patterning based on phase-gradient encoding*. *Nature*, 2013. **493**(7430): p. 101-106.
17. Xiong, F.Z., et al., *Mechanical Coupling Coordinates the Co-elongation of Axial and Paraxial Tissues in Avian Embryos*. *Developmental Cell*, 2020. **55**(3): p. 354-366.
18. Mongera, A., et al., *Mechanics of Anteroposterior Axis Formation in Vertebrates*. *Annual Review of Cell and Developmental Biology*, Vol 35, 2019. **35**: p. 259-283.
19. O'Farrell, P.H., *Growing an Embryo from a Single Cell: A Hurdle in Animal Life*. *Cold Spring Harbor Perspectives in Biology*, 2015. **7**(11).

20. Keller, R.E., et al., *The Function and Mechanism of Convergent Extension during Gastrulation of Xenopus-Laevis*. Journal of Embryology and Experimental Morphology, 1985. **89**: p. 185-209.
21. Keller, R. and P. Tibbetts, *Mediolateral Cell Intercalation in the Dorsal, Axial Mesoderm of Xenopus-Laevis*. Developmental Biology, 1989. **131**(2): p. 539-549.
22. Keller, R., et al., *Cell Intercalation during Notochord Development in Xenopus-Laevis*. Journal of Experimental Zoology, 1989. **251**(2): p. 134-154.
23. Wilson, P.A., G. Oster, and R. Keller, *Cell Rearrangement and Segmentation in Xenopus - Direct Observation of Cultured Explants*. Development, 1989. **105**(1): p. 155-166.
24. Keller, R., J. Shih, and A. Sater, *The Cellular Basis of the Convergence and Extension of the Xenopus Neural Plate*. Developmental Dynamics, 1992. **193**(3): p. 199-217.
25. Elul, T., M.A.R. Koehl, and R. Keller, *Cellular mechanism underlying neural convergent extension in Xenopus laevis embryos*. Developmental Biology, 1997. **191**(2): p. 243-258.
26. Kimmel, C.B. and R.M. Warga, *Cell Lineages Generating Axial Muscle in the Zebrafish Embryo*. Nature, 1987. **327**(6119): p. 234-237.
27. Warga, R.M. and C.B. Kimmel, *Cell Movements during Epiboly and Gastrulation in Zebrafish*. Development, 1990. **108**(4): p. 569-580.
28. Glickman, N.S., et al., *Shaping the zebrafish notochord*. Development, 2003. **130**(5): p. 873-887.
29. Sepich, D.S., et al., *Initiation of convergence and extension movements of lateral mesoderm during zebrafish gastrulation*. Developmental Dynamics, 2005. **234**(2): p. 279-292.
30. Wang, J.B., et al., *Dishevelled genes mediate a conserved mammalian PCP pathway to regulate convergent extension during neurulation*. Development, 2006. **133**(9): p. 1767-1778.
31. Ybot-Gonzalez, P., et al., *Convergent extension, planar-cell-polarity signalling and initiation of mouse neural tube closure*. Development, 2007. **134**(4): p. 789-799.
32. Yamanaka, Y., et al., *Live imaging and genetic analysis of mouse notochord formation reveals regional morphogenetic mechanisms*. Developmental Cell, 2007. **13**(6): p. 884-896.
33. Yen, W.W., et al., *PTK7 is essential for polarized cell motility and convergent extension during mouse gastrulation*. Development, 2009. **136**(12): p. 2039-2048.
34. Nishimura, T., H. Honda, and M. Takeichi, *Planar Cell Polarity Links Axes of Spatial Dynamics in Neural-Tube Closure*. Cell, 2012. **149**(5): p. 1084-1097.
35. Steventon, B., et al., *Species-specific contribution of volumetric growth and tissue convergence to posterior body elongation in vertebrates*. Development, 2016. **143**(10): p. 1732-1741.
36. Delfini, M.C., et al., *Control of the segmentation process by graded MAPK/ERK activation in the chick embryo*. Proceedings of the National Academy of Sciences of the United States of America, 2005. **102**(32): p. 11343-11348.
37. Benazeraf, B., et al., *A random cell motility gradient downstream of FGF controls elongation of an amniote embryo*. Nature, 2010. **466**(7303): p. 248-252.

38. Lawton, A.K., et al., *Regulated tissue fluidity steers zebrafish body elongation*. Development, 2013. **140**(3): p. 573-582.
39. Benazeraf, B., et al., *Multi-scale quantification of tissue behavior during amniote embryo axis elongation*. Development, 2017. **144**(23): p. 4462-4472.
40. Regev, I., et al., *Motility-gradient induced elongation of the vertebrate embryo*. bioRxiv, 2017.
41. Mongera, A., et al., *A fluid-to-solid jamming transition underlies vertebrate body axis elongation*. Nature, 2018. **561**(7723): p. 401-+.
42. Sambasivan, R. and B. Steventon, *Neuromesodermal Progenitors: A Basis for Robust Axial Patterning in Development and Evolution*. Frontiers in Cell and Developmental Biology, 2021. **8**.
43. Su, T.T. and P.H. O'Farrell, *Size control: Cell proliferation does not equal growth*. Current Biology, 2009. **8**(19): p. R687-R689.
44. Martin, B.L. and D. Kimelman, *Wnt signaling and the evolution of embryonic posterior development*. Curr Biol, 2009. **19**(5): p. R215-9.
45. Nicolas, J.F., L. Mathis, and C. Bonnerot, *Evidence in the mouse for self-renewing stem cells in the formation of a segmented longitudinal structure, the myotome*. Development, 1996. **122**(9): p. 2933-2946.
46. Mathis, L. and J.F. Nicolas, *Different clonal dispersion in the rostral and caudal mouse central nervous system*. Development, 2000. **127**(6): p. 1277-1290.
47. Mathis, L., et al., *Successive patterns of clonal cell dispersion in relation to neuromeric subdivision in the mouse neuroepithelium*. Development, 1999. **126**(18): p. 4095-4106.
48. Tzouanacou, E., et al., *Redefining the Progression of Lineage Segregations during Mammalian Embryogenesis by Clonal Analysis*. Developmental Cell, 2009. **17**(3): p. 365-376.
49. Guillot, C., et al., *Dynamics of primitive streak regression controls the fate of neuromesodermal progenitors in the chicken embryo*. Elife, 2021. **10**.
50. Henrique, D., et al., *Neuromesodermal progenitors and the making of the spinal cord*. Development, 2015. **142**(17): p. 2864-+.
51. Kanki, J.P. and R.K. Ho, *The development of the posterior body in zebrafish*. Development, 1997. **124**(4): p. 881-893.
52. Martin, B.L. and D. Kimelman, *Canonical Wnt Signaling Dynamically Controls Multiple Stem Cell Fate Decisions during Vertebrate Body Formation*. Developmental Cell, 2012. **22**(1): p. 223-232.
53. Martin, B.L. and B. Steventon, *A fishy tail: Insights into the cell and molecular biology of neuromesodermal cells from zebrafish embryos*. Developmental Biology, 2022. **487**: p. 67-73.
54. Attardi, A., et al., *Neuromesodermal progenitors are a conserved source of spinal cord with divergent growth dynamics (vol 145, dev166728, 2018)*. Development, 2019. **146**(2).
55. Bouldin, C.M., et al., *Restricted expression of cdc25a in the tailbud is essential for formation of the zebrafish posterior body*. Genes & Development, 2014. **28**(4): p. 384-395.

56. Bulusu, V., et al., *Spatiotemporal Analysis of a Glycolytic Activity Gradient Linked to Mouse Embryo Mesoderm Development*. *Developmental Cell*, 2017. **40**(4): p. 331-341.
57. Bancroft, M. and R. Bellairs, *Development of Notochord in Chick-Embryo, Studied by Scanning and Transmission Electron-Microscopy*. *Journal of Embryology and Experimental Morphology*, 1976. **35**(Apr): p. 383-401.
58. Adams, D.S., R. Keller, and M.A.R. Koehl, *The Mechanics of Notochord Elongation, Straightening and Stiffening in the Embryo of Xenopus-Laevis*. *Development*, 1990. **110**(1): p. 115-130.
59. Ellis, K., J. Bagwell, and M. Bagnat, *Notochord vacuoles are lysosome-related organelles that function in axis and spine morphogenesis*. *Journal of Cell Biology*, 2013. **200**(5): p. 667-679.
60. McLaren, S.B.P. and B.J. Steventon, *Anterior expansion and posterior addition to the notochord mechanically coordinate zebrafish embryo axis elongation*. *Development*, 2021. **148**(18).
61. Seleit, A., et al., *Development and regeneration dynamics of the Medaka notochord*. *Developmental Biology*, 2020. **463**(1): p. 11-25.
62. Cooke, J. and E.C. Zeeman, *A clock and wavefront model for control of the number of repeated structures during animal morphogenesis*. *J Theor Biol*, 1976. **58**(2): p. 455-76.
63. Goodwin, B.C. and M.H. Cohen, *A phase-shift model for the spatial and temporal organization of developing systems*. *J Theor Biol*, 1969. **25**(1): p. 49-107.
64. Wolpert, L., *Positional information and the spatial pattern of cellular differentiation*. *J Theor Biol*, 1969. **25**(1): p. 1-47.
65. Palmeirim, I., et al., *Avian hairy gene expression identifies a molecular clock linked to vertebrate segmentation and somitogenesis*. *Cell*, 1997. **91**(5): p. 639-48.
66. Sasai, Y., et al., *Two mammalian helix-loop-helix factors structurally related to Drosophila hairy and Enhancer of split*. *Genes Dev*, 1992. **6**(12B): p. 2620-34.
67. Kageyama, R., T. Ohtsuka, and T. Kobayashi, *The Hes gene family: repressors and oscillators that orchestrate embryogenesis*. *Development*, 2007. **134**(7): p. 1243-1251.
68. Fischer, A. and M. Gessler, *Delta-Notch-and then? Protein interactions and proposed modes of repression by Hes and Hey bHLH factors*. *Nucleic Acids Research*, 2007. **35**(14): p. 4583-4596.
69. Jouve, C., et al., *Notch signalling is required for cyclic expression of the hairy-like gene HES1 in the presomitic mesoderm*. *Development*, 2000. **127**(7): p. 1421-1429.
70. Bessho, Y., et al., *Dynamic expression and essential functions of Hes7 in somite segmentation*. *Genes & Development*, 2001. **15**(20): p. 2642-2647.
71. Leimeister, C., et al., *Oscillating expression of c-Hey2 in the presomitic mesoderm suggests that the segmentation clock may use combinatorial signaling through multiple interacting bHLH factors*. *Developmental Biology*, 2000. **227**(1): p. 91-103.
72. Li, Y., et al., *Cyclic expression of esr9 gene in Xenopus presomitic mesoderm*. *Differentiation*, 2003. **71**(1): p. 83-89.
73. Holley, S.A., R. Geisler, and C. Nusslein-Volhard, *Control of her1 expression during zebrafish somitogenesis by a Delta-dependent oscillator and an independent wave-front activity*. *Genes & Development*, 2000. **14**(13): p. 1678-1690.

74. Sawada, A., et al., *Zebrafish Mesp family genes, mesp-a and mesp-b are segmentally expressed in the presomitic mesoderm, and Mesp-b confers the anterior identity to the developing somites*. *Development*, 2000. **127**(8): p. 1691-1702.
75. Oates, A.C. and R.K. Ho, *Hairy/E(spl)-related (Her) genes are central components of the segmentation oscillator and display redundancy with the Delta/Notch signaling pathway in the formation of anterior segmental boundaries in the zebrafish*. *Development*, 2002. **129**(12): p. 2929-2946.
76. Sieger, D., D. Tautz, and M. Gajewski, *her11 is involved in the somitogenesis clock in zebrafish*. *Development Genes and Evolution*, 2004. **214**(8): p. 393-406.
77. Elmasri, H., et al., *her7 and hey1, but not lunatic fringe show dynamic expression during somitogenesis in medaka (Oryzias latipes)*. *Gene Expression Patterns*, 2004. **4**(5): p. 553-559.
78. Gajewski, M., et al., *Comparative analysis of her genes during fish somitogenesis suggests a mouse/chick-like mode of oscillation in medaka*. *Development Genes and Evolution*, 2006. **216**(6): p. 315-332.
79. Forsberg, H., F. Crozet, and N.A. Brown, *Waves of mouse Lunatic fringe expression, in four-hour cycles at two-hour intervals, precede somite boundary formation*. *Current Biology*, 1998. **8**(18): p. 1027-1030.
80. McGrew, M.J., et al., *The lunatic Fringe gene is a target of the molecular clock linked to somite segmentation in avian embryos*. *Current Biology*, 1998. **8**(17): p. 979-982.
81. Aulehla, A. and R.L. Johnson, *Dynamic expression of lunatic fringe suggests a link between notch signaling and an autonomous cellular oscillator driving somite segmentation*. *Developmental Biology*, 1999. **207**(1): p. 49-61.
82. Jiang, Y.J., et al., *Notch signalling and the synchronization of the somite segmentation clock*. *Nature*, 2000. **408**(6811): p. 475-479.
83. Dequeant, M.L., et al., *A complex oscillating network of signaling genes underlies the mouse segmentation clock*. *Science*, 2006. **314**(5805): p. 1595-1598.
84. Krol, A.J., et al., *Evolutionary plasticity of segmentation clock networks*. *Development*, 2011. **138**(13): p. 2783-2792.
85. Dale, J.K., et al., *Oscillations of the snail genes in the presomitic mesoderm coordinate segmental patterning and morphogenesis in vertebrate somitogenesis*. *Developmental Cell*, 2006. **10**(3): p. 355-366.
86. Niwa, Y., et al., *The initiation and propagation of hes7 oscillation are cooperatively regulated by fgf and notch signaling in the somite segmentation clock*. *Developmental Cell*, 2007. **13**(2): p. 298-304.
87. Hayashi, S., et al., *Sprouty4, an FGF Inhibitor, Displays Cyclic Gene Expression under the Control of the Notch Segmentation Clock in the Mouse PSM*. *Plos One*, 2009. **4**(5).
88. Aulehla, A., et al., *Wnt3A plays a major role in the segmentation clock controlling somitogenesis*. *Developmental Cell*, 2003. **4**(3): p. 395-406.
89. Ishikawa, A., et al., *Mouse Nkd1, a Wnt antagonist, exhibits oscillatory gene expression in the PSM under the control of Notch signaling*. *Mechanisms of Development*, 2004. **121**(12): p. 1443-1453.

90. Suriben, R., D.A. Fisher, and B.N.R. Cheyette, *Dact1 presomitic mesoderm expression oscillates in phase with Axin2 in the somitogenesis clock of mice*. *Developmental Dynamics*, 2006. **235**(11): p. 3177-3183.
91. Matsuda, M., et al., *Recapitulating the human segmentation clock with pluripotent stem cells*. *Nature*, 2020. **580**(7801): p. 124-+.
92. Chu, L.F., et al., *An In Vitro Human Segmentation Clock Model Derived from Embryonic Stem Cells*. *Cell Reports*, 2019. **28**(9): p. 2247-+.
93. Friesen, W.O. and G.D. Block, *What Is a Biological Oscillator*. *American Journal of Physiology*, 1984. **246**(6): p. R847-R851.
94. Bessho, Y., et al., *Periodic repression by the bHLH factor Hes7 is an essential mechanism for the somite segmentation clock*. *Genes Dev*, 2003. **17**(12): p. 1451-6.
95. Takebayashi, K., et al., *Structure, Chromosomal Locus, and Promoter Analysis of the Gene Encoding the Mouse Helix-Loop-Helix Factor Hes-1 - Negative Autoregulation through the Multiple N-Box Elements*. *Journal of Biological Chemistry*, 1994. **269**(7): p. 5150-5156.
96. Hirata, H., et al., *Oscillatory expression of the bHLH factor Hes1 regulated by a negative feedback loop*. *Science*, 2002. **298**(5594): p. 840-843.
97. Giudicelli, F., et al., *Setting the tempo in development: An investigation of the zebrafish somite clock mechanism*. *Plos Biology*, 2007. **5**(6): p. 1309-1323.
98. Chen, J., L. Kang, and N. Zhang, *Negative feedback loop formed by lunatic fringe and Hes7 controls their oscillatory expression during somitogenesis*. *Genesis*, 2005. **43**(4): p. 196-204.
99. Brend, T. and S.A. Holley, *Expression of the Oscillating Gene her1 Is Directly Regulated by Hairy/Enhancer of Split, T-Box, and Suppressor of Hairless Proteins in the Zebrafish Segmentation Clock*. *Developmental Dynamics*, 2009. **238**(11): p. 2745-2759.
100. Ferjentsik, Z., et al., *Notch Is a Critical Component of the Mouse Somitogenesis Oscillator and Is Essential for the Formation of the Somites*. *Plos Genetics*, 2009. **5**(9).
101. Lewis, J., *Autoinhibition with transcriptional delay: A simple mechanism for the zebrafish somitogenesis oscillator*. *Current Biology*, 2003. **13**(16): p. 1398-1408.
102. Monk, N.A.M., *Oscillatory expression of Hes1, p53, and NF-kappa B driven by transcriptional time delays*. *Current Biology*, 2003. **13**(16): p. 1409-1413.
103. Takashima, Y., et al., *Intronic delay is essential for oscillatory expression in the segmentation clock*. *Proceedings of the National Academy of Sciences of the United States of America*, 2011. **108**(8): p. 3300-3305.
104. Harima, Y., et al., *Accelerating the Tempo of the Segmentation Clock by Reducing the Number of Introns in the Hes7 Gene*. *Cell Reports*, 2013. **3**(1): p. 1-7.
105. Hoyle, N.P. and D. Ish-Horowicz, *Transcript processing and export kinetics are rate-limiting steps in expressing vertebrate segmentation clock genes*. *Proceedings of the National Academy of Sciences of the United States of America*, 2013. **110**(46): p. E4316-E4324.
106. Maroto, M., et al., *Synchronised cycling gene oscillations in presomitic mesoderm cells require cell-cell contact*. *International Journal of Developmental Biology*, 2005. **49**(2-3): p. 309-315.

107. Gomez, C., et al., *Control of segment number in vertebrate embryos*. Nature, 2008. **454**(7202): p. 335-339.
108. Shih, N.P., et al., *Dynamics of the slowing segmentation clock reveal alternating two-segment periodicity*. Development, 2015. **142**(10): p. 1785-1793.
109. Tsiairis, C.D. and A. Aulehla, *Self-Organization of Embryonic Genetic Oscillators into Spatiotemporal Wave Patterns*. Cell, 2016. **164**(4): p. 656-667.
110. Yoshioka-Kobayashi, K., et al., *Coupling delay controls synchronized oscillation in the segmentation clock*. Nature, 2020. **580**(7801): p. 119-+.
111. Rohde, L.A., et al., *Cell-autonomous generation of the wave pattern within the vertebrate segmentation clock*. bioRxiv, 2021.
112. Vibe, C.B., *The temperature response of the medaka segmentation clock and its link to robustness in embryonic patterning*. 2020, Ruprecht Karl University of Heidelberg.
113. Falk, H.J., et al., *Imaging the onset of oscillatory signaling dynamics during mouse embryo gastrulation*. Development, 2022. **149**(13).
114. Julich, D., et al., *beamter/deltaC and the role of Notch ligands in the zebrafish somite segmentation, hindbrain neurogenesis and hypochord differentiation*. Developmental Biology, 2005. **286**(2): p. 391-404.
115. Horikawa, K., et al., *Noise-resistant and synchronized oscillation of the segmentation clock*. Nature, 2006. **441**(7094): p. 719-723.
116. Masamizu, Y., et al., *Real-time imaging of the somite segmentation clock: Revelation of unstable oscillators in the individual presomitic mesoderm cells*. Proceedings of the National Academy of Sciences of the United States of America, 2006. **103**(5): p. 1313-1318.
117. Webb, A.B., et al., *Persistence, period and precision of autonomous cellular oscillators from the zebrafish segmentation clock*. Elife, 2016. **5**.
118. Ozbudak, E.M. and J. Lewis, *Notch signalling synchronizes the zebrafish segmentation clock but is not needed to create somite boundaries*. Plos Genetics, 2008. **4**(2).
119. Delaune, E.A., et al., *Single-Cell-Resolution Imaging of the Impact of Notch Signaling and Mitosis on Segmentation Clock Dynamics*. Developmental Cell, 2012. **23**(5): p. 995-1005.
120. Riedel-Kruse, I.H., C. Muller, and A.C. Oates, *Synchrony dynamics during initiation, failure, and rescue of the segmentation clock*. Science, 2007. **317**(5846): p. 1911-1915.
121. Okubo, Y., et al., *Lfng regulates the synchronized oscillation of the mouse segmentation clock via trans-repression of Notch signalling*. Nature Communications, 2012. **3**.
122. Elsdale, T., M. Pearson, and M. Whitehead, *Abnormalities in Somite Segmentation Following Heat Shock to Xenopus Embryos*. Journal of Embryology and Experimental Morphology, 1976. **35**(Jun): p. 625-635.
123. Dubrulle, J., M.J. McGrew, and O. Pourquie, *FGF signaling controls somite boundary position and regulates segmentation clock control of spatiotemporal Hox gene activation*. Cell, 2001. **106**(2): p. 219-32.
124. Bajard, L., et al., *Wnt-regulated dynamics of positional information in zebrafish somitogenesis*. Development, 2014. **141**(6): p. 1381-1391.

125. Primmatt, D.R.N., et al., *Periodic Segmental Anomalies Induced by Heat-Shock in the Chick-Embryo Are Associated with the Cell-Cycle*. *Development*, 1989. **105**(1): p. 119-130.
126. Roy, M.N., V.E. Prince, and R.K. Ho, *Heat shock produces periodic somitic disturbances in the zebrafish embryo*. *Mechanisms of Development*, 1999. **85**(1-2): p. 27-34.
127. Aulehla, A., et al., *A beta-catenin gradient links the clock and wavefront systems in mouse embryo segmentation*. *Nature Cell Biology*, 2008. **10**(2): p. 186-U56.
128. Dubrulle, J. and O. Pourquie, *fgf8 mRNA decay establishes a gradient that couples axial elongation to patterning in the vertebrate embryo*. *Nature*, 2004. **427**(6973): p. 419-422.
129. Sawada, A., et al., *Fgf/MAPK signalling is a crucial positional cue in somite boundary formation*. *Development*, 2001. **128**(23): p. 4873-4880.
130. Rossant, J., et al., *Expression of a Retinoic Acid Response Element-HsplacZ Transgene Defines Specific Domains of Transcriptional Activity during Mouse Embryogenesis*. *Genes & Development*, 1991. **5**(8): p. 1333-1344.
131. Shimozono, S., et al., *Visualization of an endogenous retinoic acid gradient across embryonic development*. *Nature*, 2013. **496**(7445): p. 363-+.
132. Moreno, T.A. and C. Kintner, *Regulation of segmental patterning by retinoic acid signaling during Xenopus somitogenesis*. *Developmental Cell*, 2004. **6**(2): p. 205-218.
133. Blentic, A., E. Gale, and M. Maden, *Retinoic acid signalling centres in the avian embryo identified by sites of expression of synthesising and catabolising enzymes*. *Developmental Dynamics*, 2003. **227**(1): p. 114-127.
134. Aulehla, A. and B.G. Herrmann, *Segmentation in vertebrates: clock and gradient finally joined*. *Genes & Development*, 2004. **18**(17): p. 2060-2067.
135. Zhao, D., et al., *Molecular identification of a major retinoic-acid-synthesizing enzyme, a retinaldehyde-specific dehydrogenase*. *European Journal of Biochemistry*, 1996. **240**(1): p. 15-22.
136. Niederreither, K., et al., *Restricted expression and retinoic acid-induced downregulation of the retinaldehyde dehydrogenase type 2 (RALDH-2) gene during mouse development*. *Mechanisms of Development*, 1997. **62**(1): p. 67-78.
137. White, J.A., et al., *Identification of the retinoic acid-inducible all-trans-retinoic acid 4-hydroxylase*. *Journal of Biological Chemistry*, 1996. **271**(47): p. 29922-29927.
138. Fujii, H., et al., *Metabolic inactivation of retinoic acid by a novel P450 differentially expressed in developing mouse embryos*. *Embo Journal*, 1997. **16**(14): p. 4163-4173.
139. Sakai, Y., et al., *The retinoic acid-inactivating enzyme CYP26 is essential for establishing an uneven distribution of retinoic acid along the antero-posterior axis within the mouse embryo*. *Genes & Development*, 2001. **15**(2): p. 213-225.
140. Naiche, L.A., N. Holder, and M. Lewandoski, *FGF4 and FGF8 comprise the wavefront activity that controls somitogenesis*. *Proceedings of the National Academy of Sciences of the United States of America*, 2011. **108**(10): p. 4018-4023.
141. Diez del Corral, R., et al., *Opposing FGF and retinoid pathways control ventral neural pattern, neuronal differentiation, and segmentation during body axis extension*. *Neuron*, 2003. **40**(1): p. 65-79.

142. Abu-Abed, S., et al., *Developing with lethal RA levels: genetic ablation of Rarg can restore the viability of mice lacking Cyp26a1*. *Development*, 2003. **130**(7): p. 1449-1459.
143. Olivera-Martinez, I. and K.G. Storey, *Wnt signals provide a timing mechanism for the FGF-retinoid differentiation switch during vertebrate body axis extension*. *Development*, 2007. **134**(11): p. 2125-2135.
144. Stavridis, M.P., B.J. Collins, and K.G. Storey, *Retinoic acid orchestrates fibroblast growth factor signalling to drive embryonic stem cell differentiation*. *Development*, 2010. **137**(6): p. 881-890.
145. Dunty, W.C., et al., *Wnt3a/beta-catenin signaling controls posterior body development by coordinating mesoderm formation and segmentation*. *Development*, 2008. **135**(1): p. 85-94.
146. Vermot, J., et al., *Retinoic acid controls the bilateral symmetry of somite formation in the mouse embryo*. *Science*, 2005. **308**(5721): p. 563-566.
147. Sonnen, K.F., et al., *Modulation of Phase Shift between Wnt and Notch Signaling Oscillations Controls Mesoderm Segmentation*. *Cell*, 2018. **172**(5): p. 1079-1090 e12.
148. Sonnen, K.F. and A. Aulehla, *Dynamic signal encoding-From cells to organisms*. *Seminars in Cell & Developmental Biology*, 2014. **34**: p. 91-98.
149. Boulet, A.M. and M.R. Capecchi, *Signaling by FGF4 and FGF8 is required for axial elongation of the mouse embryo*. *Developmental Biology*, 2012. **371**(2): p. 235-245.
150. Diez del Corral, R., D.N. Breitkreuz, and K.G. Storey, *Onset of neuronal differentiation is regulated by paraxial mesoderm and requires attenuation of FGF signalling*. *Development*, 2002. **129**(7): p. 1681-1691.
151. Turner, D.A., et al., *Wnt/beta-catenin and FGF signalling direct the specification and maintenance of a neuromesodermal axial progenitor in ensembles of mouse embryonic stem cells*. *Development*, 2014. **141**(22): p. 4243-4253.
152. Olivera-Martinez, I., et al., *Loss of FGF-Dependent Mesoderm Identity and Rise of Endogenous Retinoid Signalling Determine Cessation of Body Axis Elongation*. *Plos Biology*, 2012. **10**(10).
153. Ishimatsu, K., A. Takamatsu, and H. Takeda, *Emergence of traveling waves in the zebrafish segmentation clock*. *Development*, 2010. **137**(10): p. 1595-1599.
154. Diaz-Cuadros, M., et al., *In vitro characterization of the human segmentation clock*. *Nature*, 2020. **580**(7801): p. 113-+.
155. Tomita, T., *The Origin and Regulation of Segmentation Clock Oscillation Dynamics in the Mouse Embryo*. 2022, Ruprecht Karl University of Heidelberg.
156. Vasiliasuskas, D. and C.D. Stern, *Patterning the embryonic axis: FGF signaling and how vertebrate embryos measure time*. *Cell*, 2001. **106**(2): p. 133-136.
157. Iwamatsu, T., *Stages of normal development in the medaka *Oryzias latipes**. *Mech Dev*, 2004. **121**(7-8): p. 605-18.
158. Kasahara, M., et al., *The medaka draft genome and insights into vertebrate genome evolution*. *Nature*, 2007. **447**(7145): p. 714-719.
159. Howe, K., et al., *The zebrafish reference genome sequence and its relationship to the human genome*. *Nature*, 2013. **496**(7446): p. 498-503.

160. Spivakov, M., et al., *Genomic and Phenotypic Characterization of a Wild Medaka Population: Towards the Establishment of an Isogenic Population Genetic Resource in Fish*. *G3-Genes Genomes Genetics*, 2014. **4**(3): p. 433-445.
161. Gutierrez-Triana, J.A., et al., *Efficient single-copy HDR by 5' modified long dsDNA donors*. *Elife*, 2018. **7**.
162. Seleit, A., A. Aulehla, and A. Paix, *Endogenous protein tagging in medaka using a simplified CRISPR/Cas9 knock-in approach*. *Elife*, 2021. **10**.
163. Kumar, S., et al., *TimeTree: A Resource for Timelines, Timetrees, and Divergence Times*. *Molecular Biology and Evolution*, 2017. **34**(7): p. 1812-1819.
164. Driever, W., et al., *A genetic screen for mutations affecting embryogenesis in zebrafish*. *Development*, 1996. **123**: p. 37-46.
165. Haffter, P., et al., *The identification of genes with unique and essential functions in the development of the zebrafish, Danio rerio*. *Development*, 1996. **123**: p. 1-36.
166. Furutani-Seiki, M., et al., *A systematic genome-wide screen for mutations affecting organogenesis in Medaka, Oryzias latipes*. *Mechanisms of Development*, 2004. **121**(7-8): p. 647-658.
167. Elmasri, H., et al., *Mutations affecting somite formation in the Medaka (Oryzias latipes)*. *Mechanisms of Development*, 2004. **121**(7-8): p. 659-671.
168. Furutani-Seiki, M. and J. Wittbrodt, *Medaka and zebrafish, an evolutionary twin study*. *Mechanisms of Development*, 2004. **121**(7-8): p. 629-637.
169. Jardine, D. and M.K. Litvak, *Direct yolk sac volume manipulation of zebrafish embryos and the relationship between offspring size and yolk sac volume*. *Journal of Fish Biology*, 2003. **63**(2): p. 388-397.
170. Kotrschal, K., W.D. Krautgartner, and A. Hansen, *Ontogeny of the solitary chemosensory cells in the zebrafish, Danio rerio*. *Chemical Senses*, 1997. **22**(2): p. 111-118.
171. Lindsay, S.M. and R.G. Vogt, *Behavioral responses of newly hatched zebrafish (Danio rerio) to amino acid chemostimulants*. *Chemical Senses*, 2004. **29**(2): p. 93-100.
172. Robertson, G.N., et al., *Development of the swimbladder and its innervation in the zebrafish, Danio rerio*. *Journal of Morphology*, 2007. **268**(11): p. 967-985.
173. Muller, U.K. and J.L. van Leeuwen, *Swimming of larval zebrafish: ontogeny of body waves and implications for locomotory development*. *Journal of Experimental Biology*, 2004. **207**(5): p. 853-868.
174. Wilson, C., *Aspects of larval rearing*. *ILAR J*, 2012. **53**(2): p. 169-78.
175. Wittbrodt, J., A. Shima, and M. Scharl, *Medaka - A model organism from the Far East*. *Nature Reviews Genetics*, 2002. **3**(1): p. 53-64.
176. Kinoshita, M., et al., *Medaka: Biology, Management, and Experimental Protocols*. 2009, Ames, Iowa: Wiley-Blackwell.
177. Cope, J., et al., *The stellate layer and rhythmic contractions of the Oryzias latipes embryo*. *J Exp Zool*, 1990. **254**(3): p. 270-5.
178. Fluck, R.A., A.L. Miller, and L.F. Jaffe, *Calcium Waves Accompany Contraction Waves in the Oryzias-Latipes (Medaka) Blastoderm*. *Biological Bulletin*, 1991. **181**(2): p. 352-352.

179. Simon, J.Z. and M.S. Cooper, *Calcium Oscillations and Calcium Waves Coordinate Rhythmic Contractile Activity within the Stellate Cell Layer of Medaka Fish Embryos*. Journal of Experimental Zoology, 1995. **273**(2): p. 118-129.
180. Ishikawa, T., et al., *UPR transducer BBF2H7 allows export of type II collagen in a cargo- and developmental stage-specific manner*. Journal of Cell Biology, 2017. **216**(6): p. 1761-1774.
181. Arzt, M., et al., *LABKIT: Labeling and Segmentation Toolkit for Big Image Data*. Frontiers in Computer Science, 2022. **4**.
182. Thomson, L., L. Muresan, and B. Steventon, *The zebrafish presomitic mesoderm elongates through compaction-extension*. Cells & Development, 2021. **168**.
183. Syvaaja, J., et al., *DNA polymerases alpha, delta, and epsilon: three distinct enzymes from HeLa cells*. Proc Natl Acad Sci U S A, 1990. **87**(17): p. 6664-8.
184. Jung, G., et al., *Diffusion of small molecules into medaka embryos improved by electroporation*. BMC Biotechnol, 2013. **13**: p. 53.
185. Mönke, G.S., F. A.; Schmal, C.; Granada, A. E., *Optimal time frequency analysis for biological data - pyBOAT*. bioRxiv, 2020.
186. Monroy, A., M. Ishida, and E. Nakano, *The pattern of transfer of the yolk material to the embryo during the development of the teleostean fish, Oryzias latipes*. Embryologia, 1961. **6**(1-3): p. 151-158.
187. Puangchit, P., et al., *Non-staining visualization of embryogenesis and energy metabolism in medaka fish eggs using near-infrared spectroscopy and imaging*. Analyst, 2017. **142**(24): p. 4765-4772.
188. Fraher, D., et al., *Zebrafish Embryonic Lipidomic Analysis Reveals that the Yolk Cell Is Metabolically Active in Processing Lipid*. Cell Rep, 2016. **14**(6): p. 1317-1329.
189. Link, V., A. Shevchenko, and C.P. Heisenberg, *Proteomics of early zebrafish embryos*. BMC Dev Biol, 2006. **6**: p. 1.
190. Diaz-Cuadros, M., et al., *Metabolic regulation of species-specific developmental rates*. Nature, 2023. **613**(7944): p. 550-557.
191. Snow, M.H.L., *Gastrulation in the mouse: Growth and regionalization of the epiblast*. Development, 1977. **42**(1).
192. Venters, S.J., M.L. Hultner, and C.P. Ordahl, *Somite cell cycle analysis using somite-staging to measure intrinsic developmental time*. Dev Dyn, 2008. **237**(2): p. 377-92.
193. Mills, C.L. and R. Bellairs, *Mitosis and cell death in the tail of the chick embryo*. Anat Embryol (Berl), 1989. **180**(3): p. 301-8.
194. Tiwari, P., H. Rengarajan, and T.E. Saunders, *Scaling of internal organs during Drosophila embryonic development*. Biophysical Journal, 2021. **120**(19): p. 4264-4276.
195. Shingleton, A.W., et al., *Many ways to be small: different environmental regulators of size generate distinct scaling relationships in Drosophila melanogaster*. Proceedings of the Royal Society B-Biological Sciences, 2009. **276**(1667): p. 2625-2633.
196. Cooke, J., *A note on segmentation and the scale of pattern formation in insects and in vertebrates*. Development, 1988. **205**: p. 245-248.
197. Inoue, D. and J. Wittbrodt, *One for all--a highly efficient and versatile method for fluorescent immunostaining in fish embryos*. PLoS One, 2011. **6**(5): p. e19713.